ICMAB Universitat Autònoma de Barcelona CSIC

Memòria de la tesis doctoral

Coated Conductors and Chemical Solution Growth of YBCO Films: A Micro-Raman Spectroscopy Study

Programa de Doctorat en Ciència de Materials
Departament de Física de la Universitat Autònoma de Barcelona

Por:
Juan Carlos González González
Departament de Materials Magnètics i Superconductors
Institut de Ciència de Materials de Barcelona
Consejo Superior de Investigaciones Científicas

Directores: Dra. Teresa Puig i Molina
Dr. Narcís Mestres i Andreu
Tutor: Prof. Santiago Suriñach

Bellaterra, 24 de Gener de 2005

En Teresa Puig i Molina, Científica Titular de l'Institut de Ciència de Materials de Barcelona, i Narcís Mestres i Andreu, Investigador Científic de l'Institut de Ciència de Materials de Barcelona

CERTIFIQUEN

Que el treball presentat a la memòria "Coated Conductors and Chemical Solution Growth of YBCO Films: A Micro-Raman Spectroscopy Study", que presenta Juan Carlos González González com a memòria de la tesis doctoral en Ciència dels Materials, ha estat realitzat sota la seva direcció.

Bellatera, Gener de 2005.

Dra. Teresa Puig i Molina　　　Dr. Narcís Mestres i Andreu

Tutor: Prof. Santiago Suriñach

Acknoledgements

In first place, I would like to thanks personal and sinceresly to Professor Xavier Obradors, Vice director of the *Institut de Ciència de Materials de Barcelona – CSIC*, for his friendship, continuous support and to give me the opportunity to participate in the European project called *SOLSULET*.

I would like to thanks personal and sinceresly to Dr. Narcís Mestres i Andreu, from the Optic department at *Institut de Ciència de Materials de Barcelona – CSIC*, for his friendship, continuous support and his holy patient for teach me his knowledge about Raman effect.

I would like to thanks personal and sinceresly to Dra. Teresa Puig i Molina, from the Magnetic and Superconducting Materials at *Institut de Ciència de Materials de Barcelona – CSIC*, for her friendship, continuous support and teach me her knowledge about the fascinating superconducting world.

I would like to thanks to the Agencia Española de Cooperación Internacional (AECI) from the Ministerio de Asuntos Exteriores of the Spanish government, for the PhD fellowship.

I would like to thanks to the Ministerio de Educación, Ciencia, Cultura y Deporte of the Spanish government, for the grant to finish my PhD studies.

I would like to thanks to the Fundació Bosh i Gimpera of Catalunya, for the economic support to finish my PhD thesis.

I would like to thanks to Dr. Alberto Pomar from the Magnetic and Superconducting Materials at *Institut de Ciència de Materials de Barcelona – CSIC*, for the resistivity measurements.

I would like to thanks to Professor H. C. Freyhardt from the Göttingen University in Germany and Dr. R. Feenstra from the Oak Ridge National laboratory in USA; for supply us the high-J_c coated conductors.

I would like to thanks to Professor Jordi Pascual, head of the Raman laboratory at the Physics departement of the UAB, for his continuous support and friendship.

I would like to thanks to the incomparable and tireless PhD students team of the *SOLSULET* project: Mariona Coll, Anna Palau, Marta Rossell, Andrea Cavallaro, Jaume Gazquez, Joffre Gutierrez i Oscar Castaño; for their continuous support.

El meu agraïment i etern reconeixement al meus amics i companys: Simonetta Illiescu, Neus Romá, Mariona Coll, Anna Palau, Liber Abad, Ingrid Cañero, Elisenda Rodriguez, Laura Fernández, Natalia Bedoya, Anna Esther Carrillo, Andreas Cavallaro de la Vega, Sergi Valencia, José Navarro, Oscar Castaño, David Bastidas, Jaumet Gazquez, Bernat Bozzo, Joffre Gutierrez, Xavier Martí, Diego Rubi, Ramon Rubi, Jordi Figueras, David Martinez, Gervasi Herranz, Nico Dix, Roberto Fernández, Jordi Teva, Oriol Sabater, Ignasi Mata, Mustapha Najib, Manu Bibes, Simon Sena, i Jerome Plain.

A l'equip de futbol sala del ICMAB, als pitxixis de la lligueta: Oscar Castaño, David Bastidas, Jaumet Gazquez, Joffre Gutierrez, Benja Martinez, Dani Maspoch, Dani Ruiz, Santi Salas, David Martinez,

El meu agraïment als meus etern amics peruans, per als seus cartas de entusiasme i opinions.

A la *molècula pentatòmica* per les discussions acadèmiques al Poble Nou, sense els quals no hagués estat possible avançar en el meu projecte.

A la meva família, en especial a la meva mare, per el seu entusiasme.

A la meva dona, la Yhelina, per la seva paciència i el seu recolzament.

A tota la penya del ICMAB

A la gent de Catalunya, per la seva acollida i per el seu calor humà, que ha fet sentir-me no tan lluny de casa.

To my wife, Yhelim
Who made everything possible

Contents

Chapter 1.

Abbreviated Terms

Nomenclature

α	Scattering angle
α	Absorption coefficient
θ	Tilt angle
θ	Misorientation angle
λ	Superconducting penetration depth
λ	Wavelength of radiation
χ	Magnetic susceptibility per volume unit
$\chi(\omega)$	Electric susceptibility
δ	*c*-axis grain fraction
γ	Anisotropy factor
γ	FWHM of the Raman profile
φ	Rotation angle
ϕ	Magnetic flux
ρ	Normal-state resistivity
ξ	Superconducting coherence length
ε	Electric permitivity
$\Delta\phi$	FWHM of the *in-plane* texture
$\Delta\omega$	FWHM of the *out-of-plane* texture
a, b, c	Unit cell parameters
A	Area
A	Total YBCO grain population
$\mathrm{A_g}$	One-dimensional vibration in the *z*-direction
$\mathrm{B_{1g}}$	One-dimensional vibration in the *z*-direction
$\mathbf{B_c}$	Critical induction field
$\mathbf{B_{c1}}$	Lower critical field
$\mathbf{B_{c2}}$	Upper critical field
$\mathbf{B_{irr}}$	Irreversibility field
$\mathbf{c}$	Light velocity
$\mathbf{e}_\mathrm{i}$	Incident unit vector
$\mathbf{e}_\mathrm{S}$	Scattering unit vector
$\mathbf{E}$	Electric field
f_a	*a*-axis oriented grain fraction by XRD
f_c	*c*-axis oriented grain fraction by XRD
$\mathbf{F}_\mathrm{L}$	Lorentz force
H_{ext}	External magnetic field
$\mathrm{I_c}$	Critical current
I_a	Raman intensity of the *a*-axis oriented grains
I_c	Raman intensity of the *c*-axis oriented grains

$I_{\phi_a}^{(102)}$	Integrated intensity of ϕ-scan (102) XRD reflection for *a*-domain
$I_{\phi_c}^{(102)}$	Integrated intensity of ϕ-scan (102) XRD reflection for *c*-domain
$I(\varphi)$	Angular dependence of the Raman intensity
I_R	Raman signal intensity
J_c	Critical current density
K	Intensity correction factor
k	Photon wavevector
M	Magnetization vector
P	Polarization vector
$P(H_2O)$	Water vapour partial pressure
$P(O_2)$	Oxygen partial pressure
q	adimensional parameter (1/*q* called Fano parameter)
q	Phonon wavevector
Q	Phonon coordinate
Q	Biaxial texture parameter
r	Raman intensity ratio of O(2,3)-B_{1g} and O(4)-A_g modes
R	Raman tensor
$\mathbf{R}_{Ag}$	Raman tensor of O(4)-A_g mode
$\mathbf{R}_{B1g}$	Raman tensor of O(2,3)-B_{1g} mode
R	Radius of the sample
T	Temperature
T_c	Superconducting critical temperature
t	Sample thickness
ω	Phonon frequency
x	Oxygen content in $YBa_2Cu_3O_{7-x}$
x, y, z	Cartesian coordinates
$x_{A_g}, y_{A_g}, z_{A_g}$	Raman tensor components of A_g mode
$x_{A_{1g}}, z_{A_{1g}}$	Raman tensor components of A_{1g} mode
$x_{B_{1g}}, z_{B_{1g}}$	Raman tensor component of B_{1g} mode
v	velocity
V_c	Scattering volume

Acronyms and Initials

AFM	Atomic force microscopy
BSCCO	$Bi_2Sr_2Ca_2Cu_3O_y$
CC	Coated conductor
CD	Cation disorder
CCD	Charge-coupled device
DGT	Double grating *turret*
EELS	Electron energy loss spectroscopy
EDP	Electron diffraction pattern
EDX	Energy-dispersive X-ray diffraction
FWHM	Full width at half maximum

GB	Grain boundary
GUI	Graphic user interface
HTS	High-temperature superconductor/s
ICMAB	Institut de Ciència de Materials de Barcelona
IL	Irreversibility line
IR	Infrared radiation
La214	$La_{1-x}Sr_xCuO_4$
LH_2	Liquid hydrogen
LHe_2	Liquid helium
LN_2	Liquid nitrogen
MBE	Molecular beam epitaxy
MOD	Metal organic decomposition
PDF	Powder diffraction file
PLD	Pulsed laser deposition
$Power_L$	Nominal laser power output
$Power_S$	Power on sample
RABiTS	Rolling-Assisted Biaxially Textured Substrate
RISC	Reduced instruction set computer
SEM	Scanning electron microscopy
SMES	Superconducting magnetic energy storage
SNF	Supernotch filter
SOLSULET	Novel sol gel technology for long length superconducting coated tapes
SQUID	Superconducting quantum interference device
TEM	Transmission electron microscopy
TEM_{ii}	Transverse electromagnetic modes
TFA	Trifluoroacetate
TlBCCO	$Tl_2Ba_2Ca_2Cu_3O_z$
UAB	Universitat Autònoma de Barcelona
UB	Universitat de Barcelona
XRD	X-ray diffraction
YBCO	Yttrium barium copper oxide ($YBa_2Cu_3O_{7-x}$)
YSZ	Yttria-stabilized zirconia

Abstract

We present the non-destructive studies on coated conductors and YBCO TFA-MOD films by micro-Raman spectroscopy complemented by other techniques such as XRD, SEM, TEM, resistiviy and critical current density. We determined quantitatively the degree of uniaxial and biaxial texture of YBCO coated conductors and investigated aspects like crystal orientation, uniformity, secondary phases, impurities, oxygen content and defects of TFA-MOD grown films based on the specific Raman selection rules for YBCO and polarized Raman scattering experiments. Moreover, we have studied the main YBCO TFA growth parameters and their relevance in the final microstructure and superconducting properties. Finally, we studied the role of the intermediate phases on the mechanism of YBCO nucleation and growth.

Preface

Micro-Raman spectroscopy has become a very useful, powerful tool, and non-destructive technique complementary to other techniques to the characterization and study of High T_c superconducting oxides. Through this thesis we will show the usefulness and completeness of the micro-Raman spectroscopy in the study of YBCO coated conductors and TFA-MOD films.

This thesis is divided in six chapters. In the first one, we expose an amenable brief introduction to high temperature materials, especially focused on the YBCO compound; in addition we perform a short revision of the Raman effect and the corresponding optical phonon modes of YBCO necessary to understand the study and characterization of YBCO films by micro-Raman spectroscopy.

Then, in the second chapter we describe briefly the experimental techniques used for the physical characterization of YBCO films like micro-Raman spectroscopy, x-ray diffraction (XRD), scanning electron microscopy (SEM), resistivity, transmission electron microscopy (TEM) and critical current density. Because this thesis is focused on the use of micro-Raman spectroscopy, we describe this technique in more detail.

In the third chapter we perform a quantitative determination of the degree of uniaxial and biaxial texture in coated conductors and YBCO films. The *in-plane* grain orientation is governed by Lorentz distribution function. The Raman results are compared with results of XRD ϕ-scans measurements, and we demonstrate the relationship between texture determination by both techniques.

After, in the fourth chapter we describe in detail the YBCO TFA-MOD process necessary for the study, analysis and characterization of TFA grown films, and we show with emphasis the applications of the Raman scattering analysis of TFA films in aspects like orientation, uniformity, secondary phases, impurities, oxygen content and structural defects.

Then, in the fifth chapter, we study the relevance of control of YBCO TFA growth parameters on the final microstructure and superconducting properties. The growth parameters studied are: reaction time, growth temperature, water vapour pressure and gas flow rate. We also investigate the influence of porosity on the superconducting properties of the TFA films and its possible reduction by applying a sintering process.

Following, in the sixth chapter, we present our preliminary studies toward further knowledge on the mechanisms of YBCO nucleation and the role of intermediate phases such as BaF_2, Y_2O_3, CuO and $Y_2Cu_2O_5$ in the growth of the YBCO phase in the TFA-MOD process by analyzing quenched films at different temperatures of the heating ramp.

Finally, we present the general conclusions of this study and bibliography.

Motivation

Since their discovery in 1987, significant progress has been made in the fabrication of high-quality, high-temperature YBCO superconducting thin films. A major challenge facing the commercialization of high-temperature superconductors tapes is reducing the cost of manufacturing while maintaining the performance required for practical applications. Chemical solution growth of epitaxial YBCO tapes has emerged as a very competitive technique to obtain superconducting tapes of high quality at low cost. In particular, it has been showed that is possible to growth epitaxial high-T_c superconducting materials onto single crystals substrates given new opportunities for appearance of different applications where texture or granular feature of the material needs to be controlled. But single crystal substrates are not suitable for many practical applications because their cost, limitations in size and shape, and lack of flexibility. Hence, a great deal of effort has been directed at the fabrication of YBCO tapes on technical substrates. The preparation of superconducting coated conductors (second generation high temperature superconducting tapes), where a biaxial texture of the superconducting oxide needs to be reached on metallic substrates, can strongly benefit from this new methodology.

Presently several growth techniques to obtain YBCO films onto different kinds of substrates exists, such as: *Pulsed Laser Deposition* (PLD), *Sputtering*, *Thermal Co-evaporation*, *Chemical Vapour Deposition* (CVD), *Liquid Phase Epitaxy* (LPE), *Metal organic Deposition* (MOD), etc. Among the various processes used for the deposition of YBCO tapes, metalorganic deposition (MOD) process using trifluoroacetates (TFA) is a promising approach for a variety of reasons. First, solution-based coating techniques are well-established industrial processes for coating wide, continuous lengths of flexible substrates. Second, the low capital equipment and materials cost of MOD-TFA make the approach more cost-effective than alternative vapour-phase techniques. Additionally, the precursor chemistry and stoichiometry are easily controlled, allowing precise optimization of the properties and uniformity of the YBCO film. Although solution-based deposition processes have been successfully developed for a variety of applications, continuous deposition of high-quality superconducting films over flexible kilometre-length metallic substrates is a new application. However, it is indispensable to control the complex growth process and thus optimize the microstructural factors that may have influence into the superconducting properties of these materials. Due to the anisotropy of these materials, they require to be biaxially textured onto the substrate to be able to transport high currents at high magnetic fields. This challenge has been taken by the superconductivity group at ICMAB in the scope of the European project called *SOLSULET*.

In this work, we have studied the structural characterization of coated conductors and YBCO superconducting films prepared by the MOD-TFA process onto single crystal substrates, by micro-Raman spectroscopy (μRS), x-ray diffraction (XRD), scanning electron microscopy (SEM) and transmission electron microscopy (TEM) (in collaboration with other collegues). These have been complemented by the superconducting characterization by resistivity and critical current density measurements also carried out by the other members of the group, to be able to later transfer this growth technology to metallic substrates.

Therefore, among these analytical techniques micro-Raman spectroscopy is the main technique to be used in this thesis. The micro-Raman spectroscopy is a very effective analytical tool, quick and non-destructive, with high sensitivity and high spatial resolution (in the order of 1 μm), to characterize superconducting films, complementary to the other analytical techniques above mentioned. The potentiality of this technique allowed us to characterize the uniaxial and biaxial texture, the distribution and sizes of YBCO grains, the secondary and impurity phases present in the film, the oxygen content and defects present in the YBCO structure, the intermediate phases involved in the reaction kinetics to get YBCO and the nucleation and growth processes.

Chapter 1

This chapter is divided in two parts. The first one is devoted to a brief introduction to high temperature superconductor materials, and specially focused on the $YBa_2Cu_3O_{7-x}$ (YBCO) compound, while the second one is devoted to a short revision on the Raman effect and the optical phonon modes of YBCO, necessary to understand the characterization of YBCO films by micro-Raman spectroscopy.

A. Introduction to High Temperature Superconductor Materials

1.1. Introduction to Superconductivity

The superconductors are materials that loss their electric resistance ($\rho = 0$)[1.1] below a certain critical temperature, called T_c (figure 1.1a) and the magnetic inductance field becomes zero ($\mathbf{B} = 0$) inside them when they are cooled below T_c in a weak external magnetic field, H_{ext}, *Meissner* effect[1.1] (figure 1.1b).

These are two distinctive properties for a material to be considered a superconductor. However, if we pass a current higher than the critical current density J_c, the superconducting state is destroyed. The mechanism to avoid the dissipation, in the superconducting state, is the weak coupling of a conduction electron with another one in the form of pairs, called *Copper pairs*. They can flow without any dissipation, there is no scattering of the "individual" pairs with atoms or impurities, and therefore there is no resistivity. The correlation distance between two electrons of the Copper pair is named the coherence length, $\xi(T)$.

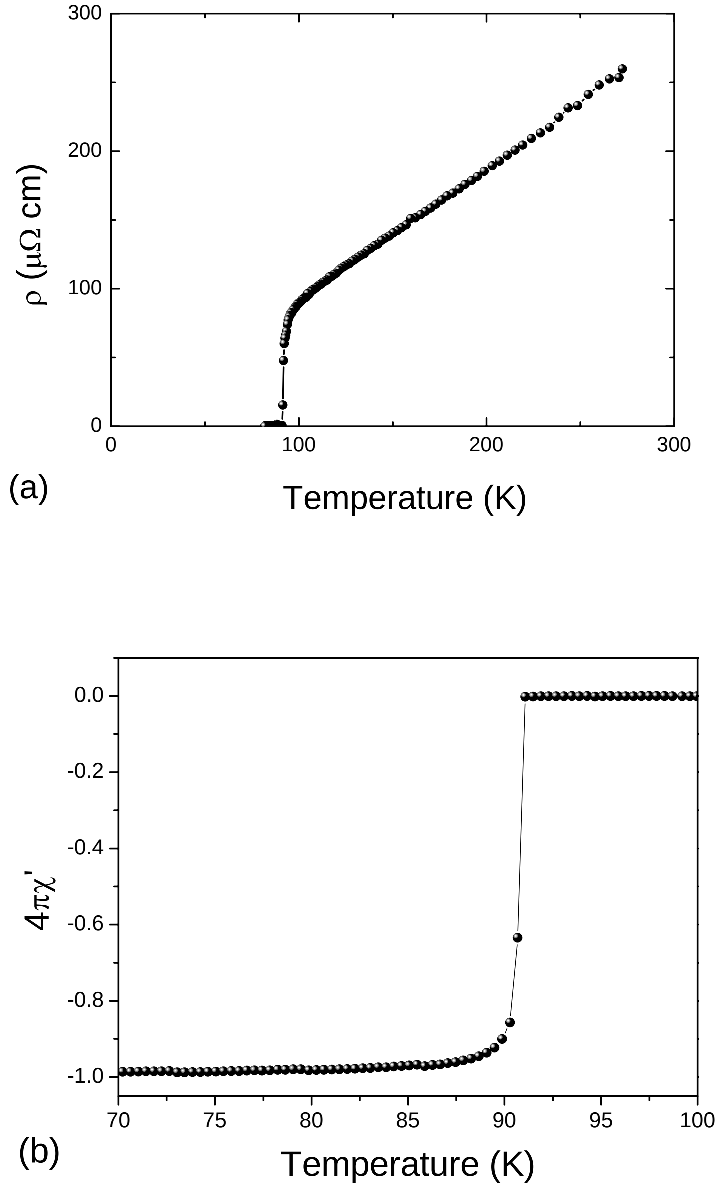

Figure 1.1. (a) Resistivity and (b) Magnetic susceptibility of YBCO film.

We will describe briefly the two types of superconductors[1.2]: *type I* and *type II* superconductors.

1.1.1. Type I superconductors

They are materials that completely expel magnetic flux from their interior, by means of surface currents (*Meissner* effect). The distance of the sample region through which the surface currents flow is called *superconducting penetration depth*, λ(T). The strength of the magnetic induction required to completely destroy the state of perfect diamagnetism (χ = -1) in the interior of the superconducting specimen is called the critical induction field $\mathbf{B_c}$.

1.1.2. Type II superconductor

For a *type II* superconductor there are two critical induction fields. The lower critical field $\mathbf{B_{c1}}$ and the upper critical field $\mathbf{B_{c2}}$. The flux is completely expelled (*Meissner* state) only up to the induction field $\mathbf{B_{c1}}$. So in applied induction fields smaller than $\mathbf{B_{c1}}$, the *type II* superconductor behaves like as *type I* superconductor below $\mathbf{B_c}$. Above $\mathbf{B_{c1}}$ the magnetic flux partially penetrates into the material until the upper critical field $\mathbf{B_{c2}}$, is reached. Above $\mathbf{B_{c2}}$ the material reaches the normal state (see figure 1.2).

1.1.2.1. Mixed State

Between $\mathbf{B_{c1}}$ and $\mathbf{B_{c2}}$ the superconductor is said to be in the *mixed state* (figure1.2) in which the magnetic flux partially penetrates the superconducting specimen in the form of tiny microscopic filaments called *vortices*, each one containing a flux quantum. A vortex consists of a normal core (size in the order of ~ ξ), in which no *Copper pairs* exist, surrounded by a superconducting region (size in the order of ~ λ) in which a persistent supercurrent flows, which generates a field within the core equivalent to a flux quantum. The number of vortices gradually increases as the field is raised from $\mathbf{B_{c1}}$ to $\mathbf{B_{c2}}$ ($n = \frac{\mathrm{B}}{\phi_o}$, n is the density of vortices).

When a current density ($\boldsymbol{J}$) is applied to a *type II* superconductor in the mixed state, the *Lorentz* force ($\mathbf{F_L} = \boldsymbol{J} \, x \, \mathbf{B}$) acts on the vortex leading to flux motion if there is no barrier for flux motion. When vortices move at the velocity of $\mathbf{v}$, an electric field (**E**) is created in the direction of the current as $\mathbf{E} = \mathbf{v} \text{ x } \mathbf{B}$ and a voltage appears. This creates a non-desirable energy dissipation and a non zero-resistance state is obtained. In real materials, there are impurities and imperfections in the atomic lattice to pin these vortices (F_p, pinning force), and avoid their movement and therefore dissipation.

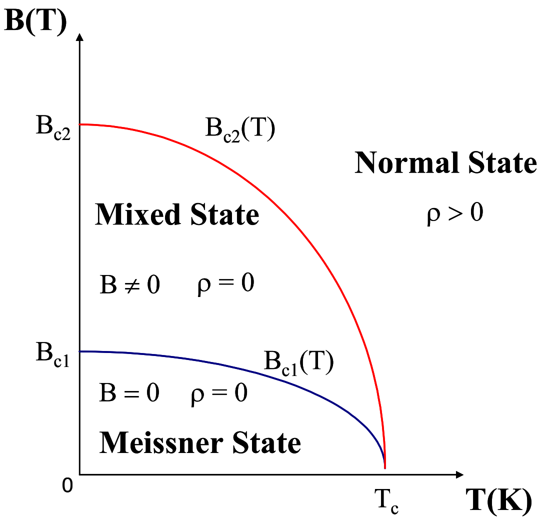

Figure 1.2. Magnetic phase diagram of a *type II* superconductor. The variations of critical fields $\mathbf{B}_{c1}$ and $\mathbf{B}_{c2}$ as a function of temperature are shown.

Thanks to this partial flux penetration, the material can withstand strong applied magnetic fields without ongoing to the normal state. Superconductivity does persist in the mixed state up to the upper critical field $\mathbf{B}_{c2}$.

For high-power applications, *type II* superconductors are the only candidates to transport high currents in high magnetic fields. It was this which made possible the development of low T_c superconductor wires during 1960s and 1970s to useful high-field superconducting magnets working at very low temperatures close to liquid helium, 4K.

The high temperature superconductors (HTS) are ceramic compounds (*type II* superconductors) based on cooper oxides; they have critical temperatures close to 100K. One of the compounds more intensely studied is $YBa_2Cu_3O_{7-\delta}$ (YBCO); it has a critical temperature of ~ 92K. This temperature is higher enough to enable to use liquid nitrogen (77K) as cooling liquid, thus enlarging its engineering applications to power applications.

Nowadays, the low T_c superconductors can be explained by the weak coupling of *Copper pairs* (electron-electron coupling via a phonon) described by the BCS theory developed in 1957. However, the HTS can not be explained by the BCS theory, because it can not explain the coupling energy necessary at high temperatures. Other strong-electron coupling theories are required.

1.2. Fundamental Properties of YBCO

1.2.1. YBCO Structure

The YBCO compound forms in an orthorhombic *Pmmm* structure with a single formula per primitive cell. The structure is illustrated in figure 1.3. The structure is about as simple as conceivable for a quaternary compound with ratios 1:2:3:7. It can be viewed as a defect perovskite lattice $(Y\text{-}Ba)_3Cu_3O_{9-x}$, based on three Cu-centered perovskite cubes with both O vacancy ordering and Y-Ba ordering along *c*-axis. Of two vacancies (x = 2), one occurs in every Cu-O plane, along *a*-axis at site (½, 0, 0), resulting in the orthorhombic symmetry. The Y and two Ba ions order along the *c*-axis, and the other O vacancy occurs in the Y plane. The unit cell parameters are: a = 3.8185 Å, b = 3.8856 Å and c = 11.6804 Å[1.3].

The resulting structure is usually described in terms of CuO_2 planes and CuO chains. The chains consist of Cu(1) and O(1) atoms (we are using atoms notation of *Jorgensen*[1.3]) along the *b*-axis, at (0, 0, 0) and (0, ½, 0), respectively. These chains are more properly regarded as ribbons, since the O(4) atom lies above and below the Cu(1) atom at the (0, 0, $z_{O(4)}$) position, and the Cu(1)-O(4) separation is the smallest Cu-O distance in the structure. Thus the Cu(1) atom is fourfold coordinated with O ions, each O(1) ion is shared by two Cu(1) atoms. The CuO_2 superconducting planes consists of Cu(2) sites at (0, 0, $z_{Cu(2)}$) neighbored by O(2) and O(3) sites at (½, 0, $z_{O(2)}$) and (0, ½, $z_{O(3)}$). The heights are, in units of c, given by $z_{Cu(2)}$ = 0.3574 Å, $z_{O(2)}$ = 0.3767 Å, $z_{O(4)}$ = 0.1542 Å and $z_{O(3)}$ = 0.3804 Å, according to *Jorgensen*[1.3]. The CuO_2 planes are therefore somewhat dimpled, with two oxygens O(2) and O(3) being nearly coplanar, but with the Cu(2) site lying out of this plane by ~0.22*c* = 0.25 Å (we shall denote the O(2) and O(3) ions pair like O(2,3)).

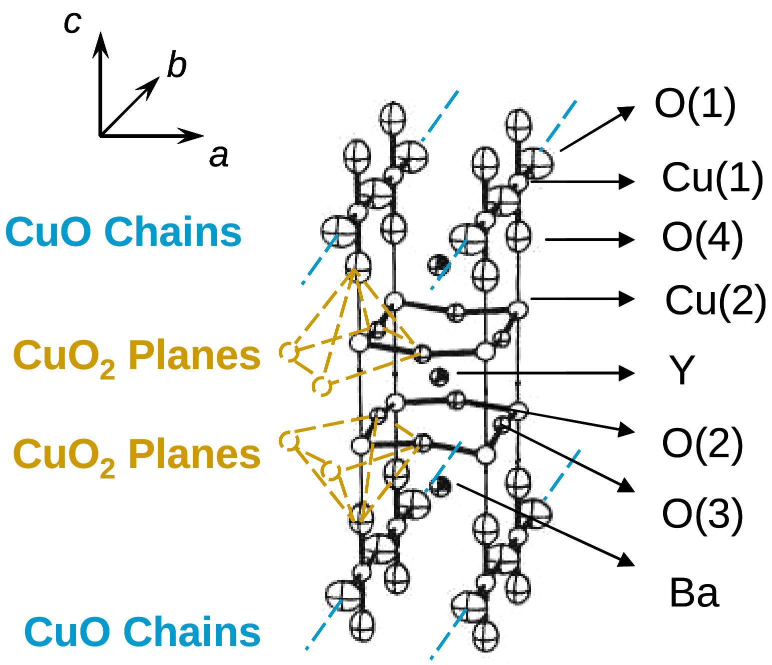

Figure1.3. YBCO orthorhombic unit cell. YBCO is a complex, layered perovskite centred on a yttrium layer, around which are stacked the CuO_2 superconducting planes and a double layer of BaO and CuO.

With Cu(1) chosen at the origin, the Y site is at (½, ½, ½) and the Ba site is at (½, ½, z_{Ba}), with z_{Ba} = 0.1895 Å[1.3]. Thus the Ba and O(4) sites form a warped rocksaltlike layer between the superconducting planes and the chains. Oxygen atoms are entirely missing from the Y layers, which separate the CuO_2 planes in the unit cell.

1.2.2. Structural Blocks

The YBCO unit cell can be conceptualized from two structural blocks with distinct electronic properties, as shown in figure 1.4. The first block consists of one CuO_2 plane. Each Cu atom in the CuO_2 layer is surrounded by four O atoms in a square-planar configuration (figure 1.3). For HTS structures with more than one CuO_2 planes per unit cell like TlBCCO, BSCCO and HgBCCO, the individual layers are separated by a layer of divalent alkaline earth or trivalent rare earth atoms[1.4]. The CuO_2 planes define the *a*-*b* planes in all HTS crystal structures, with the *c*-axis of the crystal structure perpendicular to the planes. The second block in unit cell is often referred to as a charge reservoir (metallic chains in YBCO) and is used to define specific homologous HTS families of compounds. Within each HTS compound, this block appears to be largely responsible for providing charge carriers to the CuO_2 planes. It also determines the degree of anisotropy in the individual HTS compounds.

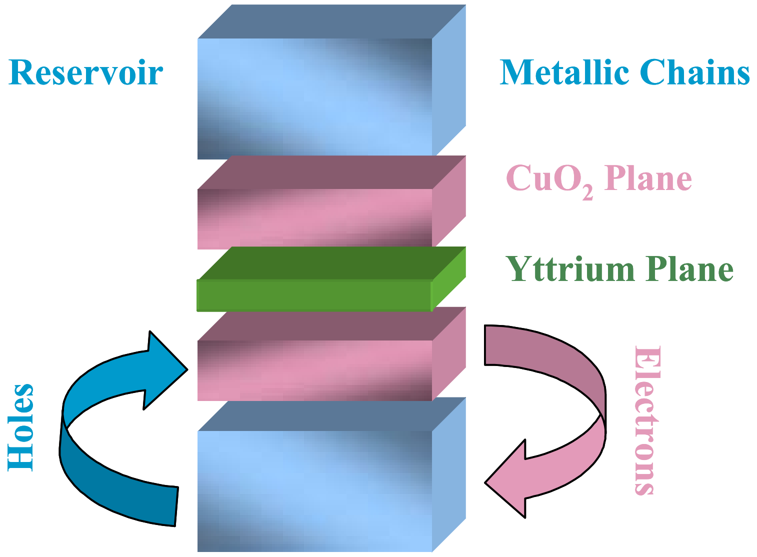

Figure 1.4. Schematic view of the chemical blocks in YBCO superconductor.

1.2.3. Irreversibility Line

An important property of YBCO relates to the ability of this material to carry significant currents at high external magnetic induction field and as any *type II* superconductor, magnetic induction field penetrate the HTS cuprates in the form of vortices in the mixed state. At a given temperature, each HTS material has a maximum magnetic field, $\mathbf{B}_{\mathbf{irr}}$, above which loss-free *dc* current flow is not possible, dissipation starts due to motion of vortices at any small applied current, *i.e.* the mixed state enters to a reversible state where $J_c = 0$. The field-temperature line (**B-T**) dividing $J_c \neq 0$ from the $J_c = 0$ states is defined as the irreversibility line (IL). This line is very important for application purpose since it sets the position from where the material is not anymore useful although it is still in the superconducting state, as shown in figure 1.5.

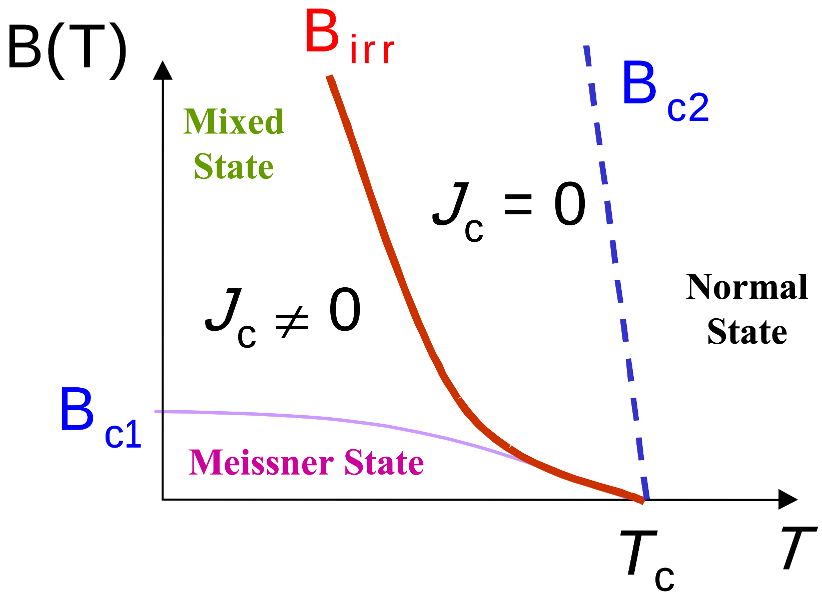

Figure 1.5. Scheme of the irreversibility line $\mathbf{B}_{\mathbf{irr}}$ and the critical magnetic fields B_{c1} and $\mathbf{B}_{\mathbf{c2}}$ as a function of temperature.

Figure 1.6 shows IL for typical superconductors and temperatures of cryogenic liquids. As it is shown in figure 1.6, YBCO is the best candidate for high-power applications at 77 K at high external magnetic fields.

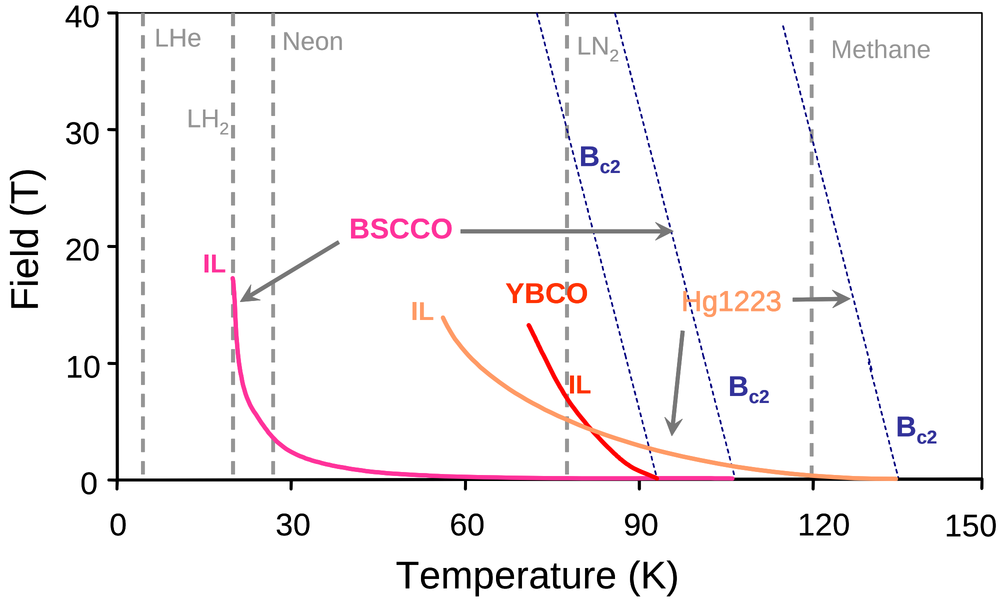

Figure 1.6. Upper critical induction fields (discontinued lines) and irreversibility lines (continued lines) for some HTS superconducting materials.[1.6]

1.2.4. Anisotropy Factor

The layered structure of HTS leads to a very anisotropic materials. The superconducting coherence length, $\xi(T)$, is defined as the correlation distance between two electrons of the Cooper pair, is then also anisotropic and quite small in the YBCO compound. The typical values, for YBCO, are in the order of the atomic space, $\xi_{ab}(T) \sim$ 30Å, $\xi_c(T) \sim$ 4Å[1.5]. The conductivity in the *a*-*b* plane is then also very different from the one in the *c*-direction, so it tends to flow mainly along *a*-*b* planes, *i.e.*, $J_c^{ab} >> J_c^c$. Therefore, for high-power applications we need the YBCO *c*-axis grains grown perpendicular to the substrate, as illustrated in figure 1.7.

In table 1.1 it is shown the anisotropy factor, γ, of two superconductors: YBCO and $Bi_2Sr_2Ca_2Cu_3O_y$ (BSCCO). The anisotropy factor, γ, is related to the ratio between the resistivity in the *c*-direction to resistivity in the *a*-*b* plane ($\gamma^2 = \frac{\rho_c}{\rho_{ab}}$).

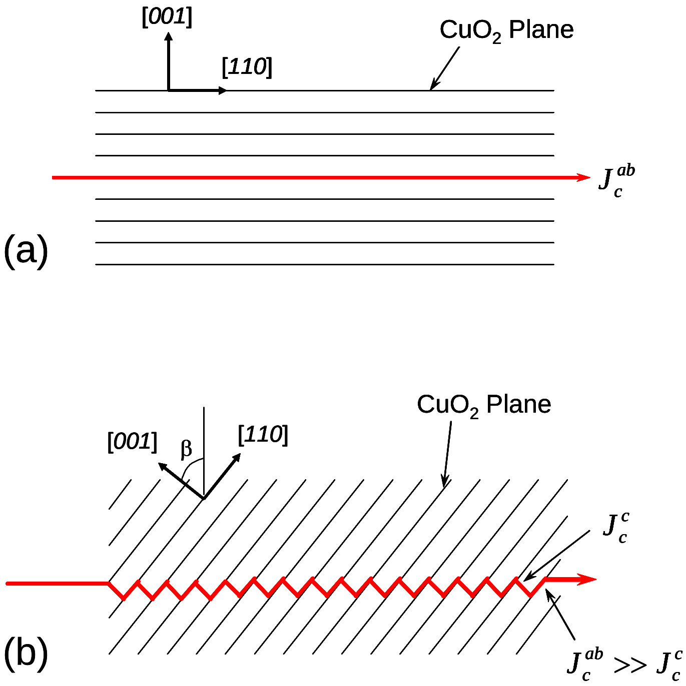

Figure 1.7. Scheme of circulating current in YBCO film (a) *c*-axis oriented and (b) inclined *c*-axis oriented with regard to substrate surface.

Table 1.1

Measured anisotropy factor for YBCO and Bi2212 crystals

Sample	**T_c (K)**	**γ^2**
$YBa_2Cu_3O_7$ [1.8]	92.6	50
$Bi_2Sr_2Ca_2Cu_3O_y$ [1.8]	110	200000

An explanation to the variation of γ^2 for BSCCO superconductor falls in its crystallographic structure, where the CuO_2 superconducting planes are separated by insulator blocks performing the function of insulating charge reservoirs, while for YBCO, the CuO_2 superconducting planes are separated by metallic chains of CuO performing the function of metallic charge reservoirs (see figure 1.4) diminishing the resistivity along the *c*-axis.

1.2.5. *In-plane* Grain Boundaries

One aspect that became clear early in HTS research was also the detrimental effect of *in-plane* grain boundaries (GB) on transport currents. In all the HTS materials, the current density that can flow through the material is severely limited by the presence of GB, particularly for those boundaries with misorientation [*001*] tilt-angles greater than 10 degrees[1.9]. Transport studies through individual GB in YBCO bicrystals[1.10] and coated conductors[1.11] showed that large-angle grain boundaries act as weak links in the superconductor. Therefore, the *in-plane* GB are the main limitation for the flow of the critical current, as they constitute a barrier for current flow. The critical current density J_c through the *in-plane* GB is very sensitive to YBCO grains orientation because it decreases exponentially with tilt-angle, θ, following the relation[1.10,1.11] (figure 1.8):

$$J_c(\theta) = J_c(0)\exp(-\theta/\theta_0) \tag{1.1}$$

where $J_c(0)$ and θ_0 are constants.

It also implies that HTS wires and tapes with very high current-carrying capability require fabrication techniques that result in highly biaxially oriented material virtually epitaxial and with no *in-plane* GB larger than 4 – 5° degree.

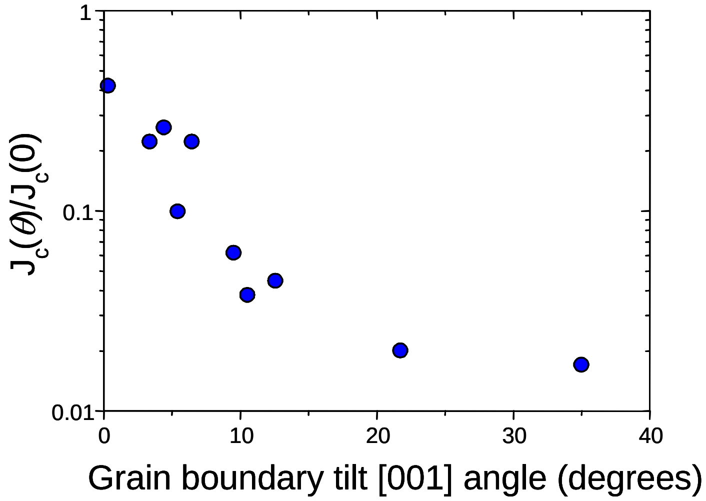

Figure 1.8. Dependence of J_c on misorientation [*001*] tilt-angle for YBCO films on $SrTiO_3$ bicrystals measured by Dimos *et al*[1.10].

1.2.6. Oxygen Stoichiometry

In all of the HTS cuprates, charge doping plays a critical role in determining the superconducting properties as shown in figure 1.9. For YBCO superconductor, the charge carrier are holes.

By varying the carrier charge concentration through chemical substitutions or changes in the oxygen stoichiometry, the transport properties of the YBCO can be varied from superconducting to insulating (figure 1.10). It is well established[1.3,1.12] that YBCO can exist in at least two different structures, depending on the overall oxygen content and ordering of the oxygen atoms in the CuO basal planes. In the tetragonal phase (P4/mmm) the oxygen sites in the CuO basal planes are occupied at random and the material is insulating. The high-T_c YBCO (92K) compound posses orthorhombic (Pmmm) symmetry and exhibits complete ordering of the oxygen atoms in one-dimensional CuO chains along the *b*-axis, called *metallic chains* (see figure 1.3). For an oxygen content of **x** ~ 0.6, a tetragonal to orthorhombic phase transformation is observed (figure 1.11-a), and furthermore a decrease of the *c* parameter with increasing oxygen content is also observed (figure1.11-b).

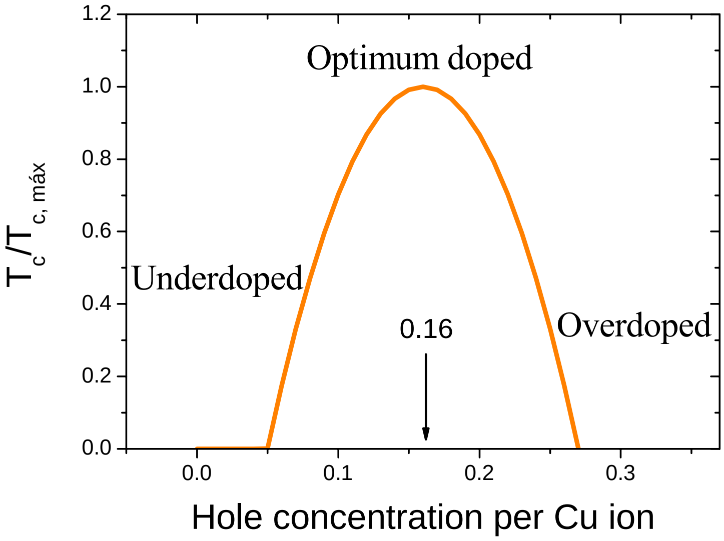

Figure 1.9. Doping curve of maximum charge carrier.

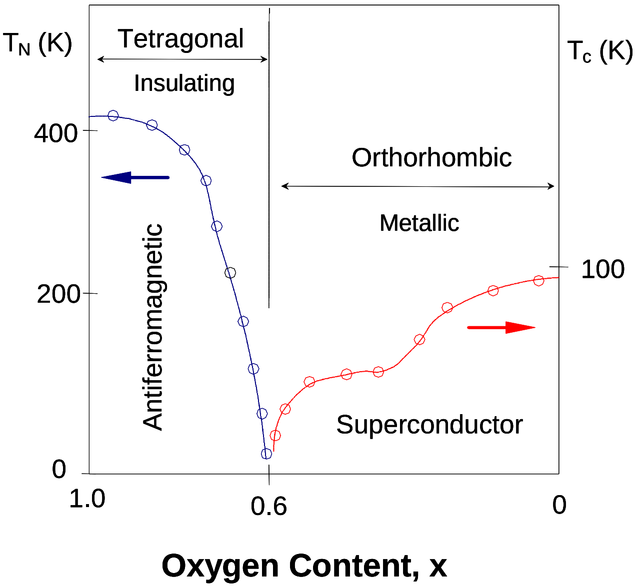

Figure 1.10. Oxygen content of $YBa_2Cu_3O_{7-x}$. Notice the phase transformation at **x** ~ 0.6.

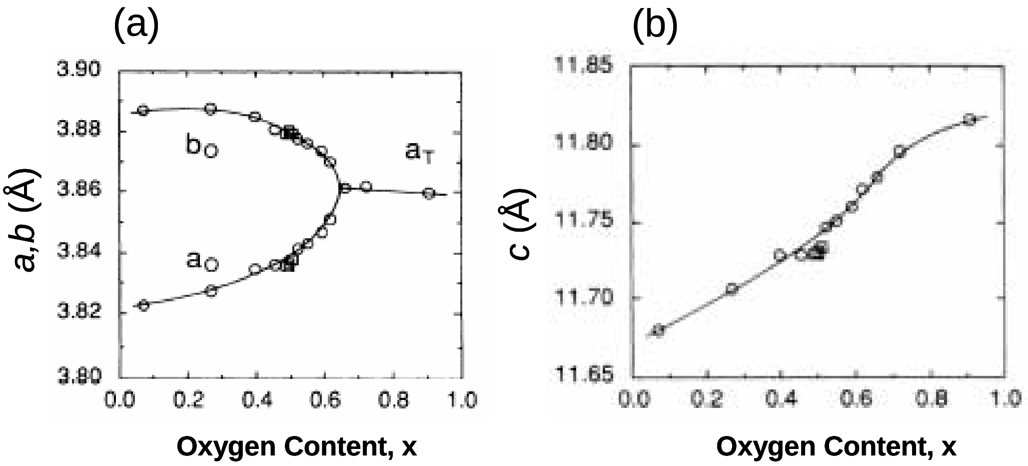

Figure 1.11. Unit cell parameters of YBCO as a function of the oxygen content[1.13].

1.3. Interest on Thin Films and Coated Conductors

Since the discovery of the first HTS[1.1], a significant effort has been put into the research and realization of epitaxial HTS films. Prior to 1986, all the superconducting applications were based on low-temperature superconducting materials, mainly Nb-Ti alloy (T_c ~ 9 K) and Nb_3Sn (T_c ~ 18 K). The first period of superconducting applications, from approximately 1962 to 1986, explored various power applications but found them too complex and expensive, thus relegating superconductivity to high-technology and medical applications where no competitors existed.

In early 1987, superconductivity in YBCO at 92 K was announced, well above the boiling point of liquid nitrogen (77 K). YBCO coated conductor represents the most promising HTS candidate for power application because of the demonstrated superior properties (*i.e.* high J_c, at high fields). This fact, dramatically changed the prospect of electrical power applications of superconductors, because of the significantly increased critical temperature where the employment of a more economical cryogen, liquid nitrogen becomes possible.

Coated conductors are seen nowadays to prompt the market of fault current limiters, transformers, power cables, motors, SMES, NMR, MRI. At the date, researches in laboratories of the world are focusing in the research and industrial production of YBCO CC highly biaxially textured.

1.3.1. First and Second Generation Tapes

Nowadays one can find two kinds of flexible and with high critical current density superconducting tapes, one of them, called *first generation of superconducting tapes*, are made by the *powder-in-tube* technique[1.15,1.16], where the tube is an Ag tube and the superconducting powder is the Bi2212 or the $Bi_2Sr_2Ca_2Cu_3O_y$ phases (with T_c's of 90 K and 110 K, respectively). In this technique, the tapes are made by sequential thermomechanical processing in which each iteration consists of a rolling plus a heat treatment sequence used to promote the uniaxial texture and densification of the BSCCO phase. An advantage of BSCCO over YBCO is the smaller sensitivity of its superconducting properties to high-angle grain boundaries and oxygen loss. At the date, textured tapes and wires of BSCCO superconductor are commercial available in long lengths (in order of kilometers), although its actual use is restrained to low field applications or temperatures below 25 K, due to its IL as we saw in section 1.2.3.

The second kind of tapes (coated conductors) are called, *second generation of superconducting tapes*. They are YBCO biaxially textured films grown onto metallic substrates and they are the only ones able to be used at high magnetic fields. In film form of 1 μm of thickness, YBCO is capable of transporting high critical currents in the order of $3MA/cm^2$ at 77K and $H_{ext} = 0$. In the next sections the architecture and processing techniques used for theses second generation tapes are presented.

1.3.2. Substrate

One of the most important materials issues in coated conductor growth concerns the choice of the right substrate and buffer layers. To obtain YBCO films of high quality, the substrate must have the desirable properties[1.17] such as: chemical compatibility, similar thermal expansion coeficient, good lattice matching with the YBCO phase, low roughness and must be flexible, hard, cheap and available in long lengths. Therefore for

YBCO coated conductor the substrate needs to have a metallic base over which other buffer layers can be grown epitaxially prior to the YBCO phase.

On another hand, buffer layers have been used extensively in the study of HTS films. These are films that are grown directly on the (metallic) substrate in order to alleviate some of the shortcomings that a substrate may have. The most common reason to use a buffer layer is to avoid unwanted reactions between film and substrate. Obviously, the buffer layer must be chemically compatible with both materials. Some reaction between the buffer layer and substrate may be permissible if it is confined to a region near the interface.

Buffer layers may serve other purposes, as well. If the thermal-expansion mismatch between the HTS layer and substrate is large, a buffer layer with intermediate thermal properties may alleviate cracking of the film. Choosing a buffer material with a lattice constant intermediate between the two materials may improve the epitaxial quality of the grown layer. The two mostly used techniques for growth on metallic substrates are: IBAD and RABiTS techniques, which we will briefly comment below.

1.3.2.1. IBAD Technique

The IBAD (Ion Beam Assited Deposition) technique characterized by a concurrent ion beam bombardment during growth of the buffer layer (YSZ, MgO or $La_2Zr_2O_7$) on polycrystalline metallic substrates (hastelloy, Ni, stainless steel), as shown schematically in figure 1.12a-b. This system is called the “dual-ion-beam sputtering system”. The group of Los Alamos National Laboratory (LANL) was one of the pioneers in the field of superconductivity[1.18].

In the IBAD process, a textured buffer layer is grown onto a polycrystalline metallic substrate. A strong $\langle 100 \rangle$ biaxial texture of the buffer layer is obtained with typical grain size is in the order of ~ 5μm. This textured buffer layer should transmit its texture, to the YBCO film.

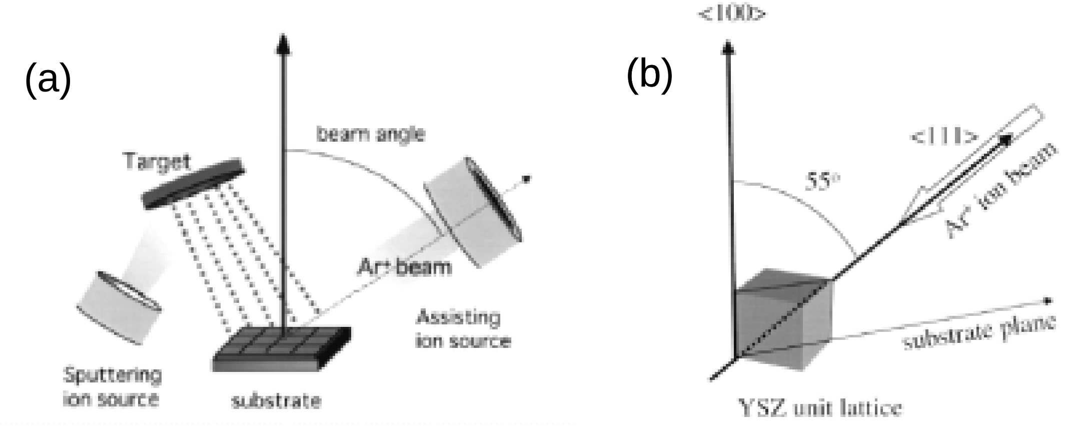

Figure 1.12. Schematic diagram: (a) of IBAD system and (b) alignment axes of YSZ unit lattice.

1.3.2.2. RABiTS Technique

The second method, development at Oak Ridge National Laboratory (ORNL)[1.19], is called RABiTS (Rolling Assisted Biaxially Textured Substrates). This inexpensive method[1.15,1.16] consists of using a biaxially textured metal substrate like pure nickel or certain nickel alloys. They are textured by a thermomechanical process with progressive cold-rolling deformation followed by annealing (figure 1.13). The resulting metal tape has a relatively sharp biaxial, 'cube' texture, with typical values $\Delta\omega \sim 4^o - 5^o$ degree, $\Delta\phi \sim 5^o - 6^o$ degree, grain size in the order ~50 μm and it is ~100μm in thickness. Then buffer layers can be epitaxially deposited on top prior the YBCO deposition. The low angle grain boundaries of the YBCO layers are a direct reflection of the low angle grain boundaries of the underlayer structures, as shown in figure 1.14.

Onto this Ni, Ni-alloys metal tapes, it is possible to grow oxide buffer layers like YSZ, CeO_2, Y_2O_3, to protect the metal from oxidation and to be a chemical barrier to reaction with the YBCO.

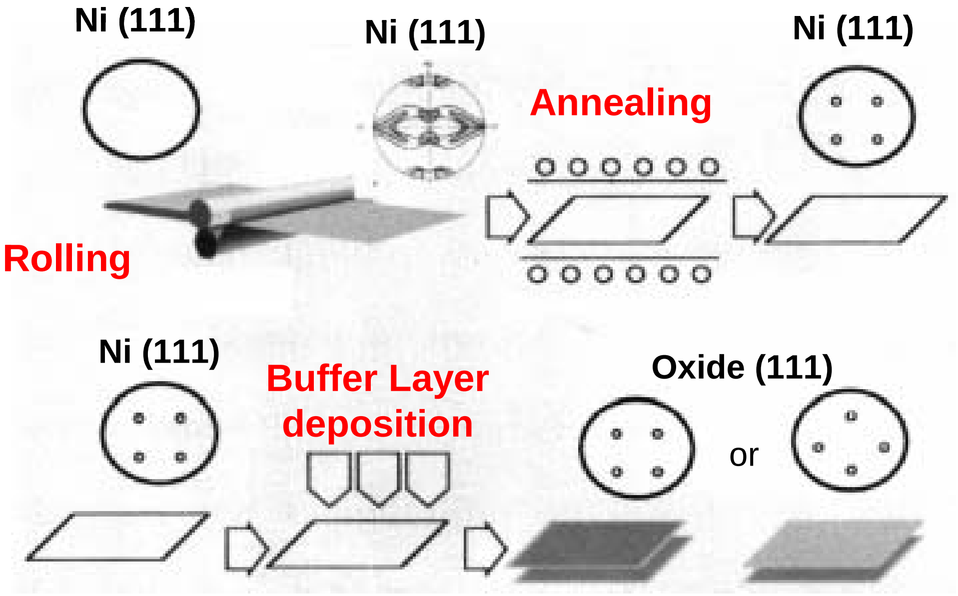

Figure 1.13. Schematic of the RABiTS technique with progression of pole figures.

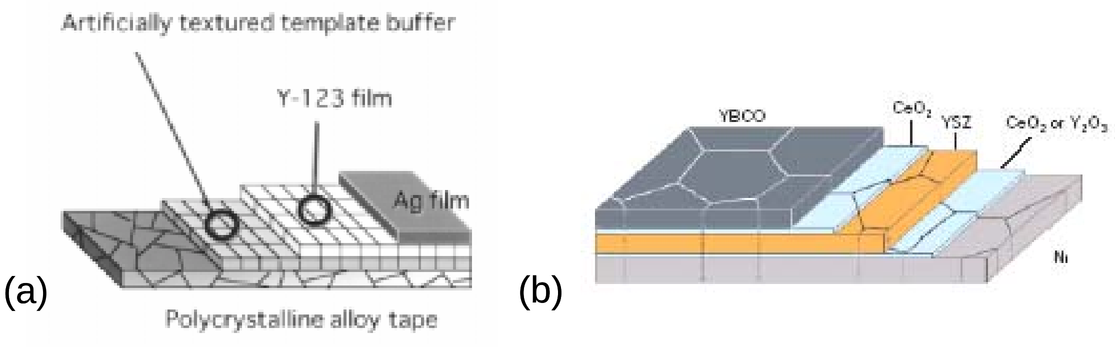

Figure 1.14. (a) A schematic description of biaxially aligned YBCO superconductor film using artificially textured template or buffer layer growth by IBAD. (b) Schematic description of YBCO superconducting tape grown onto textured nickel substrate by RABiTS process. Notice the grain boundary of the metallic substrate is transferred through the different layers.

1.3.3. General Methods for YBCO Film Growth

YBCO films of high performance require, as mentioned above, an epitaxial growth (figure 1.15b) and uniaxial growth is centainly not sufficient (figure 1.15a).

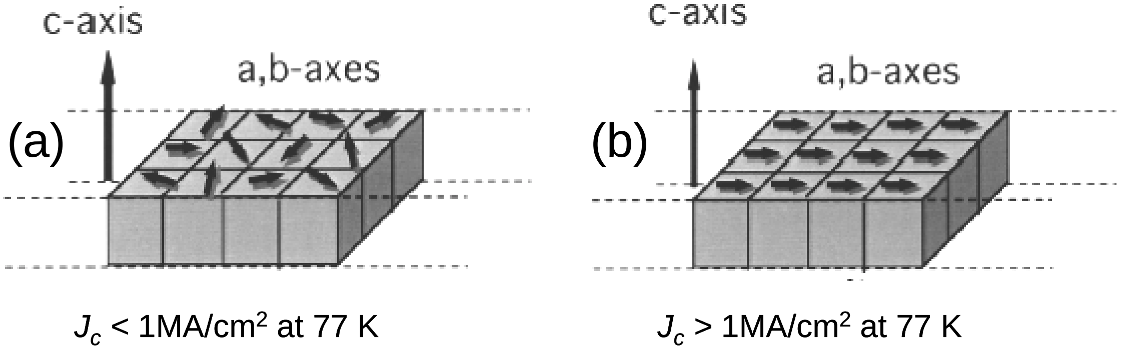

Figure 1.15. Schematic diagram for crystalline alignment structures of YBCO films (a) uniaxially aligned structure and (b) biaxially aligned structure.

Despite the synthesis of YBCO superconducting films is not trivial, several techniques to growth them exists, each one with a characteristic morphology, and then with associated physical properties. The growth of YBCO films falls into two major categories: physical and chemical methods, described below.

1. **Physical methods**: They are well-known and developed. Some examples of physical methods[1.21-1.24] are pulsed laser deposition (PLD), sputtering, molecular beam epitaxial (MBE) and BaF_2 process. Almost all these techniques require expensive high-vacuum systems to grow YBCO: Another disadvantage is the relatively slow rate of thin films growth and therefore long growth times are required to get films thick enough to carry high I_c.
2. **Chemical methods**: They are still not very well-known and under development, but have high potential to scale-up. Some examples of chemical methods[1.25-1.29] are metal organic decomposition (MOD), metal organic chemical vapor deposition (MOCVD) and liquid phase epitaxy. All these techniques do not require expensive high-vacuum systems to grow YBCO and therefore are low cost.

In this thesis, we studied different YBCO films and coated conductors provide by different laboratories. YBCO – IBAD textured tapes grown by PLD, in the laboratory of *Zentrum für Funktionswekstoffe* in Göttingen – Germany, YBCO – RABiT textured tapes grown by BaF_2 process, in the laboratory of the *Oak Ridge National Laboratory* in Tennessee – USA and textured thin films of YBCO – TFA grown in the laboratory of

ICMAB-CSIC in Barcelona. For this reason, I shall describe briefly the YBCO growth by PLD and BaF_2, and focus in more details on the TFA-MOD process.

1.3.3.1. PLD process

Pulsed-laser deposition (PLD) was popularized as an oxide film growth technique through its success in growing in situ epitaxial HTS films with high critical current density. In PLD, shown schematically in Figure 1.16, a pulsed laser is focused onto a target of the material to be deposited. For sufficiently high laser energy density, each laser pulse vaporizes or ablates a small amount of the material that is ejected from the target in a forward-directed plume. The ablation plume provides the material flux for film growth. The substrate must be located in a suitable position in the plume and be in contact with the heater to maintain the temperature for depositing well-aligned YBCO grains. Furthermore, both the total pressure of the atmosphere and oxygen partial pressure in the chamber must be precisely controlled to produce high-performance YBCO films. Epitaxial HTS films can be deposited by PLD using single, stoichiometric targets of the material of interest, or with multiple targets for each element. PLD has two intrinsic problems: it requires an expensive vacuum system and the high-power UV laser.

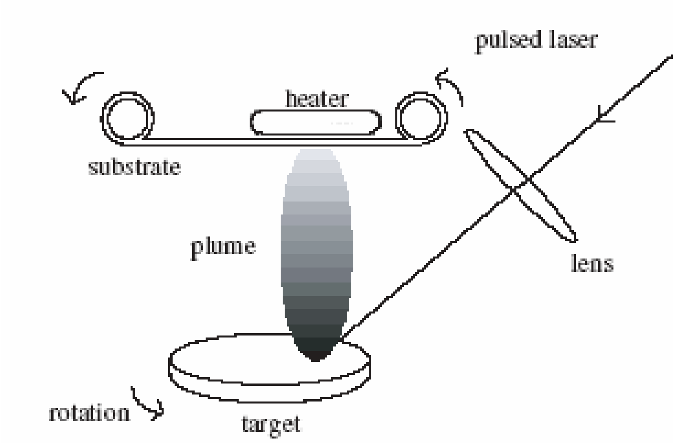

Figure 1.16. Sketch of pulsed laser deposition method for fabricating YBCO superconductors.

1.3.3.2. BaF_2 process

The precursor film is performed into a high-vacuum apparatus. This vacuum chamber includes electron guns for Y and Cu sources and a thermal heater for BaF_2, as represented in figure 1.17. The precursor film contains Y, Cu and BaF_2. After, the deposited precursor, the film is *ex situ* fired to become a YBCO superconductor film under humidified gas during the firing process. YBCO films produced by this *ex situ* process aims to replace the BaO phase in the precursor film by BaF_2 phase because of the difficulty of decomposing $BaCO_3$ during firing and the YBCO deterioration caused by CO_x derived from it[1.31]. Thick high-J_c YBCO films have actually been produced.

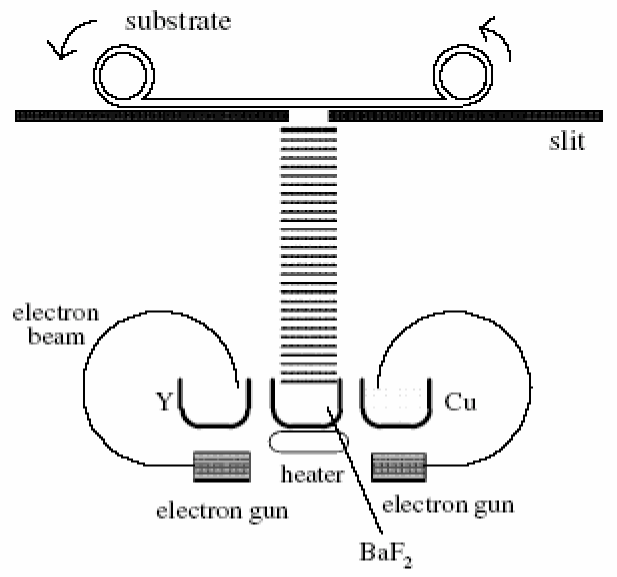

Figure 1.17. Sketch of deposition of precursor film using the BaF_2 process. Yttrium and copper are ablated to deposit precursor film by electron beams provided by electron guns. Only BaF_2 is heated by the heater and deposited onto the substrate.

1.3.3.3. TFA-MOD process

YBCO TFA-MOD was first reported by Gupta *et al* [1.30]. Large-area, uniform, high critical current density YBCO superconductor films are now routinely obtained by metalorganic decomposition using trifluoroacetates (TFA-MOD)[1.26,1.29]. This method has many advantages like as a precise control of the metal components (cations), a broad flexibility to coat large area surfaces and does not require any expensive vacuum apparatus at any time during the whole process. Thus, TFA-MOD is regarded as one of the most suitable candidates for fabricating YBCO long tapes (second generation of superconducting tapes) for many high-power applications at low cost.

The YBCO TFA-MOD samples studied in this thesis have been grown by members of the superconductivity group at ICMAB in the scope of *SOLSULET* project. The basic TFA process consists of four distinct steps: (1) precursor solution synthesis, (2) precursor solution coating, (3) pyrolysis of the organic material, and (4) YBCO nucleation and growth. Although they are separate processes, each step is dependent on the preceding steps in order to successfully fabricate a high-J_c YBCO film. The four major process steps and their adaptation to low cost manufacturing are summarized in the following sections.

1. **Precursor solution synthesis**. The TFA process mostly uses a precursor prepared by reacting a mixture of metal (Y, Ba, Cu) acetates with a stoichiometric amount of trifluoroacetic acid in an aqueous solution, drying the product to a viscous state, and then redissolving the product in methanol[1.29]. Subsequent improvements to the synthesis focused on reducing the free acid and water content in the precursor solution. The processing steps of this solution are schematically shown in figure 1.18.
2. **Precursor solution coating**. Deposition of the TFA precursor solution onto $SrTiO_3$ and $LaAlO_3$ single crystals, or flexible metallic substrate has been carried out by spin coating process, as represented in figure 1.19, or dip coating. In the spin-coating system, the coating solution was dripped onto a substrate and the solvent vaporized from the coating solution on the turning substrate to give a gel film.
3. **Pyrolysis process**. Precursor pyrolysis involves the thermal decomposition of the metalorganic salts and removal of the organic constituents of the precursor, leaving behind a mixture of nominally copper oxide, yttrium oxide, and barium fluoride. The process is carried out in a humid, oxidizing atmosphere at temperatures of <400 ^{o}C[1.29]. The thermal decomposition of TFA precursor films results in >50% reduction in film thickness and is accompanied by an increase of stress within the film.

The standard TFA-based precursor is very susceptible to cracking at decomposition temperatures corresponding to the increase in the stress versus temperature curve just above 200 °C shown in figure 1.19. In order to mitigate cracking in the film, the original temperature–time profile developed for the decomposition required nearly 20 hours.[1.29] Approaches to shortening the decomposition time or optimizing the thermal treatment are actually in study and mainly focused on reducing the stress by modifying the chemistry of the starting precursors.

4. **YBCO nucleation and growth**. The conversion of the decomposed precursor film to the $YBa_2Cu_3O_{7-x}$ phase is illustrated schematically in Figure 1.19. The conversion of the precursor to the YBCO results in ~50% reduction in film thickness. The initial step is the reaction of BaF_2 in the precursor film with H_2O, which requires transport of H_2O vapour into the film and removal of the resulting HF product. As the BaF_2 reacts, the $YBa_2Cu_3O_{6.5}$ phase nucleates at the buffer interface and continues to grow through the film thickness, as illustrated in Figure 1.19. Precise control of the reaction rate is required to promote the epitaxial nucleation of $YBa_2Cu_3O_{6.5}$ on the substrate (oxide buffer) surface and subsequent growth of the highly textured $YBa_2Cu_3O_{6.5}$ through the thickness of the film. As the film approaches the hold temperature (790 – 800 °C)[1.29], the $YBa_2Cu_3O_{6.5}$ begins to nucleate at the substrate (buffer) interface. The $YBa_2Cu_3O_{6.5}$ continues to grow through the thickness of the precursor as the film is held at the growth temperature. Finally, the film is slow cooled to ~ 450 ^{o}C into a dry oxydizing atmosphere to carry out the film oxygenation and thus transform the insulating tetragonal ($YBa_2Cu_3O_{6.5}$) to the superconducting orthorhombic ($YBa_2Cu_3O_{7-x}$) phase.

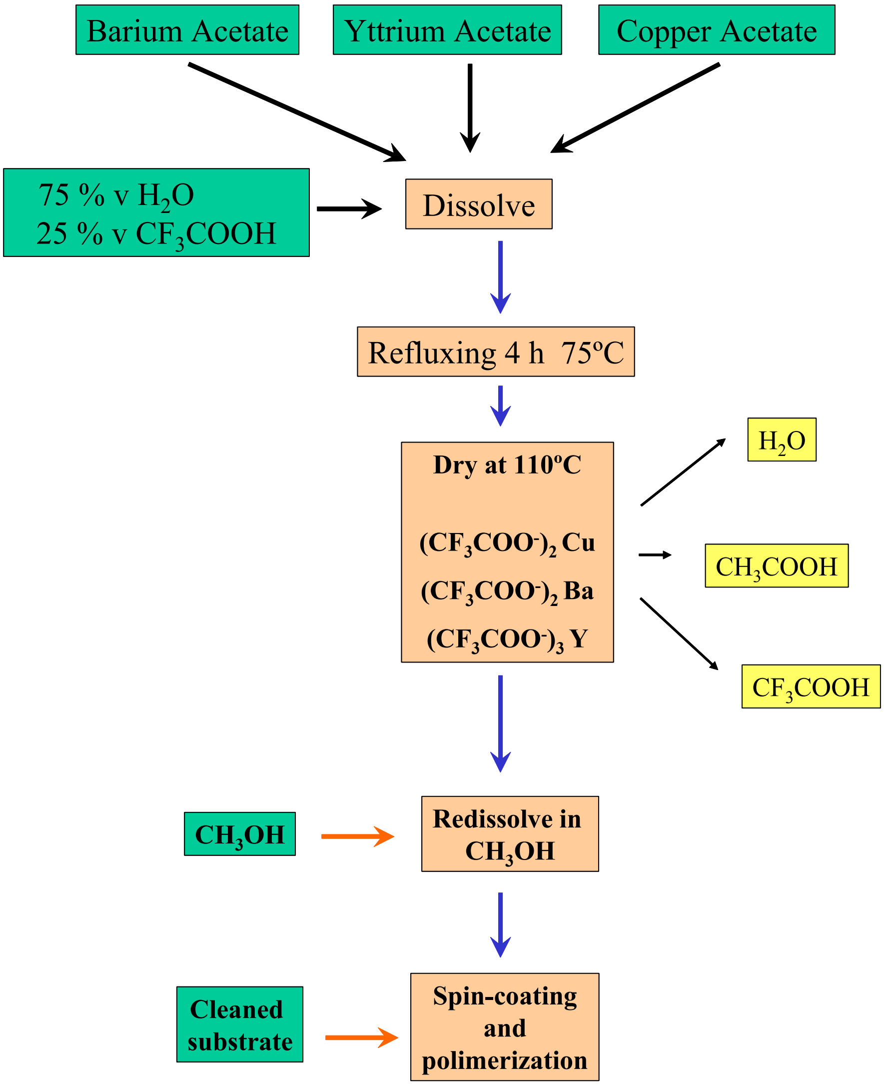

Figure 1.18. Process for preparing coating solution in TFA-MOD. Metal trifluoroacetates are synthesized with metal acetates and trifluoroacetic acid in water.

In this thesis we will show the high potential of micro-Raman technique to determine, control and optimize the growth of YBCO superconducting films onto single crystal and (buffer layer) metallic substrate. Thus, the next part of this chapter is a short revision on Raman effect and the optical phonon modes of YBCO, necessary to have a general idea about the study realized on YBCO films by micro-Raman spectroscopy.

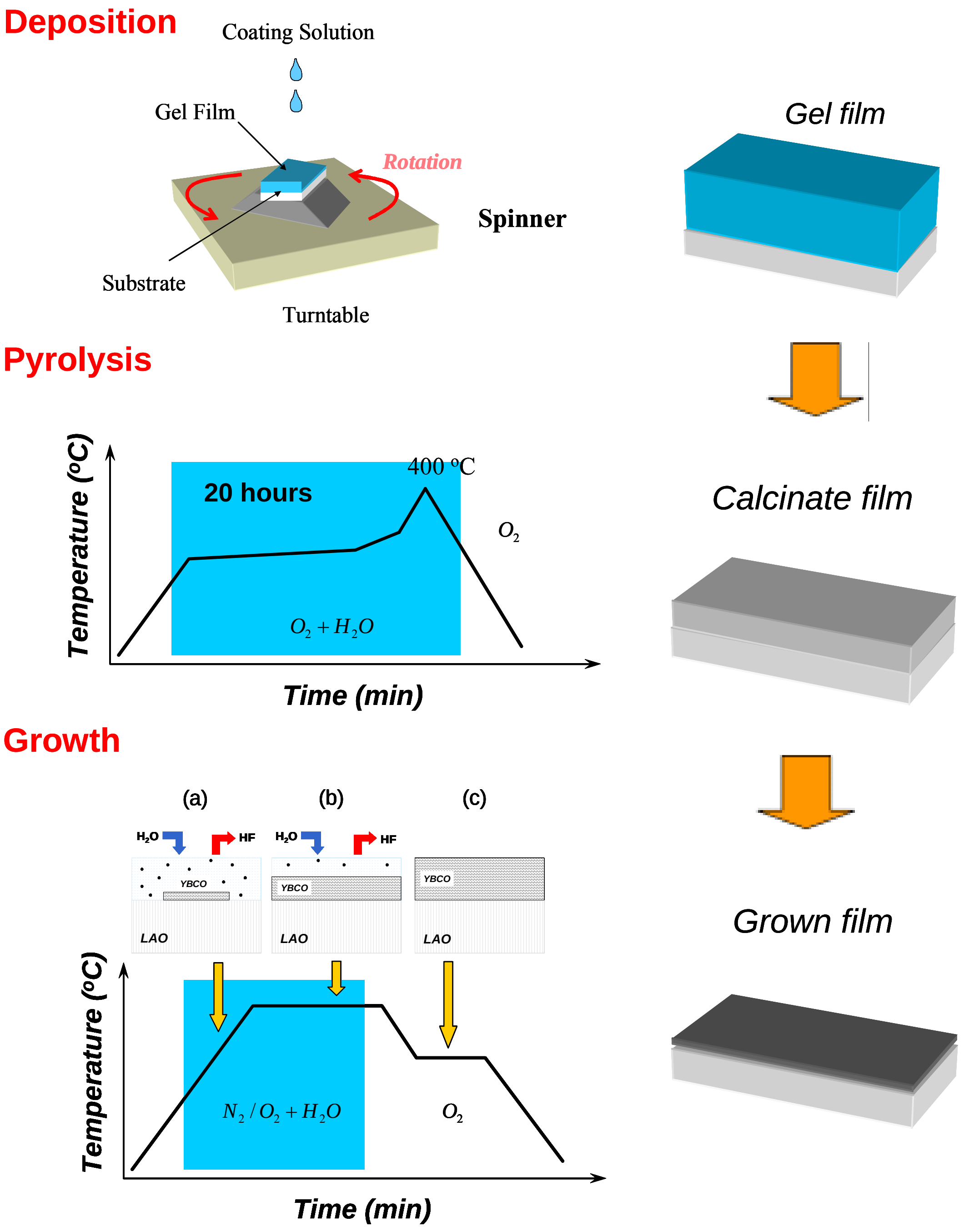

Figure 1.19. Schematic illustration of metalorganic deposition using trifluoroacetates (TFA-MOD) for fabricating YBCO superconductors. Coating solution is deposited to give a gel film on the substrate by spin-coating. The gel is pyrolyzed for the decomposition of trifluoroacetate-based precursor films and then become a precursor film. The precursor is converted to YBCO superconductor. Illustration of the (a) nucleation, (b) growth and (c) oxygenation of the YBCO phase from trifluoroacetates precursor film as a function of processing temperature and atmosphere. All these processes may be achieved in ambient pressure.

B. Introduction to Raman Spectroscopy

We present a brief introduction to the principles of Raman scattering in solids, describing the Raman active optical phonon modes observed for the YBCO compound. Theses results will be useful to determine and to characterize the composition and grain orientation of YBCO films from a detailed analysis of the intensity of the modes observed.

1.4. The Raman effect

The Raman scattering is the inelastic scattering of electromagnetic radiation (photons) creating (Stokes process) or annihilating (anti-Stokes process) an elementary excitation in the solid. The anti-Stokes process can occur only if the crystal is initially in an excited state. The elementary excitations can, among others, be phonons, plasmons, excitons or spin fluctuations.

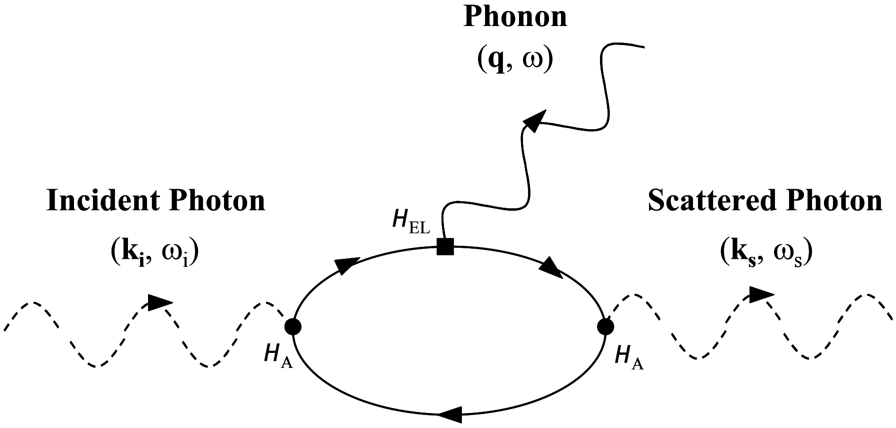

Figure 1.20. Feymann diagram which describe the first-order Raman scattering by lattice vibrations involving intermediate electron-hole pair states. H_A is electron-radiation interaction, and H_{EL} is the electron-lattice interaction.

In the present work we focus on the study of Raman scattering by phonons in YBCO films. Figure 1.20 shows schematically the mechanism of Raman scattering, for creating a phonon, which includes three steps[1.32]:

1. The external field, with frequency ω_i and vector wave $\mathbf{k_i}$, couples with the electronic system of the solid. Simultaneously with the anihilation of the photon incident an electron-hole pair is produced and electronic system changes from its initial value into a virtual intermediate level.
2. The transition of the electron-hole pair to another state with the creation of a phonon (Stokes process), with frequency ω and vector wave $\mathbf{q}$.
3. The recombination of the electron-hole pair creates the scattered phonon with frequency ω_s and vector wave $\mathbf{k_s}$.

Steps 1 and 3 involve the electron-radiation interaction (H_{A}) and step 2 the electron-phonon interaction (H_{EL}). Energy is conserved only in the total process, whereas wave vector is conserved in each step.

1.4.1. Kinematics of Inelastic Light Scattering Process

The kinematics of the inelastic scattering process in a crystalline solid is determined by conservation of energy and momentum. The conservation conditions can be written in terms of the wave vectors and frequencies of the photons and crystal excitation involved in the process.

$$\hbar\omega_i = \hbar\omega_s \pm \hbar q \qquad (1.2)$$

$$\mathbf{k_i} = \mathbf{k_s} \pm \mathbf{q} \qquad (1.3)$$

The plus and minus signs correspond to the Stokes and anti-Stokes process, respectively. Equation (1.3) allows us to limit the wave vector $\mathbf{q}$ to the portion of reciprocal space enclosed by the first Brillouin zone (BZ).

The magnitude of the scattering wave vector is determined by the scattering geometry. As indicated by figure 1.21, the minimum value of $|\mathbf{q}| \approx 0$ is obtained in forward scattering, when $\alpha = 0^o$. The maximum value of $|\mathbf{q}| \approx \frac{4\pi}{\lambda}$ is obtained in backscattering, when $\alpha = 180^o$.

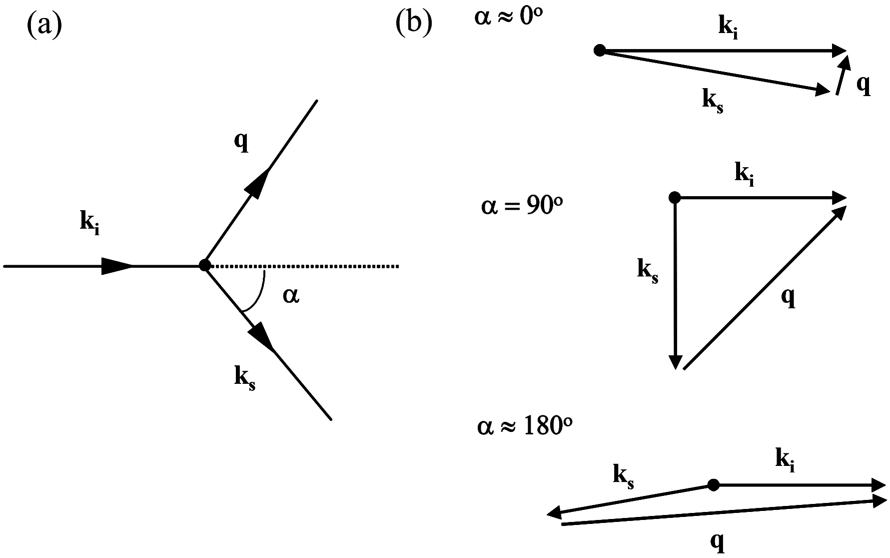

Figure 1.21. Kinematics of Stokes inelastic light scattering. (a) defines the scattering angle α. (b) Shows the magnitudes of **q** for forward, right angle and backward scattering geometries.

When applying equation (1.3) to Stokes Raman scattering by a crystal one must keep in mind that the wave vectors $\mathbf{k_i}$ and $\mathbf{k_s}$ of standard laser photons are very small compared with the linear dimensions of the BZ which are given by $2\pi/a \approx 1.65$ Å^{-1}, where $a \sim 3.8$ Å (for YBCO lattice constant $a \approx b \approx 3.8$ Å), while the magnitude of $\mathbf{k_i}$ and $\mathbf{k_s}$ is given by $2\pi/\lambda \approx 0.0012$ Å^{-1} (λ is the a laser wavelength ~ 5145 Å), a fact which leads to allowed scattering only for phonons with **q** close to the center of the BZ. Therefore only the phonons corresponding to $\mathbf{q} \approx 0$ are active in the optical spectra.

For crystals in which yhe translational invariance is strongly distorted as well as for amorphous solids, **k** conservation is not strictly required, in fact, the concept of **k** may even be irrelevant. Broad bands appear then in the Raman spectra instead of sharp peaks.

Usually, the Raman effect is treated either quantum-mechanically as a perturbation or classically as a microscopic change of the electronic susceptibility. The Raman scattering of phonons in a solid emerges from a linear coupling of the external electric field with the electronic system of the solid. The crystal responds to a disturbance with a change in the electric susceptibility by an excitation of the crystal.

1.4.2. The Raman Tensor

It is well established[1.32] that light is scattered inelastically by the spatial and temporal fluctuations in the electronic contributions to the electric susceptibility, which are associated with the elementary excitations of the crystal. In the case of light scattering by collective excitations such as phonons, the fluctuations result from the modulation of the electric susceptibility.

Within the framework of the classical theory for inelastic scattering we can write down the electric field related to the incident and scattered light $\mathbf{E_i}$ and $\mathbf{E_s}$, respectively, as

$$\mathbf{E_i} = \mathbf{e}_{\mathrm{i}}.E_{\mathrm{i}}^{0}.\exp\left[-i\left(\omega_{\mathrm{i}}.t-\mathbf{k}_{\mathrm{i}}.\mathbf{r}\right)\right] \tag{1.4a}$$

$$\mathbf{E_s} = \mathbf{e}_{\mathrm{s}}.E_{\mathrm{s}}^{0}.\exp\left[-i\left(\omega_{\mathrm{s}}.t-\mathbf{k}_{\mathrm{s}}.\mathbf{r}\right)\right] \tag{1.4b}$$

where the $\mathbf{e}_{\mathrm{i}}$ and $\mathbf{e}_{\mathrm{S}}$ are the unit polarization vectors for the incident and scattered photons, E_{i}^{0} and E_{s}^{0} are the corresponding amplitudes and $\omega_{\mathrm{i,s}}$ and $\mathbf{k}_{\mathrm{i,s}}$ the corresponding frequencies and wavevectors. The electric field of the incident light produces a polarization which is related to $\mathbf{E_i}$, in absence of any excitation of the scattering medium, by[1.33]:

$$\mathbf{P} = \varepsilon_o \overleftrightarrow{\chi}(\omega_{\mathrm{i}})\mathbf{E_i} \tag{1.5}$$

where $\overleftrightarrow{\chi}(\omega_{\mathrm{i}})$ is the first-order or linear electric susceptibility tensor of the medium at frequency ω_{i} which, in general, varies as a function of the incident photon energy. If the frequency ω of the scattered phonon is much smaller than the frequencies of the incident and scattered light, *i.e.* $\omega << \omega_{\mathrm{i}}, \omega_{\mathrm{s}}$, due to that $\overleftrightarrow{\chi}(\omega_{\mathrm{i}})$ is modified by thermally excited phonons with displacements of atomic order, and these displacements are small compared to the lattice constant, therefore the electric susceptibility tensor can be written as an expansion in powers series as a function of the phonon coordinates, Q, of the medium[1.34]:

$$\overleftrightarrow{\chi}(\omega, \mathrm{Q}) = \overleftrightarrow{\chi}(\omega) + \frac{\mathrm{d}\overleftrightarrow{\chi}(\omega)}{\mathrm{dQ}}\mathrm{Q} + \frac{1}{2}\frac{\mathrm{d}^2\overleftrightarrow{\chi}(\omega)}{\mathrm{dQ}^2}\mathrm{Q}^2 + \ldots \tag{1.6}$$

where Q can be written as:

$$\mathrm{Q} = \mathrm{Q}_{\mathrm{o}}.\exp[\pm i(\omega.t + \mathbf{q}.\mathbf{r})] \tag{1.7}$$

Here Q_{o} is the amplitude and ω and **q** are the frequency and the wavevector of phonon, respectively. The coefficients of this expansion (equation 1.6) are the Raman tensors of first, second, third order, etc, of the collective excitations, which describe the mixing of the incident and scattered fields with crystal normal modes. The effect of the phonons is to modulate the wavefunctions and energy levels of the medium[1.34]. The changes in these quantities are linear in Q to the first order in perturbation theory, and their effect is represented macroscopically by an additional contribution to the electric susceptibility. Inserting equations (1.6) and (1.7) into (1.5) we obtain the induced polarization:

$$\mathbf{P} = \mathbf{P_0} + \mathbf{P_1} + \ldots = \varepsilon_o \overleftrightarrow{\chi}(\omega_{\mathrm{i}})\mathbf{E}_i + \varepsilon_o\left(\frac{\mathrm{d}\overleftrightarrow{\chi}(\omega)}{\mathrm{dQ}}\mathrm{Q}\right)\mathbf{E}_{\mathrm{i}} + \ldots \tag{1.8a}$$

$$\mathbf{P_0} = \varepsilon_o \overleftrightarrow{\chi}(\omega_{\mathrm{i}})\mathbf{E}_i \tag{1.8b}$$

$$\mathbf{P_1} = \varepsilon_o\left(\frac{\mathrm{d}\overleftrightarrow{\chi}(\omega)}{\mathrm{dQ}}\right).\mathrm{Q}_0.E_i^0.\exp[-i\{(\omega_{\mathrm{i}} \pm \omega).t - (\mathbf{k}_{\mathrm{s}} \pm \mathbf{q}).\mathbf{r}\}] \tag{1.8c}$$

The first-order polarization, equation (1.8b), oscillates at the same frequency as the incident field and contributes only to elastic scattering (Rayleigh scattering), while the second-order polarization, equation (1.8c), oscillates at frequencies different from ω_i because Q is itself a time-dependent function[1.33,1.34]. This part of the polarization radiates the inelastic contribution (Raman scattering). That means, the term $\mathbf{P_1}$ describes a *radiatory dipole* with frequency $\omega_s = \omega_i \pm \omega$. The wavevector for the emitted light $\mathbf{k}_s$ has to fulfill the relation $\mathbf{k}_s = \mathbf{k}_i \pm \mathbf{q}$. Here the – sign refers to *Stokes* and the + sign to *Antistokes* scattering.

The second-rank Raman tensor, $\overleftrightarrow{\mathbf{R}}$, can be considered like a *response function*[1.35] for light scattering, which relates the incident field to the scattered field. There is one such tensor associated with each particular excitation; each of them contains the corresponding polarization selection rules for light scattering. Away from electronic resonance and for scattering by phonons, the Raman tensor is proportional to the derivative of the electric susceptibility with respect to the phonon coordinate[1.36]:

$$\mathbf{R} \propto \frac{d\chi(\boldsymbol{\omega}_i)}{\mathbf{dQ}} \tag{1.9}$$

the phonon modulates the susceptibility at its frequency ω. Since the electric susceptibility $\bar{\chi}$ is a symmetric second-rank tensor, so will be $\bar{\mathbf{R}}$.

The total scattering into a solid angle *d*Ω associated with particular excited state of the sample is determined by the differential cross section[1.36]:

$$\frac{d\sigma}{d\Omega} \approx \frac{\omega_i^4 \omega_s V_c}{\mathbf{c}} \left| \mathbf{e}_s \cdot \frac{d\chi(\omega)}{dQ} \cdot \mathbf{e}_i \right|^2 \tag{1.10}$$

where V_c is the scattering volume. The differential cross section defines the intensity and the shape of Raman spectra. The intensity of the scattered Raman radiation is proportional to the square of the susceptibility derivative with respect to the normal vibration coordinate, i.e. it depends on the variation of electric susceptibility during vibration[1.32]:

$$I_R \approx \left| \mathrm{e}_s \cdot \frac{d\overset{\leftrightarrow}{\chi}(\omega)}{dQ} \cdot \mathrm{e}_i \right|^2 \tag{1.11}$$

Rewriting (1.11) by (1.9) we obtain that the Raman intensity is proportional to:

$$I_R \approx \left| \mathrm{e}_s \cdot \overset{\leftrightarrow}{\mathrm{R}} \cdot \mathrm{e}_i \right|^2 \tag{1.12}$$

where $\mathbf{e}_\mathrm{i}$ and $\mathbf{e}_\mathrm{s}$ are the unit polarization vectors for the incident and scattered photons.

1.4.3. Light Scattering Selection Rules

In addition to the conditions imposed by the kinematics of the scattering process, there is another requirement which determine the appearance in the Raman spectrum of a band corresponding to a given vibration mode. If the vibration mode produces a change of the electric susceptibility, *i.e.* if[1.32]:

$$\frac{d\overset{\leftrightarrow}{\chi}(\omega)}{dQ} \neq 0, \tag{1.13}$$

it is active in the Raman spectrum. From the point of view of the Raman tensor, the symmetry of the Raman tensor, determines the selection rules of the permitted vibrational modes in a particular scattering configuration. One Raman mode is permitted for a determined scattering configuration when the result of contracting the unit polarization vectors $\mathbf{e}_\mathrm{s}$ and $\mathbf{e}_\mathrm{i}$ with the Raman tensor is different from zero[1.36].

$$\mathrm{e}_s \cdot \overset{\leftrightarrow}{\mathbf{R}} \cdot \mathrm{e}_i \neq 0 \tag{1.14}$$

$\mathbf{e}_\mathrm{i}$ and $\mathbf{e}_\mathrm{s}$ are the electric-field vectors of the incident and scattered light that define the scattering configuration with respect to the crystal axis.

1.5. Raman phonons of YBCO superconductor

The vibrations of the atoms in a solid occur in what are called *normal modes*. These involve the coherent oscillations of atoms in the unit cell relative to each other at a characteristic frequency (phonon frequency). The oscillations occur in such a manner that the center of gravity (center of inversion) is preserved.

Most HTS are centrosymmetric crystals. Their elementary excitations (phonons) are either odd or even. Raman spectroscopy, involving two photons (each of them odd) only couples to even excitations. IR spectroscopy involves only one photon and couples therefore only odd excitations.

1.5.1. The A_g- and B_{1g}-Modes

Spectroscopists[1.37] have developed a notation of these modes based on characteristic of the oscillations. The one-dimensional A and B modes refer to atoms motions parallel to *c*-axis, i.e., in the vertical (z) direction. The A mode is symmetrical for 90^o rotation around z, which means that all the arrows on the atoms of figure 1.22.a are coincident under this operation. The B mode is antisymmetrical under this 90^o rotation, so that the arrows reverse direction as it is shown in figure 1.22.b. The subscript 1 is for a mode which is symmetrical for a 180^o rotation about x or y, while the subscript 2 is for a mode which is antisymmetrical for this rotation.

The even, or *gerade* (*g*), vibrations, which preserve this center of symmetry, are said to be symmetric with respect to inversion and the odd, or *ungerade* (*u*), vibrations, are antisymmetric with respect to inversion.

There are also two-dimensional modes E_g and E_u involving atoms motions in the ab-plane, but these are more difficult to characterize.

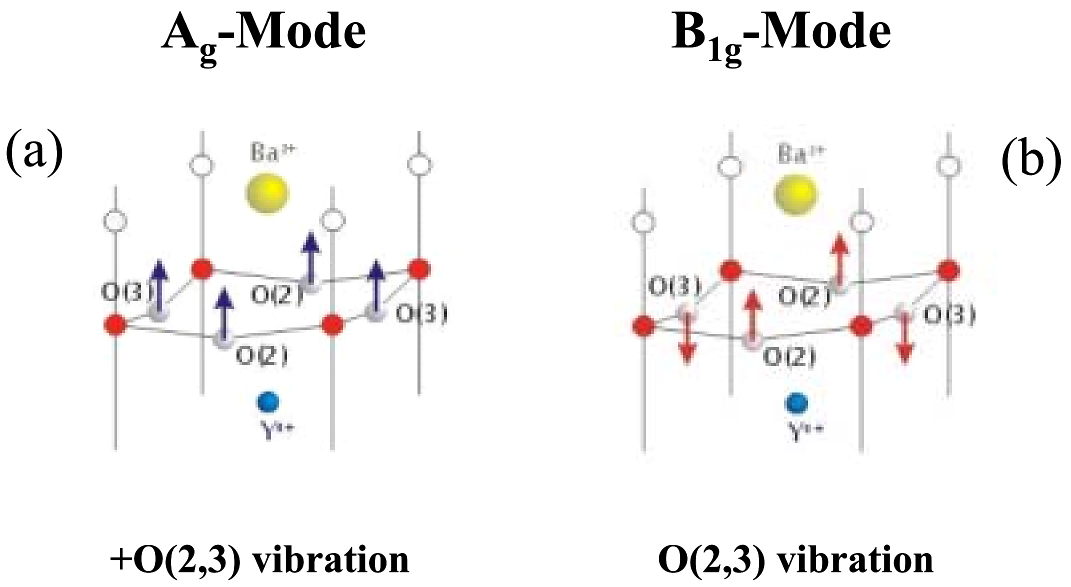

A_g-Mode

B_{1g}-Mode

+O(2,3) vibration

O(2,3) vibration

Figure 1.22. Representation of (a) A_g- and (b) B_{1g}-mode.

1.5.2. Optical Phonon Modes of YBCO

The YBCO superconductor has an orthorhombic unit cell that belongs to the space group *Pmmm* (D_{2h}^1) and point group *mmm* (D_{2h}). These groups have an inversion center, so that optical modes near to **q** = 0 cannot be both Raman and Infrared active. There is at least one site which has the full symmetry of the point group. It may be seen from figure 1.3 that this is indeed the case for the sites of the O(1), Cu(1) and Y atoms. The pairs of atoms O(2), O(3), O(4), Ba and Cu(2) have lower, C_{2v} symmetry. Permutation of the equivalent atoms in the C_{2v} pairs leads to the irreducible representations A_g and B_{1u} of D_{2h}.

The corresponding modes are obtained by multiplying these representations by those of the displacements vectors in x, y and z directions (representations B_{3u}, B_{2u} and B_{1u}). From standard tables one finds three odd (*ungerade*) modes B_{3u}, B_{2u}, B_{1u}, and three even (*gerade*) modes A_g, B_{2g} and B_{3g} for each member of a pair, as shown in table 1.3.

Table 1.3.

Atom	**Site Symmetry**	**Even modes**	**Odd Modes**
Y, Cu(1), O(1)	mmm D_{2h}	---------------------	B_{1u} , B_{2u} , B_{3u}
O(2), O(3), O(4) Ba, Cu(2)	mm2 C_{2v}	A_g , B_{2g} , B_{3g}	B_{1u} , B_{2u} , B_{3u}

For the vibrations involving the atomic positions with full symmetry we find only three odd modes for each atom. After subtracting the three acoustic modes we arrive at 36 optically active modes to be considered in YBCO[1.35]:

$$\Gamma = 5A_g + 5B_{2g} + 5B_{3g} + 7B_{1u} + 7B_{2u} + 7B_{3u}. \tag{1.15}$$

Of these, 15 are Raman active according to symmetry and 21 infrared active (Table 1.4). In many cases these activities are negligibly small. For instance, B_{2g} and B_{3g} Raman optical modes with displacements in x- and y-directions respectively, are usually more weaker than vibrations in z-direction (10 to 100 times)[1.38]; for this reason, we ignored the B_{2g} and B_{3g} modes in our study. In table 1.5 we give the character table for these modes and their optical activities.

Table 1.4. Active modes in YBCO

Raman Active Modes	$5A_g$, $5B_{2g}$, $5B_{3g}$
IR Active Modes	$7B_{1u}$, $7B_{2u}$, $7B_{3u}$

Which of the expected modes will actually be observed in an experiment depends on a number of additional physical aspects of these modes. To be observed in IR spectra, a mode must show a significant charge displacement (dipole moment), a requirement for which group-theorical IR activity is necessary but not sufficient. It can sometimes be concluded from specific models for the ionic charges and the expected displacement of those ions that a mode is actually nearly silent, *i.e.*, it shows no appreciable activity although it is IR allowed. An important example is a mode related to the silent (IR and

Raman forbidden) mode of the perovskites. The physical reason for the latter being IR forbidden is that the oxygen ions situated on contiguous faces of the perovskite unit cell vibrate out of phase in z-direction thus yielding no net dipole.

Table 1.5. Optical activities for YBCO modes.

Representation	**Optical Activity**
A_g	$\alpha_{xx}, \alpha_{yy}, \alpha_{zz}$ (Raman)
A_u	Silent
B_{1g}	α_{xy} (Raman)
B_{1u}	IR(z)
B_{2g}	α_{xz} (Raman)
B_{2u}	IR(y)
B_{3g}	α_{yz} (Raman)
B_{3u}	IR(x)

Sometimes it is useful to analyze a system with higher symmetry (like YBCO tetragonal) if the system under consideration possesses approximately that symmetry, broken by a weak perturbation of lower symmetry. Transitions or modes forbidden for higher symmetry may be expected to appear only weakly, even if they are allowed, in the actual system. The higher-symmetry modes may have different selection rules which will be fulfilled approximately in the lower-symmetry system, a fact which should help to identify some modes.

The YBCO orthorhombic structure is a light deformation of tetragonal structure (higher symmetry, $a \approx b$). Therefore, for the five orthorhombic eigenmodes, one mode corresponding to a tensor that it has practically the B_{1g}-mode symmetry of tetragonal structure, in the same way the other four modes have a symmetry practically the same to the A_{1g}-mode symmetry of tetragonal structure, as shown in figure 1.23 the *split* of five A_g modes into four A_{1g} modes and one B_{1g} mode. Therefore, historically they are five

YBCO modes labelled with labels of tetragonal modes (B_{1g}- and A_{1g}-modes) although we have, strictly speaking, an orthorhombic group with five A_g-modes.

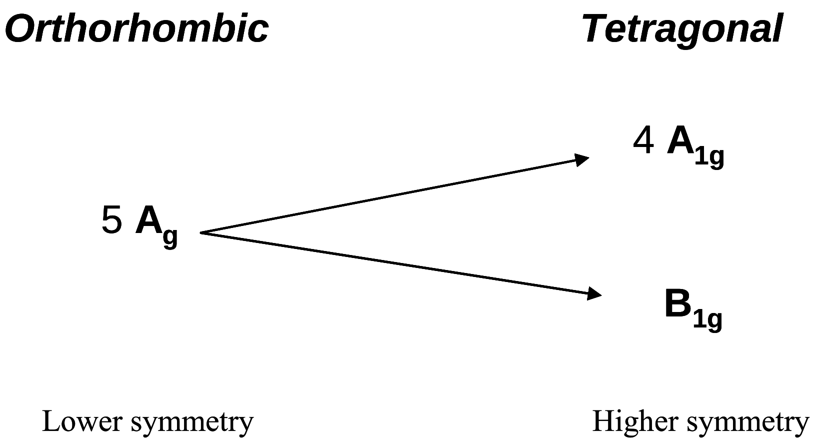

Figure 1.23. Higher- and lower-symmetry of YBCO.

1.5.3. The Raman Spectra of YBCO

We will mainly consider the canonical YBCO superconductor. Its unit cell is shown in figure 1.3. The sites of the Y, Cu(1) and O(1) atoms are inversion centers. The corresponding vibrations of these atoms are thus odd upon inversion and therefore Raman inactive. The remaining atoms are not at centers of inversion. They thus appear as pairs of equivalent atoms connected by the inversion. They give rise to odd (both atoms moving in the same direction) and even (motion in opposite directions) vibrational patterns. The corresponding pairs of IR- and Raman-active vibrations are sometimes called *Dadidov doublets*. The even vibrations along z appear to be much stronger in the Raman spectra than their x-y counterparts, and are shown in the figure 1.24[1.39].

For the YBCO orthorhombic structure, five z-polarized Raman phonons exist. The lowest frequency z-polarized Raman phonon involves mainly the vibrations of the heaviest Barium atom (Ba) at 115 cm^{-1} frequency, the next lowest vibrations involving those of the copper atoms Cu(2) at 150 cm^{-1} frequency. The remaining three modes are dominated by vibrations of O(2) and O(3) oxygens atoms at 340 and 440 cm^{-1} frequencies respectively, both frequencies including both oxygen atoms and they are involving symmetric and antisymmetric vibrations (we shall denote the symmetric vibration like +O(2,3) and antisymmetric vibration like O(2,3)). Finally the vibration of the apical oxygen O(4). All theses characteristic frequencies and symmetries are shown in figure 1.24 and table 1.6, respectively.

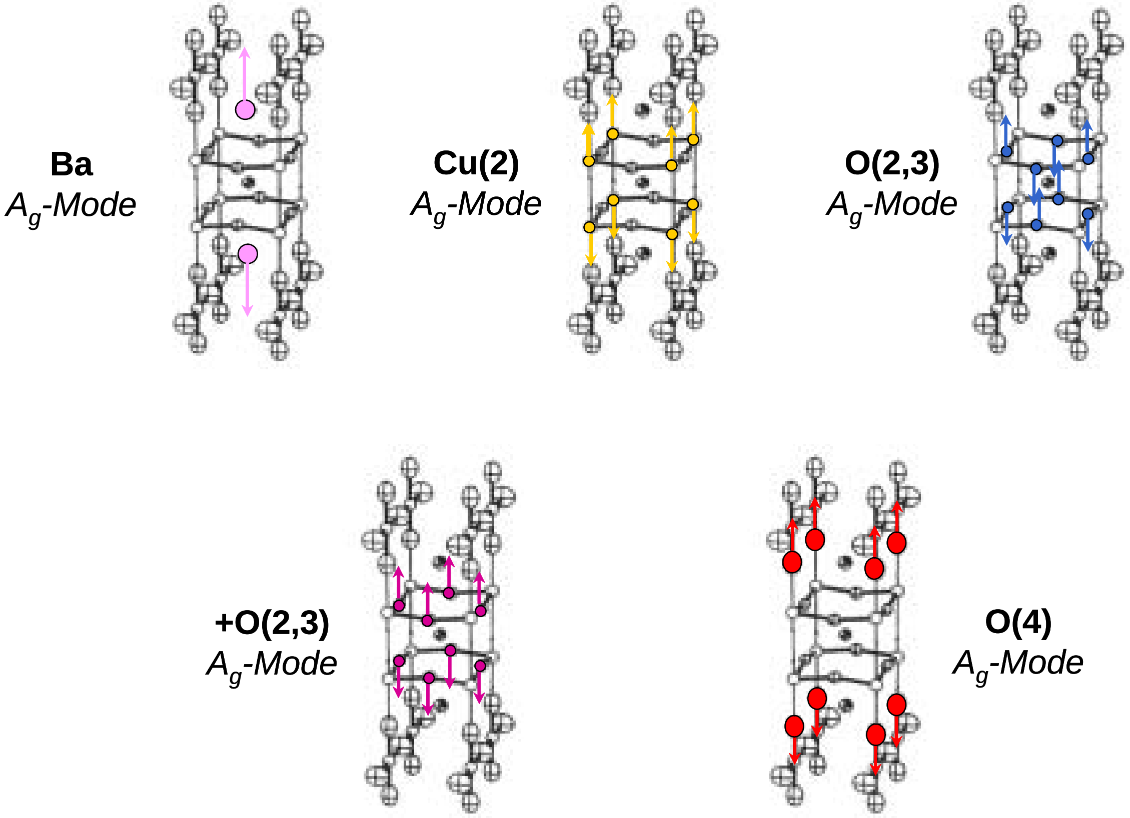

Figure 1.24. Schematic representation of z-vibration of optical active Raman modes of YBCO[1.39].

Table 1.6.

z-polarized Raman phonons of YBCO

Atom	Frequency (cm^{-1})	Symmetry
Ba	115	A_g
Cu(2)	150	A_g
O(2,3)	340	B_{1g}
+O(2,3)	440	A_g
O(4)	500	A_g

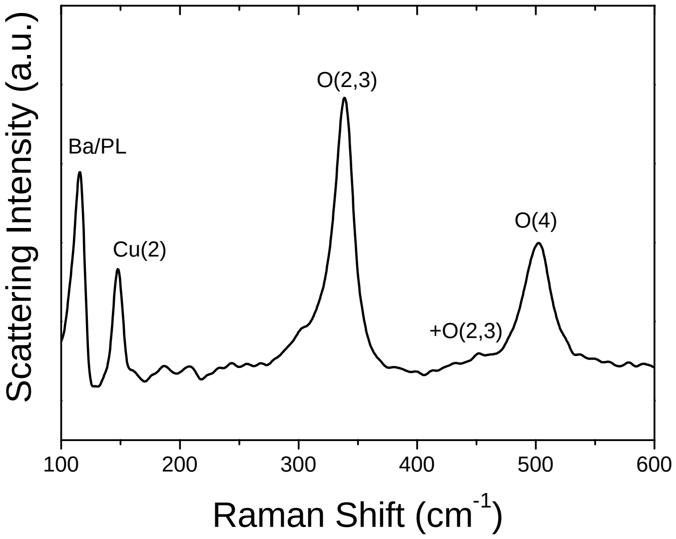

Figure 1.25. Typical z-polarized Raman spectra of epitaxial YBCO film. Notice the oxygen Raman modes at high frequencies while Cu(2) and Ba modes at low frequencies. The barium A_g-mode is overlapped with the plasma line at 117 cm^{-1}.

Its possible to know the expected optical Raman modes of samples under analysis by contraction of the irreducible representations of the Raman tensor with the vector indicating the direction of the incident and scattered light polarization. In table 1.7, we show the irreducible representations of the Raman tensors for the orthorhombic and tetragonal point groups that will be used along this thesis. Many HTS belong to these two point groups, this makes possible to find the direction of the crystallographic axis of the superconducting grains in YBCO film, *i.e.*, to obtain the orientation of the grains respect to the substrate or axes.

Therefore, the intensity of the Raman profiles has a strong dependence on the scattering geometry and relative orientation among the sample, the incident and scattered light polarization directions (selection rules). This fact, made possible to find the direction of crystallographic axis of the crystals in YBCO film. Thus, micro-Raman spectroscopy is a powerful tool of non-destructive analysis, because the samples no required any previous preparation for their characterization, in comparison with other analysis techniques. It is also possible to obtain information about composition, impurities, secondary phases, defects and grain sizes, in YBCO films prepared by physical and chemical methods, which are issues to show and to discuss in the following chapters.

Table 1.7.

Irreducible representations of the Raman tensor used in the present work

Orthorhombic D_{2h}

$$\begin{pmatrix} x_{A_g} & & \\ & y_{A_g} & \\ & & z_{A_g} \end{pmatrix}$$

Tetragonal D_{4h}

$$\begin{pmatrix} x_{A_{1g}} & & \\ & x_{A_{1g}} & \\ & & z_{A_{1g}} \end{pmatrix} \quad \begin{pmatrix} x_{B_{1g}} & & \\ & -x_{B_{1g}} & \\ & & 0 \end{pmatrix}$$

Chapter 2

Experimental Techniques

In this chapter, we will briefly describe the experimental techniques used in this thesis for the physical characterization of YBCO films like micro-Raman spectroscopy, x-ray diffraction, scanning electron microscopy, resistivity, transmission electron microscopy and critical current density. Measurements of resistivity, transmission electron microscopy and critical current density presented in this thesis have been actually performed by other members of the superconductivity group. We present the results here in order to complement the other measurements and be able to have a complete understanding of the different subjects. Because this thesis mostly focuses on the use of micro-Raman spectroscopy as a very powerful tool for non-destructive characterization of YBCO films and CC, we will describe this technique in more detail than the others.

2.1. Instrumentation for micro-Raman Spectroscopy

The instrumentation used to perform micro-Raman spectroscopic studies of YBCO films and CC, in the Raman laboratory at the Universitat Autónoma de Barcelona (UAB) in collaboration with the ICMAB is shown in figures 2.1 and 2.2. It consists of the following parts, that they will be considered separately:

1. Sample holder with fixed X-Y or rotation stage of the microscope.
2. Laser source.
3. Collection optics to collect the Raman scattered photons.
4. Monochromator to separate the Raman signal into its constituent wavelengths.

5. A liquid nitrogen cooled charge coupled device (CCD) detector to collect the Raman scattered photons.
6. A computer system to make optimum use of the photons collected and to store and to display the spectra.

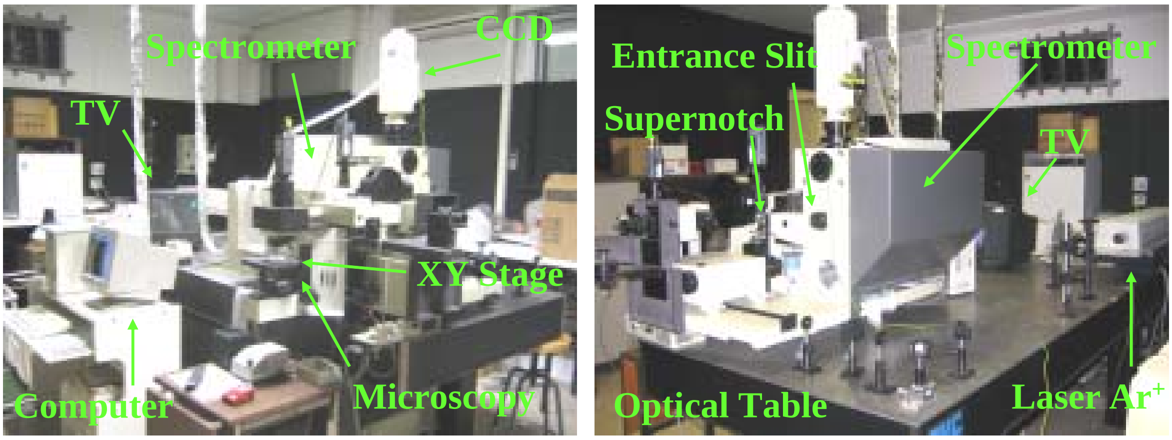

Figure 2.1. (a) Right- and (b) left-side view of Raman laboratory at UAB.

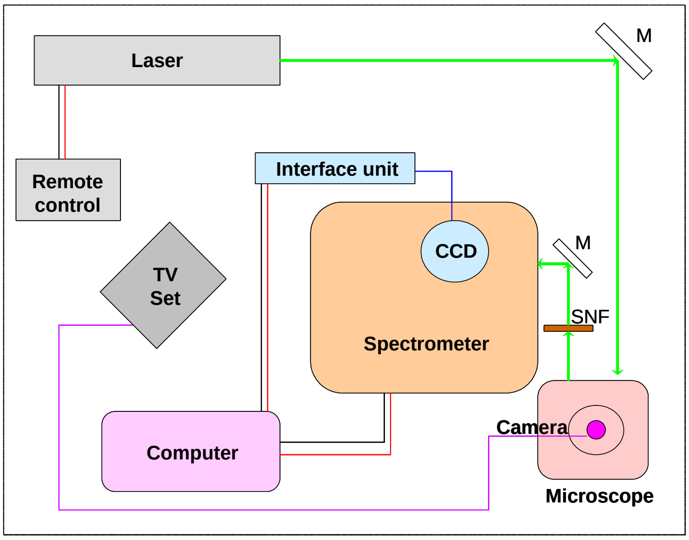

Figure 2.2. Draw top-view of Raman laboratory at UAB.

2.1.1. Sample Holding

An X-Y manual microscopy stage (figure 2.3a) was used for measurements and detection of: uniaxial texture, Raman mapping, Raman lineal scans, impurity and secondary phases. On the other hand, for measurements of the biaxial texture of the samples a manual microscope rotation stage was used (figure 2.3b).

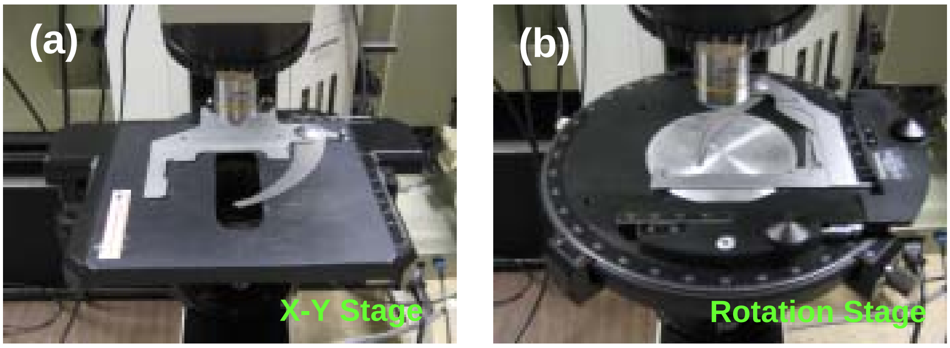

Figure 2.3. (a) X-Y stage and (b) Rotation stage of microscope.

2.1.2. Laser Source

The BeamLok Argon ion laser system from *Spectra Physics* (figure 2.4) consists of a BeamLok laser head, plasma tube, a power supply Model 2580, a remote system control module Model 2470 and a BeamLok remote control module Model 2474. These components are schematelly displayed in Figure 2.5.

This kind of laser required water cooled for refrigeration (inlet temperature 10 – 35 ^{o}C). The nominal laser power work range was between 75 – 150 mW, depending on the collection optics used and on the measurements performed. The laser power onto the sample was kept below ~ 90 kW/cm^2 to avoid degradation on the films due to overheating of the proved volume.

Well-defined variations in the spatial distribution of the electromagnetic field perpendicular to the direction of travel of the beam are called transverse electromagnetic modes (*TEM*). These variations determine, in part, the power distribution across the beam. For normal laser operation mode a Gaussian profile (TEM_{00}) was used. Other modes have different irradiance contours and are identified by the number of nulls in the irradiance distribution[2.1]. Finally, there exists an interferential filter to filter the plasma lines of the laser source before the entrance of the optical microscope.

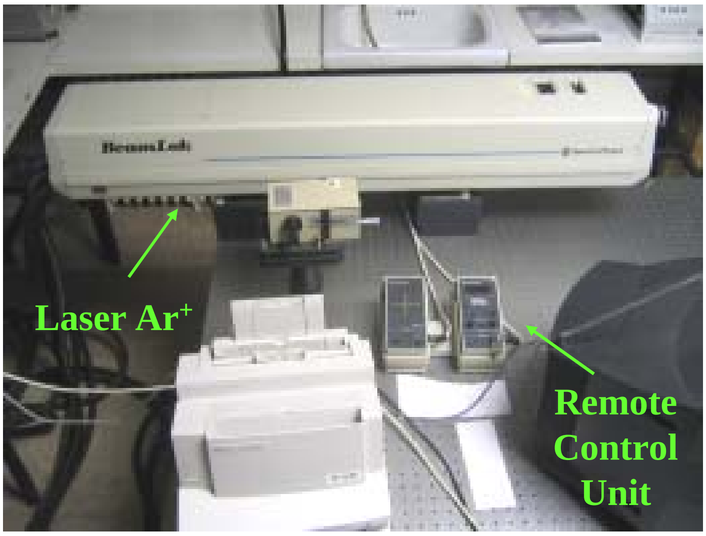

Figure 2.4. Spectra Physics BeamLok 2080 Argon-ion laser.

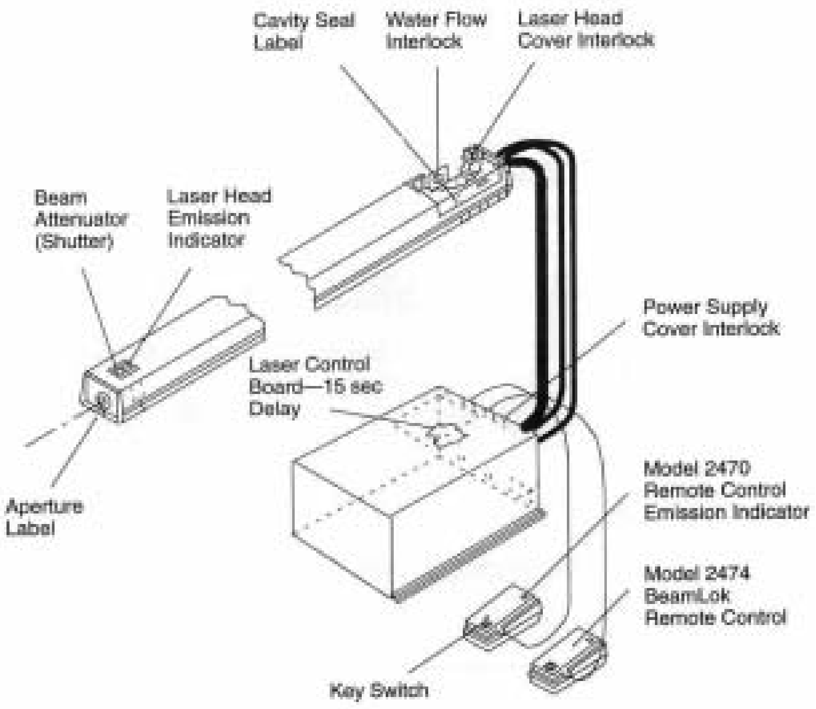

Figure 2.5. BeamLok 2080 radiation control drawing

2.1.3. Optics

The focusing and collection optics consists of a metallographic microscope *Olympus* model BX40 (figure 2.6) with three plano-achromatic objectives: X10, X50 and X100, optically adapted to the aperture of the instrument. They produce a focused laser spot of approximately 10, 5 and 1 μm in diameter, respectively.

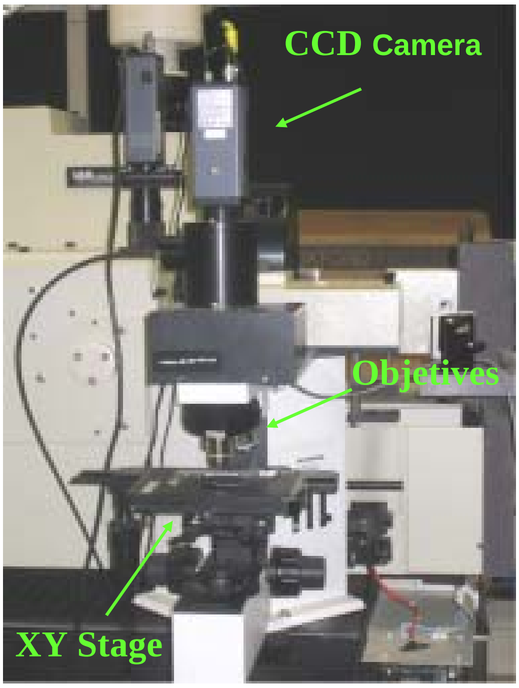

Figure 2.6. Optical microscopy *Olympus* BX40

Two focused laser spot sizes on the sample were used, ~ 1μm (x100 objective) or 10 μm (x10 objective) in diameter depending on the analysis to be performed. The larger spot was used when average measurements were to be performed and compared with x-ray data. The 1-μm spot was used for the local determination of film uniformity. These laser spots produce a power onto the sample surface very low (< 6mW) to avoid heating damage. Table 2.1 shows the nominal laser power (Power$_L$), the corresponding power measured onto the sample surface (Power$_S$) after the losses in the directing and focusing optics and its respective power density for each objective.

Table 2.1

Laser power density onto sample surface

Objective	**Laser Spot (μm)**	**Power$_L$ (mW)**	**Power$_S$ (mW)**	**Power Density (kW/cm^2)**
X10	10	150	6.05 ± 0.02	7.7
		100	4.01 ± 0.02	5.11
X100	1	100	0.65 ± 0.03	82.76
		75	0.41 ± 0.02	52.02

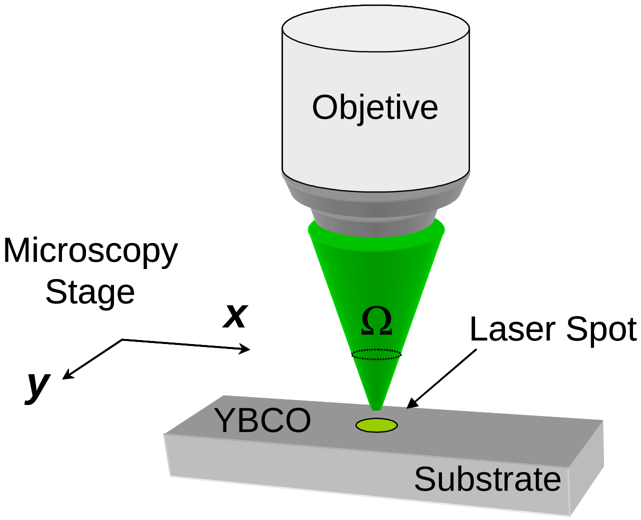

Figure 2.7. Schematic representation of the sample illumination, and collection of the scattered light through the microscope objective in backscattering configuration.

The Raman spectra were collected in backscattering geometry (figure 2.7). The objective used to focus the incident radiation was also used to collect the scattering radiation. The penetration deep of the laser light is determined by the absorption coefficient, α, of the sample. We use the green line (514.5 nm) of the Ar^+ laser, the value of the absorption coefficient is: $\alpha \sim 1.3 \times 10^{+5}$ cm^{-1}[2.2,2.3], and we obtain a probe sample deep of ~ 80 nm.

2.1.4. Raman Spectrometer

The Raman spectrometer is a *Jovin-Yvon* T64000 system. The T64000 system is a fully computerized, triple spectrometer system. The T64000 system has an integrated software and hardware package which combines all functions in a simplified, easy-to-use fashion. The ability to use the T64000 as a single or triple spectrometer permits to optimize the Raman spectrometer to the spectra and sampling requirements. This flexibility is obtained without having to disturb the sample under investigation and is completely automatized.

The T64000 system is equipped with two scanning mechanism, one for pre-monochromator and another for the monochromator (Figure 2.8). Basically, the T64000 is equipped with 1800 gr/mm gratings defining a mechanical range of 0 – 950 nm. Tuning of the gratings is done with sine drive giving an output linear in λ.

All Raman work is carried out using the single spectrometer configuration, for the analysis in a short time (~ 10 min each spectra) with a high detectivity. The detection using the single spectrometer configuration is 3 times more efficient in the spectral range used than the triple system: To be able to work with the single spectrometer configuration the system is equipped with a holographic supernotch filter (SNF), as shown in Figure 2.9. The holographic SNF, described below, is necessary for filtering the elastic scattered light. The monochromator stage is equipped with: a slit (normaly fixed at 120 μm width x 2.5 mm height) for the entrance of the scattered light and a double-gratings *turret*, DGT, (gratings of 1800 gr/mm and 600 gr/mm); the detectivity can again be increased by changing the grating from high (1800 gr/mm) to low (600 gr/mm) dispersion. In our Raman experiments, we used the 1800 gr/mm grating. There are also two mirrors off-axis associated with this grating turret, one to collimate the light coming from the entrance of the spectrometer, and the second one to focus the light from the DGT to the entrance of CCD (figure 2.9).

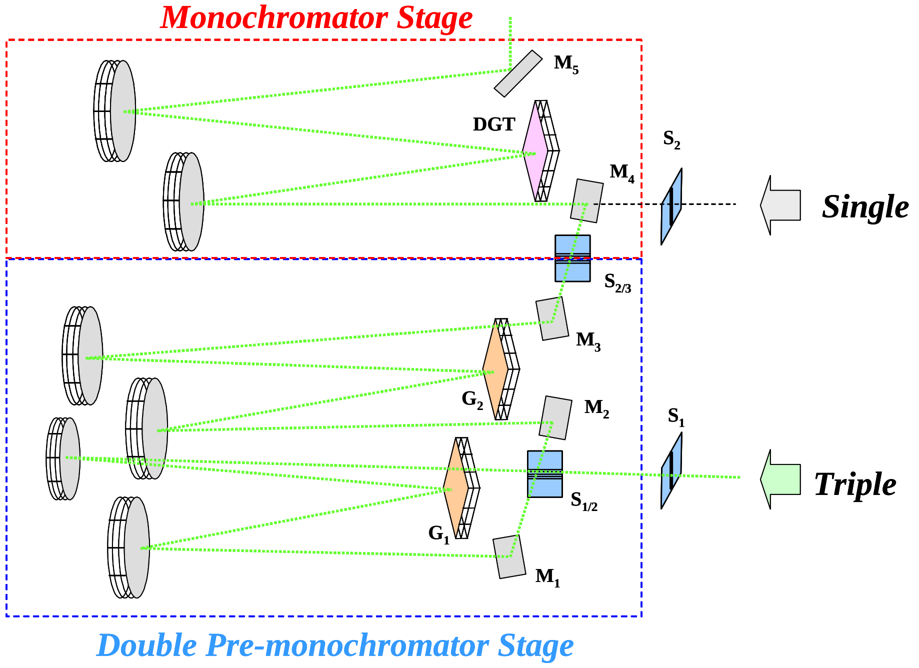

Figure 2.8. Top-view of the basic optical diagram of T64000 system

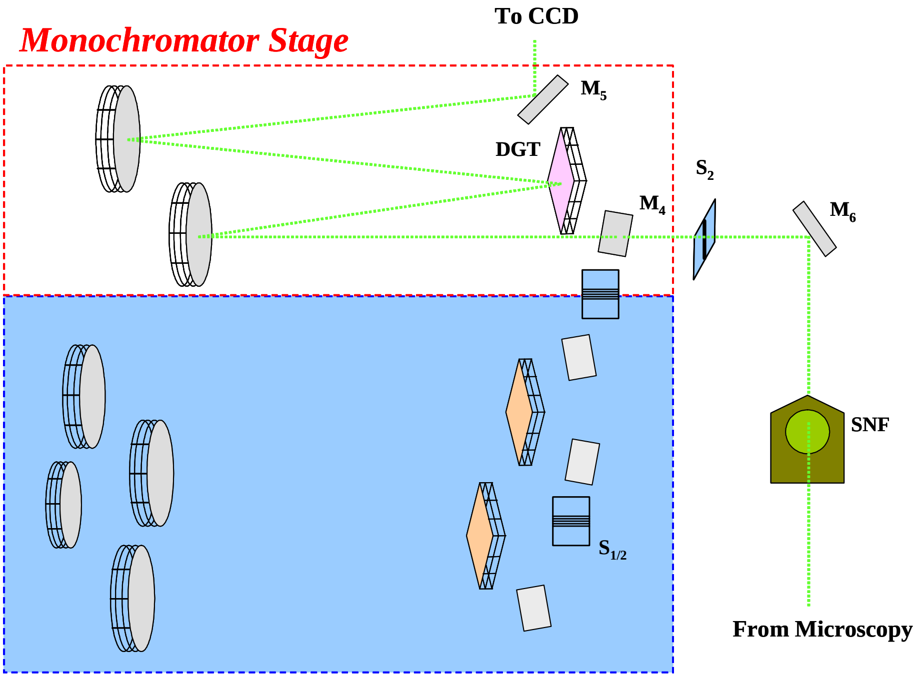

Figure 2.9. Top-view of single spectrometer configuration.

2.1.4.1. Holographic Filter

In the process of light scattering by solids, these produce an elastic (Rayleigh and Brillouin contributions) and an inelastic (Raman contribution) scattering, to filter the elastic scattering part of the Raman spectra, we used a holographic filter called Supernotch (figure 2.10), product of the *Kaiser Optical System Inc*, with serial number HSNF - 25243, optimized for the green line (514.5 nm) of the Ar^+ laser. Specifications of that filter SNF are shown in the table 2.2.

Thus, when we have used a SNF with single spectrometer configuration, the Raman spectra obtained was filtered for frequencies below 150 cm^{-1}. The spectral range used to the characterization of YBCO films was among 200 – 600 cm^{-1}. This spectral range was enough to characterize, analyse and study YBCO films by the phonon Raman modes of O(2,3) and O(4) oxygen atoms.

Table 2.2.

General features of *SuperNotch* Filter

Specifications	**SuperNotch**
Laser Attenuation *Optical Density*	> 4.0
Working Angle	0 – 10 degree
Spectral Bandwidth	< 350 cm^{-1}
Spectral Edgewidth	< 150 cm^{-1}

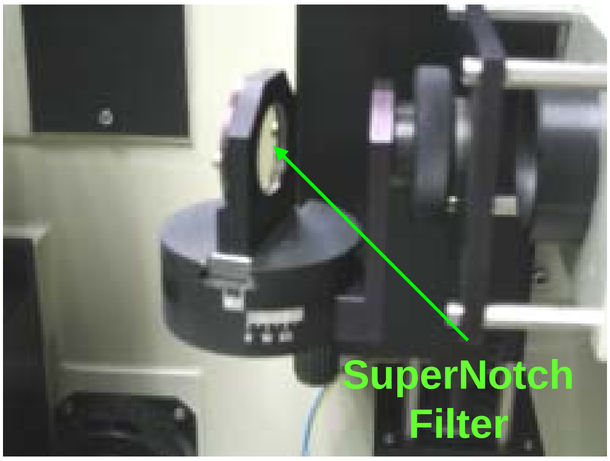

Figure 2.10. Image of SuperNotch filter (SNF) before the entrance to the spectrometer stage.

2.1.4.2. The Scattering Geometries

Two scattering geometries called, *polarized* and *depolarized*, were used to obtain Raman spectra of the YBCO films. To change the scattering geometry a λ/2 plate exists between the two lineal polarizers (at the laser output there is a lineal polarizer to determine the polarization direction of the laser beam incident on the sample and before SNF there is another one). The λ/2 is an optical element known as *retarder*, which serve to change the polarization of an incident wave. Turning the λ/2 plate 45^o degree clockwise we may change the scattering geometry. Figure 2.11 shows the two positions of λ/2 plate to obtain *polarized* and *depolarized* configuration. Spectra are called *polarized* when the directions of $\mathbf{e}_i$ and $\mathbf{e}_s$ are parallel to each other ($\mathbf{e}_i$ and $\mathbf{e}_s$ denote the directions of polarization of the incident and scattered light respectively), as showed in figure 2.12a, it means for example that the incident light propagates along z axis and is polarized along the x axis, and the polarization of the scattered light is analyzed again parallel to x while propagating in the minus z direction; spectra called *depolarized* (Figure 2.12b) when $\mathbf{e}_i$ and $\mathbf{e}_s$ are perpendicular to each other.

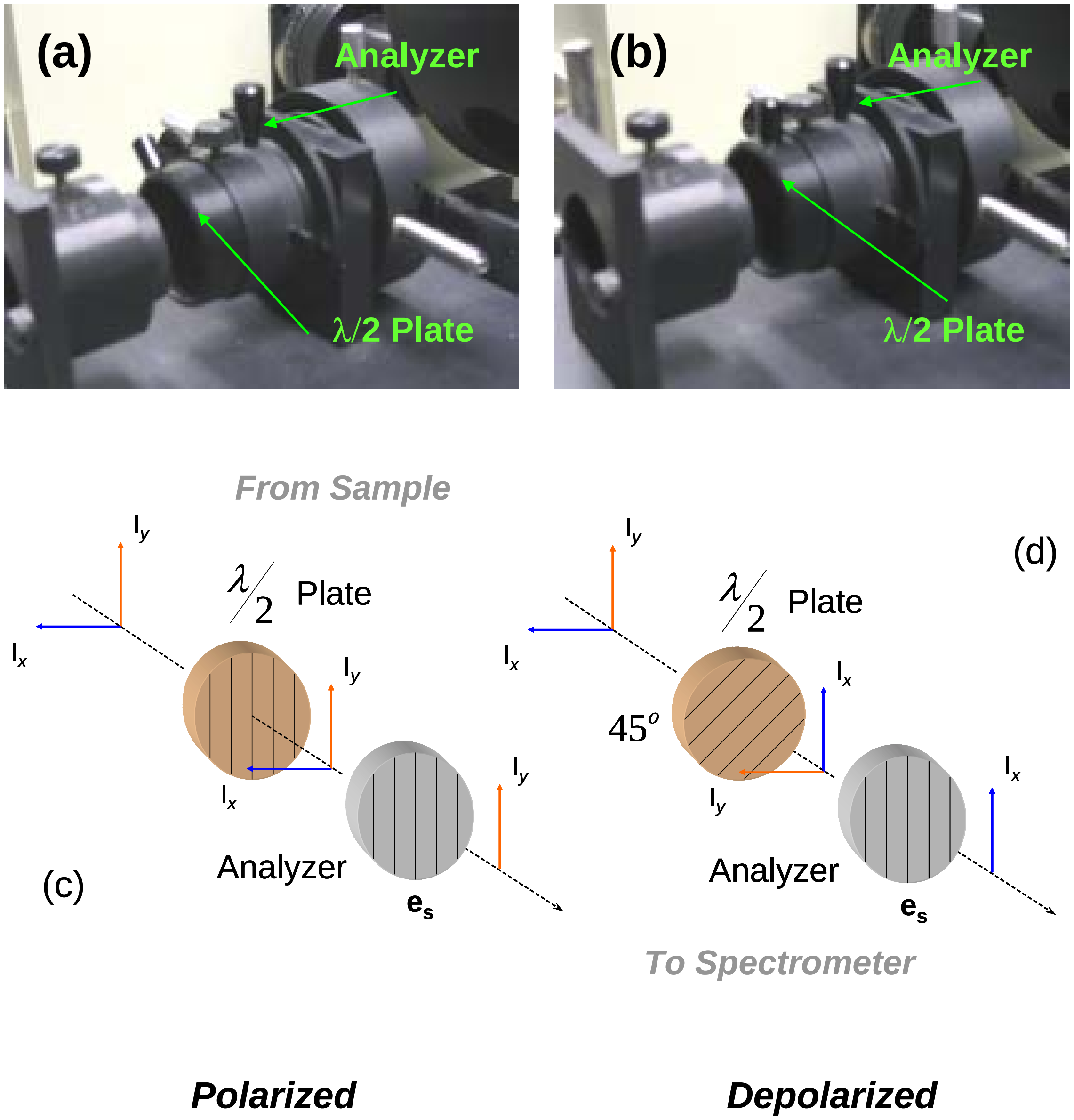

Figure 2.11. Two position of λ/2 sheet to obtain (a) *polarized* and (b) *depolarized* scattering configuration. In (c) the scattered light coming from the sample does not undergoes any change after going through the λ/2 sheet, then the depolarized intensity is cancelled after crossing the analyzer, thus we obtained the *polarized* scattering configuration, but in (d) the incident light coming from sample does undergoes a 90^{o} change after go through the λ/2 sheet turned 45^{o} degree, then the polarized intensity is cancelled after crossing the analyzer, thus we obtained the *depolarized* scattering geometry.

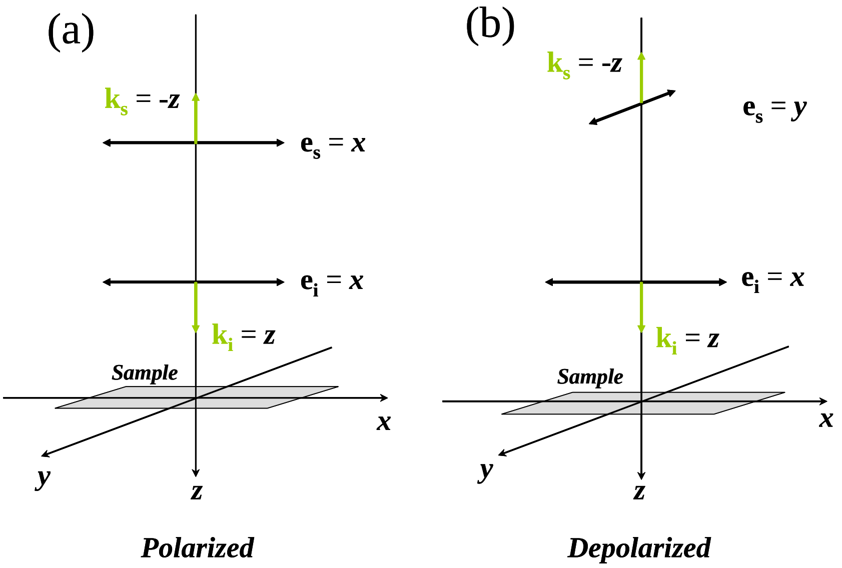

Figure 2.12. Two backscattering geometries: (a) polarized and (b) depolarized.

2.1.4.3. Spectrometer Resolution

To determine the spectrometer instrumental resolution with our standard working conditions (λ_L= 5145 Å) and entrance slit width ~ 120 μm, we use the full width half maximum (FWHM) of the plasma line at 114 cm^{-1} with a value of ~ 2cm^{-1} (Figure 2.13).

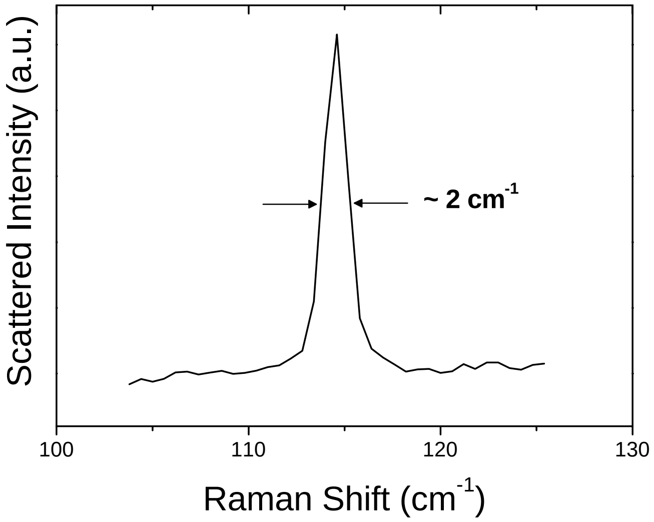

Figure 2.13. Measured plasma line profile.

2.1.5. Detector

The Jovin-Yvon T-64000 Raman spectrometer is equipped with a liquid-nitrogen-cooled charge-coupled device (CCD) detector (Figure 2.14). The components of the detector consist of a detector head, a detector interface unit, a communications card (a Reduced Instruction Set Computer, RISC), and software for hardware control (CCDLOAD.EXE software).

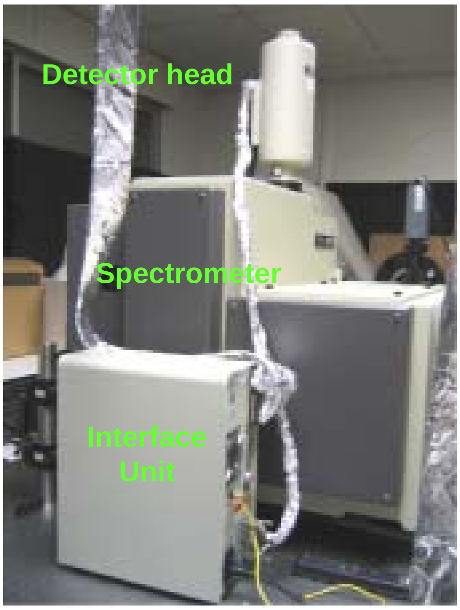

Figure 2.14. Detector head and interface unit

CCD detector arrays are essentially large area silicon photodiodes constructed such that the area is divided into a two dimensional matrix of pixels (1024 x 256 pixels). When illuminated by opening the shutter, each pixel integrates a charge arising from the photoelectric effect. The charges of adjacent pixels are kept separated by a grid of the electrodes that confine the charges by electrostatic force. At the end of the signal integration time the shutter is closed. Then the electrode grid voltages are manipulated by control signals from the detector interface unit. This will sequentially shuttle the pixel charges row by row or column by column to the edge of the chip into a read out register. The signal from the CCD is processed, amplified and converted to digital data points by electronics in the detector interface unit. The data is passed from the detector interface unit to the RISC interface memory. This allows the software running in the host computer to access it rapidly for further processing and display.

The basics features of the CCD are the high quantum efficiency, broad spectral response, large dynamic range, photometric accuracy and linearity. The area of the CCD array of the detector was adjusted to obtain minimum noise and background levels, as well as to interrogate the spectral frequency range between 200 and 700 cm^{-1}.

2.1.5.1. Intensity Correction Factor

To change from *polarized* to *depolarized* scattering geometry we selected different polarization direction of the scattered light using the combination of the λ/2 waveplate and the analyzer. A correction factor K = 1.91 was applied to the spectra measured in polarized configuration, to correct for the efficiency of the collecting optics (laser beam spliter and analyzer) in this configuration.

The correction factor was obtained from the Raman intensity modulations of silicon phonon at 521 cm^{-1} measured onto (*001*) planes of single crystal (figure 2.15). By rotating the single crystal from 0^{o} to 90^{o} degree and measuring the ratio between *polarized* and *depolarized* Raman intensity modulations of this phonon (figure 2.16a) and subsequently fit of these intensity modulations to obtain a corrected Raman intensity modulations (figure 2.16b). Table 2.3 summarized the allowed and non-allowed Raman intensities of silicon phonon mode at 521 cm^{-1} in *polarized* and *depolarized* configuration.

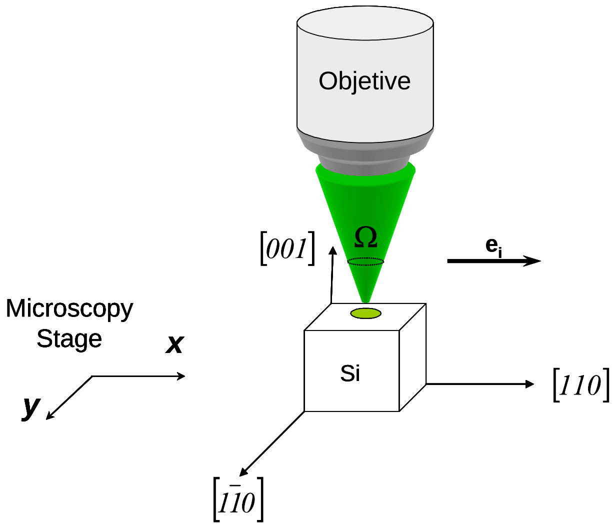

Figure 2.15. Measurement of silicon phonon at 521 cm^{-1} onto (001) planes of single crystal. Notice the $\mathbf{e}_i$ direction of incident light was parallel to $\left[110\right]$ direction; the $\left[110\right]$ and $\left[1\bar{1}0\right]$ directions were parallel to x and y directions of microscope stage, respectively.

Table 2.3

Allowed or non-allowed Raman intensities on Silicon single crystal for scattering in a (001) face

Silicon Phonon	$I^{[110]}_{polarized}$	$I^{[1\bar{1}0]}_{polarized}$	$I^{[100]}_{depolarized}$, $I^{[010]}_{depolarized}$
521 cm^{-1}	*allowed*	*allowed*	*non-allowed*

where $I^{[110]}_{polarized}$ and $I^{[1\bar{1}0]}_{polarized}$ are the *polarized* Raman intensities with the $\mathbf{e}_i$ direction of incident light parallel to $\left[110\right]$ and $\left[1\bar{1}0\right]$ directions, respectively; while $I^{[100]}_{depolarized}$ and $I^{[010]}_{depolarized}$ are the *depolarized* Raman intensities with the $\mathbf{e}_i$ direction of incident light parallel to $\left[100\right]$ and $\left[010\right]$ directions, respectively

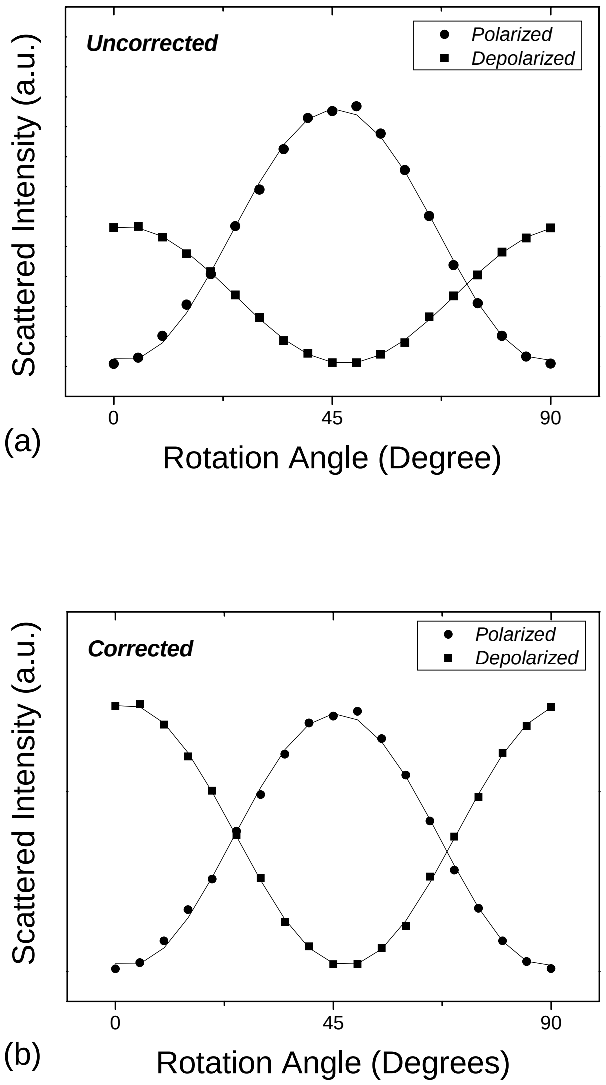

Figure 2.16. (a) Uncorrected and (b) corrected experimental Raman intensity modulations of silicon phonon at 521 cm^{-1}, with correction factor K = 1.91.

2.1.6. Software and Hardware Control

Briefly, the *Jobin Yvon* T64000 Raman spectrometer is supplied with a software package *SpectraMax* v1.1[2.4] to operate the spectrometer and to perform a range of operations on the acquired data (figure 2.17).

The laser parameters are controlled by hand (switch on, λ tuning and power), which leads to the monochromator and detector parameters to be considered. The computer controls the most crucial monochromator parameter, the slit width $S_{1/2}$ and $S_{2/3}$, opening and closing of the slits being achieved by means of stepper motors, and the two gratings at the double pre-monochromator stage, as well as the turret at monochromator stage; those gratings are controlled by stepper motors too.

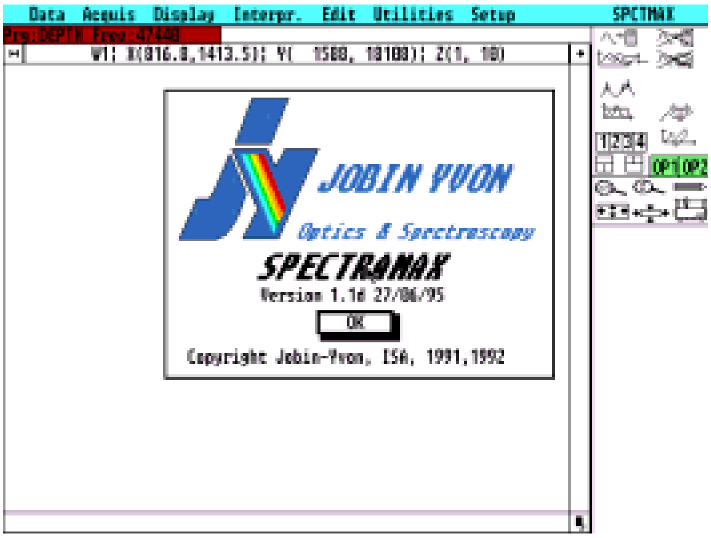

Pre:DEPTH Free:47440

W1; X(816.0,1413.5); Y(1500, 10100); Z(1, 10)

Version 1.1d 27/06/95

Copyright Jobin-Yvon, ISA, 1991,1992

Figure 2.17. Software *Spectramax* for data acquisition.

2.2. Instrumentation for X-Ray Diffraction

X-ray diffraction (XRD) is a versatile technique used for identifying the crystalline phases present in films and tapes, and analyze structural properties such as stress, grain size, phase composition, crystal orientation, and defects of different phases. Three types of measurements were made with XRD: $\theta/2\theta$-scan, ω-scan and ϕ-scan. A scheme of theses three angles are illustrated in figure 2.18. The $\theta/2\theta$- and ω-scan XRD were made by using a Rigaku Rotaflex RU-200BV diffractometer with Cu-K_α $\lambda = 1.5418$ Å and a D2000 Siemens diffractometer with Cu-K_α $\lambda = 1.5418$ Å in the x-ray diffraction service at ICMAB, while the ϕ-scan XRD was made by using a four circle diffractometer Philips PW 3710 MPD Control diffractometer with Cu-K_α $\lambda = 1.5418$ Å at *Serveis Cientifico-Tècnics* of the Universitat de Barcelona (UB).

A $\theta/2\theta$-scan XRD, in Bragg-Bretano geometry[2.5], uses a beam of X-rays bombarding a specimen from various angles, θ. The X-rays are diffracted (according to Bragg's law:

$2d\sin\theta = n\lambda$) as they are reflected from successive planes formed by the crystal lattice of the material. By varying the angle of incidence, a diffraction pattern emerges that is characteristic of the sample. The pattern is identified by comparing it with an internationally recognized data base powder diffraction file (PDF) reference patterns. In YBCO epitaxial films with the grains aligned in preferred orientation along (00*l*) lattice planes, the intensity relationship described inside of the PDF files are not valid, because they change according to the degree orientation of the grains respect to substrate surface. For example, the presence of (*103*) YBCO reflection denotes grains aligned randomly respect to substrate surface (non textured film), while (*00l*) reflections denote YBCO grains aligned with *c*-axis perpendicular to substrate surface (textured film) and (*h00*) reflections denote YBCO grains aligned with *a*-axis perpendicular to substrate surface.

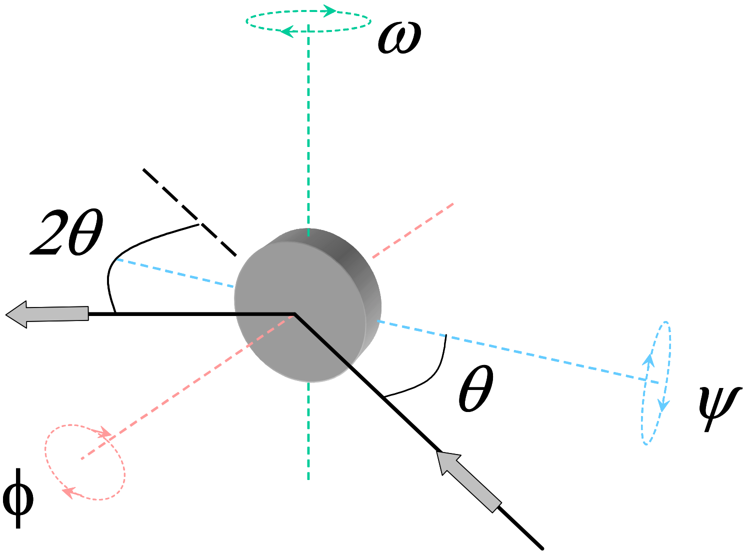

Figure 2.18. Scheme of θ, ϕ, ω and Ψ angles in XRD.

On the other hand, the ω-scan XRD measurements (*rocking curve*) characterize the *out-of plane* texture of YBCO films. It measures a single Bragg peak, for example the (*005*) YBCO profile ($2\theta \sim 35^o$), as the sample is tilted, ω degree (figure 2.18), within the diffraction plane. Determining the FWHM value of the profile, Δω, we obtained information about the degree of the uniaxial epitaxy.

Finally, the *pole figure* and ϕ-scan XRD measurements characterize the *in-plane* texture of YBCO films. Figure 2.19 illustrates two cases of *in-plane* texture. For ϕ-scan XRD measurement, we have used the (*102*) YBCO reflection (for fixed 2θ and Ψ degree). The ϕ-scan XRD is a high-accuracy "*slice*" of the *pole figure*, and the FWHM value provides the dregree of *in-plane* texture.

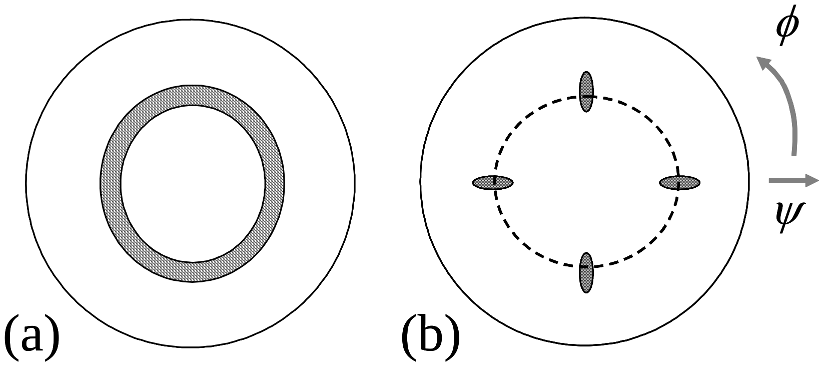

Figure 2.19. Poles figures of YBCO films with (a) random and (b) biaxial texture. Notice the ϕ-scan is a high-accuracy "*slice*" of *pole figures*.

2.3. Instrumentation for Scanning Electron Microscopy

Because of its versatility and the wide range of information it can provide, the scanning electron microscopy (SEM) is often the preferred starting tool for analytical microscopy. With SEM, a focused beam of high-energy electrons is scanned over the surface of the material. A basis scheme of SEM is shown in figure 2.20. The electron beam interacts with the material, causing a variety of signals: secondary electrons, backscattered electrons, hve been used to characterize our material. The SEM images were made by using a JEOL JSM-6300 SEM in the *Servei de Microscòpia Electrònica* at UAB, providing remarkable analytical versatility and a wide magnification range: from 15x to 300,000x. Attached to JEOL SEM there is an energy-dispersive X-ray diffraction (EDX) from LINK ISIS-200 of the Oxford Instruments company. A PC interface allows the instrument to be easily operated.

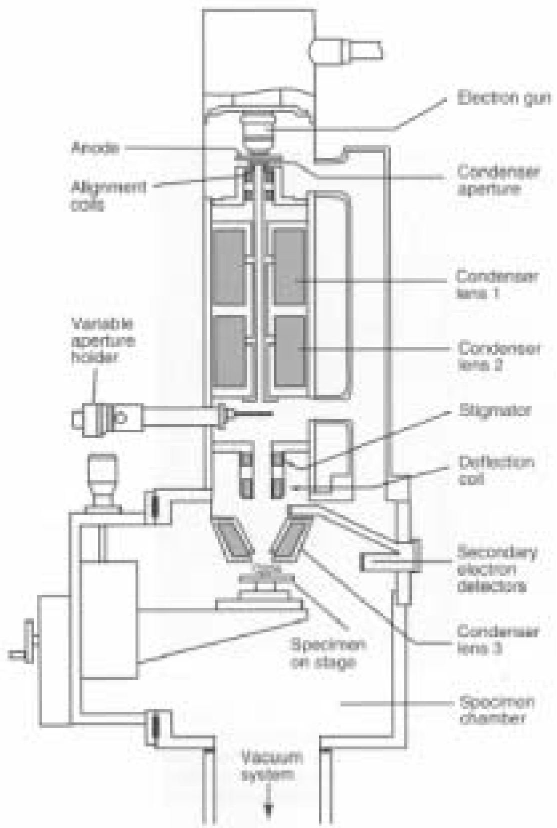

Figure 2.20. Schematic diagram of typical Scanning Electron Microscope (SEM).

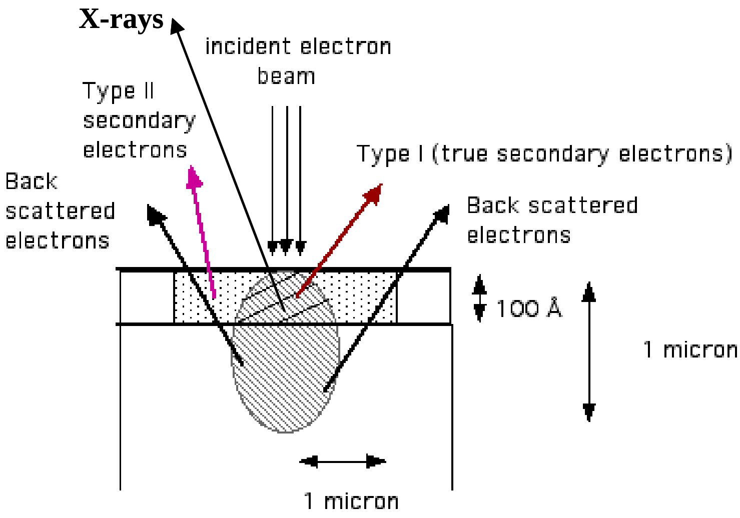

Figure 2.21. Electrons incident on a material may scatter back and knock out other (secondary) electrons. The penetration depth is in the order of microns.

No sample preparation is required in our case, since the YBCO films once oxygenated are conducting so the films were just placed in the specimen stage of the SEM. If they were not conducting, it is necessary to coat them with a thin conductive layer such as gold.

By SEM observations of the film surface, the grain morphology may be observed as well as (*c*-axis grains versus *a*/*b* crystals) the grain orientation, film homogeneity, secondary phases and porosity. This technique is complementary to the information acquired by XRD. With EDX it may be possible to analyze semi-quantitatively the film stoichiometry and secondary phases (figure 2.21).

2.4. Instrumentation for Transmission Electron Microscopy

With transmission electron microscopy (TEM), a thin (<200 nm) sample is bombarded by a highly focused beam of single-energy electrons. The beam has enough energy for the electrons to be transmitted through the sample (figure 2.22). The samples are YBCO thin foils prepared by the conventional cutting, gluing and grinding procedures, followed by a final milling step with Ar ions down to perforation[2.6]. The transmitted electron signal is greatly magnified by a series of electromagnetic lenses up to atomic resolution. The magnified transmitted signal may be observed in two ways, through electron diffraction or direct electron imaging. Electron diffraction patterns were used to determine the crystallographic structure of YBCO precursor phases in the formation process of YBCO phase. Direct electron images yield information about the microstructure of the precursor phases, YBCO grain orientation and size.

The TEM images and electron diffraction patterns were made by using a Philips CM30 TEM (transversal cross section) while HRTEM images patterns were made by using a JEOL 1010 electron microscopes operated at 200 kV (point to point resolution 0.19 nm) equipped with a Gatan Image Filter 2000 EELS spectrometer with an energy resolution of 0.8 eV in the *Serveis Cientifico-Tècnics* at UB. The EELS spectrometer allowed us perform quantitative element analysis of the YBCO films.

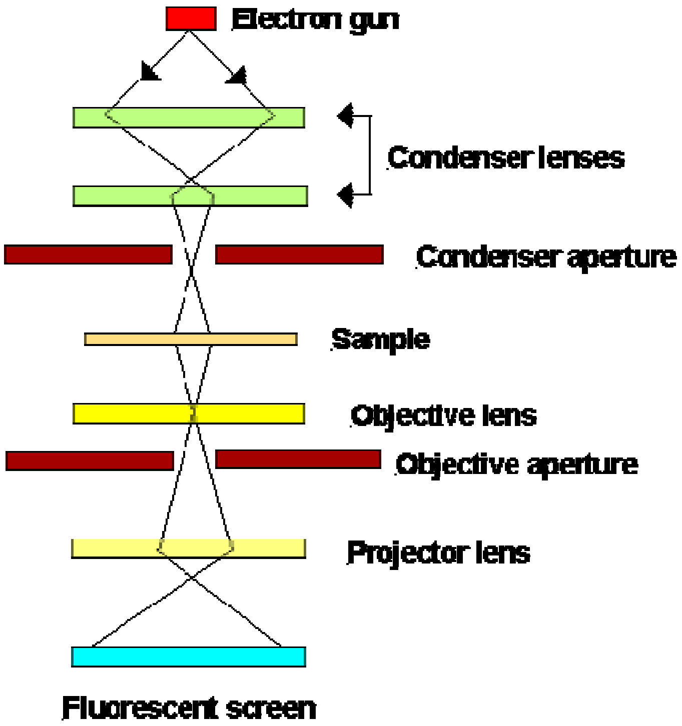

Figure 2.22. Schematic diagram of typical Transmission Electron Microscopy (TEM).

2.5. Instrumentation for Resistivity

Resistivity measurements of YBCO TFA-MOD films were done by the four point *Van der Pauw* method[2.7]. The YBCO films were mounted into the sample holder and no silver contacts were used, instead of this we utilized four spring kneedles. Briefly, a 224 programmable current source generates the excitation current (100 μA) and the 181 nanovoltimeter, both devices from *Keithley* company, is used to measure the voltage developed across the sample while the temperature controller, from *Lakeshore* company, reads the temperature for each value of voltage. Dynamic resistivity measurements were performed by lifting the sample holder close to liquid nitrogen (LN_2) surface. Figure 2.23 shows a scheme of the measurement of resistivity. The actual data acquisition is event based and labview interface fully automatized is used to carry out the full measurement. A clock runs at a fixed rate and at every clock event, a set current is applied to the sample and the voltage developed read.

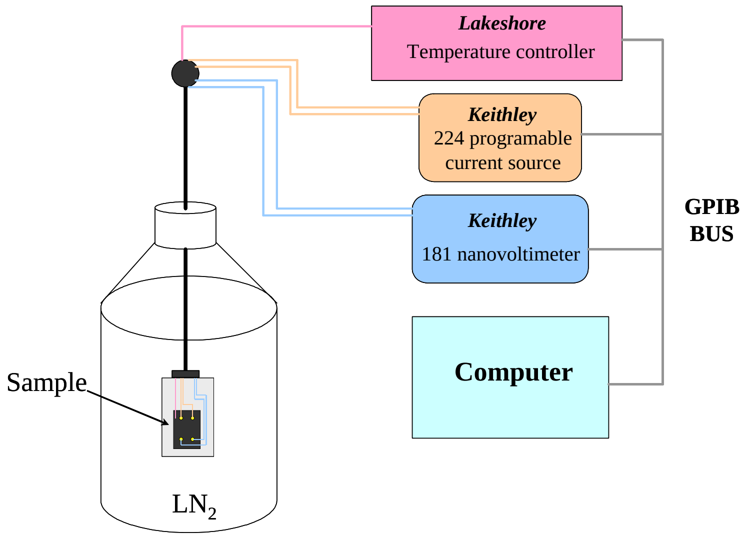

Figure 2.23. Schematic diagram for resistivity measurements in YBCO TFA films.

2.6. SQUID Magnetometer

The critical current densities of YBCO films were determined by using a superconducting quantum interference device (SQUID) magnetometer of the *Quantum Design* Company, with a superconducting coil able to generate up to 5.5 T. The system consists of a superconducting coil, with a SQUID detection system (schematic diagram in figure 2.24). The superconducting coil creates certain *dc* magnetic field applied to the sample inside the coil. The detection system is composed of sensor coils set placed in the centre of the superconducting coils. During the measurement, the sample is moved inside the coils set, in such a way that a current is induced on the coils set proportional to magnetic flux change. The signal is amplified by a SQUID sensor, a current-voltage transducer so it achieves a very high sensitivity. The voltage variations that may be detected by SQUID are proportional to magnetic moment of the sample (nominal sensitivity in these equipments is in the order of 10^{-7} emu). All the system is placed inside of helium cryostat so that the temperature may vary between 5K and 300K. To ensure enough homogeneity of magnetic field during the sample displacement inside the coils set, we have used displacements in the order of 3 cm.

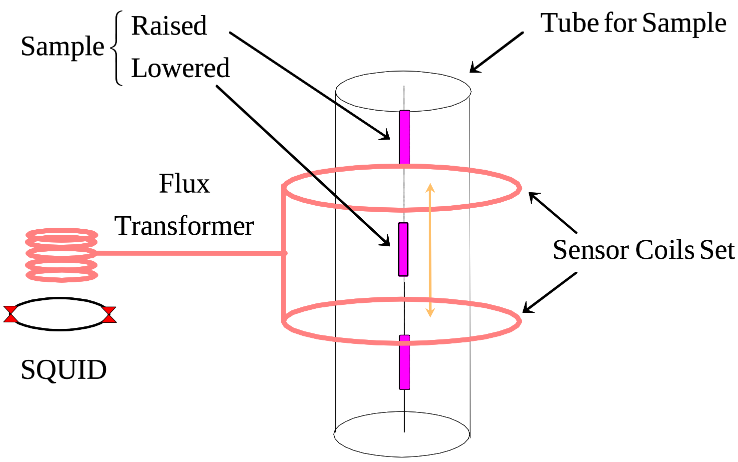

Figure 2.24. The change of magnetic flux in the sensor coil loop that has been produced by raising or lowering a sample induces a current which is transferred to a multiloop coil where it is measured by a SQUID.

The inductive critical current density is then determined by measuring **M**(H) curves at different temperatures and **M**(T) curve at self-field with the SQUID magnetometer. The critical current density is calculated from the irreversible magnetization hysteresis loop by using the critical state *Beam* model equation[2.8]:

$$J_c^{ab} = \frac{3\Delta \mathbf{M}}{2R} \tag{2.1}$$

Chapter 3

Texture analysis of YBCO films by micro-Raman

A quantitative determination of the degree of uniaxial and biaxial texture of YBCO CC has been carried out by micro-Raman spectroscopy. The uniaxial texture is characterized by determining the *c*-axis grain fraction from the ratio between the intensity of O(2,3)-B_{1g} and O(4)-A_g modes. The degree of *in-plane* orientation is determined from the relative intensity modulation of the Raman phonon modes when samples are rotated around the axis perpendicular to the films. The biaxial texture parameter determined from Raman scattering has been modeled taking into account different grain misorientation distribution functions. The Raman results are compared with results of XRD ϕ-scans measurements, and we demonstrate the relationship between the texture determinations provided by both techniques. Additionally, the possibility of micro-Raman spectroscopy to perform local analysis allows characterizing the texture uniformity of the superconducting films. The relationship between the biaxial texture determined by micro-Raman and the critical currents of coated conductors is further evidenced.

3.1. Determination of uniaxial texture in YBCO films

The potentiality of micro-Raman spectroscopy to determine the orientation of the crystal axes in YBCO films was first evidenced by Farrow *et al*[3.1]. The distinct selection rules for Raman scattering from the optical phonons of YBCO single crystals enable to determine the *c*-axis grain fraction in those films[3.2,3.3]. Two phonon peaks in the Raman spectrum previously described in chapter 1 have been used in the structural characterization of YBCO films. The peak at 340 cm^{-1}, B_{1g}-like mode, associated with the *out-of-phase* vibration of the O(2,3) oxygen atoms in the CuO_2 superconducting planes, and the peak at 500 cm^{-1}, an A_g mode involving the apical oxygen atoms O(4) vibrations[3.4,3.5].

We have first determined the *c*-axis grain fraction oriented perpendicular to the substrate plane (figure 3.1). To determine the uniaxial texture of YBCO films and CC, we have applied the same principles reported in reference [3.6] and specifically (as explained in the section 3.1.2) we have determined the local uniaxial texture to estimate the size and distribution of the *a*-axis and *c*-axis oriented grains. A preliminary study determining the local degree of *c*-axis grain texture in YBCO IBAD coated conductors was presented in reference [3.7].

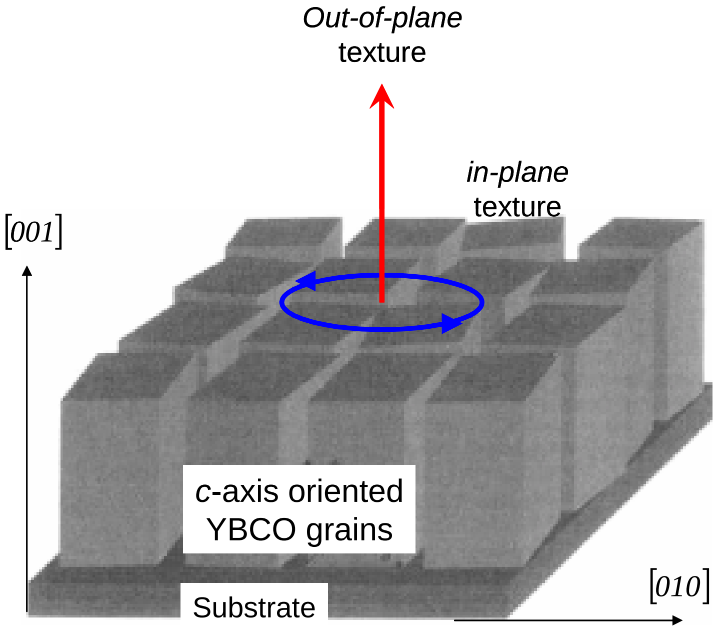

Figure 3.1. Scheme of the *out-of-plane* and *in-plane* texture in a YBCO film with large *c*-axis oriented grains perpendicular to substrate surface. Information about the *out-of-plane* and *in-plane* texture can be obtained by micro-Raman measurements.

In the nearly tetragonal symmetry, the Raman tensors $\mathbf{R}_{B_{1g}}$ and $\mathbf{R}_{A_g}$ corresponding to the O(2,3)- and O(4)-modes, respectively, have the forms shown in table 3.1.

Table 3.1.

Raman tensors corresponding to the O(2,3)-B_{1g} and O(4)-A_g phonon modes.

$$\mathbf{R}_{B_{1g}} = \begin{pmatrix} x_{B_{1g}} & & \\ & -x_{B_{1g}} & \\ & & 0 \end{pmatrix}$$

$$\mathbf{R}_{A_g} = \begin{pmatrix} x_{A_g} & & \\ & y_{A_g} & \\ & & z_{A_g} \end{pmatrix}$$

For our calculations we have used the values of the Raman tensor elements taken from Ref [3.6], and they are: $x_{A_g}^2 = y_{A_g}^2$ =2**,** $z_{A_g}^2$ =100, $x_{B_{1g}}^2 = y_{B_{1g}}^2$ =8.5. The relative Raman tensor values are normalized to the $z_{A_g}^2$ component. Those values were obtained from measurements on YBCO single crystals.

As described in chapter 1, the intensity of the Raman bands strongly depends on the crystal orientation and polarization geometry of the experimental setup, and can be expressed as:

$$I_R \approx \left| \mathrm{e}_s \cdot \overleftrightarrow{\mathrm{R}} \cdot \mathrm{e}_i \right|^2 \qquad (1.12)$$

Were $\mathbf{e}_i$ and $\mathbf{e}_s$ denote the electric vector of the incident and scattered light, respectively, while **R** represents the Raman scattering tensor of the particular Raman band under consideration. Table 3.2 shows the calculated relative Raman intensities of the O(2,3) and the O(4) YBCO modes in different backscattering configurations on the *c*-face and on the *a*-face of an YBCO crystal according to the schematic arrangement displayed in figure 3.2(a) and 3.2(b) respectively . We use the Porto notation $z(x,x)\bar{z}$ in order to describe the polarization geometry. Here the first and the last letter represent the direction of the incoming and scattered photons, whereas the letters in brackets indicate the incoming and scattered polarization

Table 3.2

Relative Raman intensities of the O(2,3) and O(4) phonon modes for different backscattering configurations on the *c*-face and the *a*-face of an YBCO crystal (see figure 3.2)

c-face	Backscattering configuration	B_{1g}-mode	A_{1g}-mode
	$z(x,x)\bar{z}$	8.5	2
	$z(y,y)\bar{z}$		
	$z(y,x)\bar{z}$	0	0
	$z(x,y)\bar{z}$		
	$z(x',x')\bar{z}$	0	0
	$z(y',y')\bar{z}$		
	$z(x',y')\bar{z}$	8.5	2
	$z(y',x')\bar{z}$		
***a*-face**	$x(z,z)\bar{x}$	0	100
	$x(y,y)\bar{x}$	8.5	2
	$x(y,z)\bar{x}$	0	0
	$x(z,y)\bar{x}$		
	$x(y'',y'')\bar{x}$	$\frac{1}{4}(8.5)$	$\frac{1}{4}(\sqrt{2}+10)^2$
	$x(z'',z'')\bar{x}$		
	$x(y'',z'')\bar{x}$	$\frac{1}{4}(8.5)$	$\frac{1}{4}(\sqrt{2}-10)^2$
	$x(z'',y'')\bar{x}$		
$x'=\frac{1}{\sqrt{2}}(110)$	$y'=\frac{1}{\sqrt{2}}(1\bar{1}0)$	$y''=\frac{1}{\sqrt{2}}(011)$	$z''=\frac{1}{\sqrt{2}}(0\bar{1}1)$

The orientation of YBCO films grown on single-crystal or textured oxide substrates can be controlled through deposition conditions. In principle, grains with their *c*-axis perpendicular parallel to the plain of the substrate are possible. We will refer to them as *c*-axis and *a*-axis oriented grains respectively (see figure 3.3). This two configurations were used for the determination of the uniaxial texture.

In *c*-axis oriented films, the crystals *c*-axis are perpendicular to the substrate surface, and both *a*-axis and *b*-axis lie in the substrate surface plane. According to table 3.2, a highly *c*-axis oriented film should show a strong B_{1g} mode at 340 cm^{-1} for a backscattering Raman measurement. On the contrary, a highly *a*-axis oriented film will display a larger intensity of the A_g mode at 500 cm^{-1} compared to the intensity of the B_{1g} mode. This fact will allow us to measure the c-axis growth fraction of YBCO films.

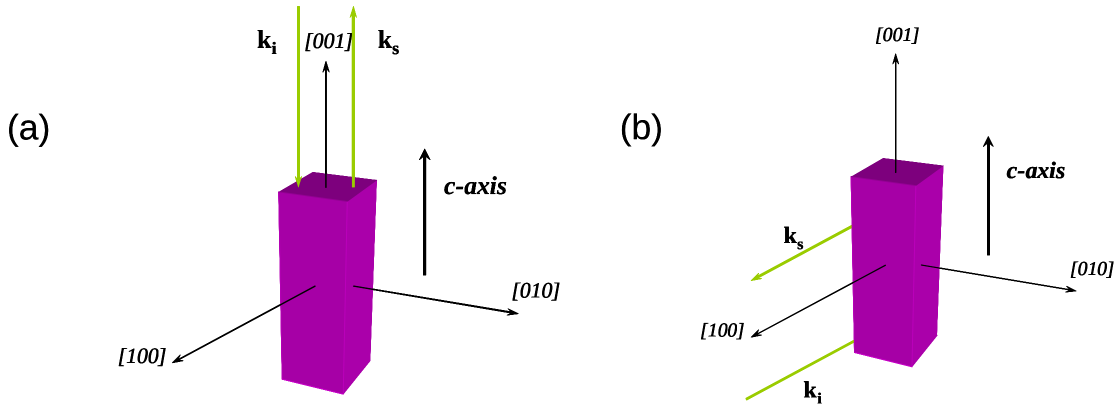

Figure 3.2. Schematic arrangement showing the two scattering configurations for backscattering on (a) the *c*-axis face and (b) on the *a*-face of an YBCO crystal.

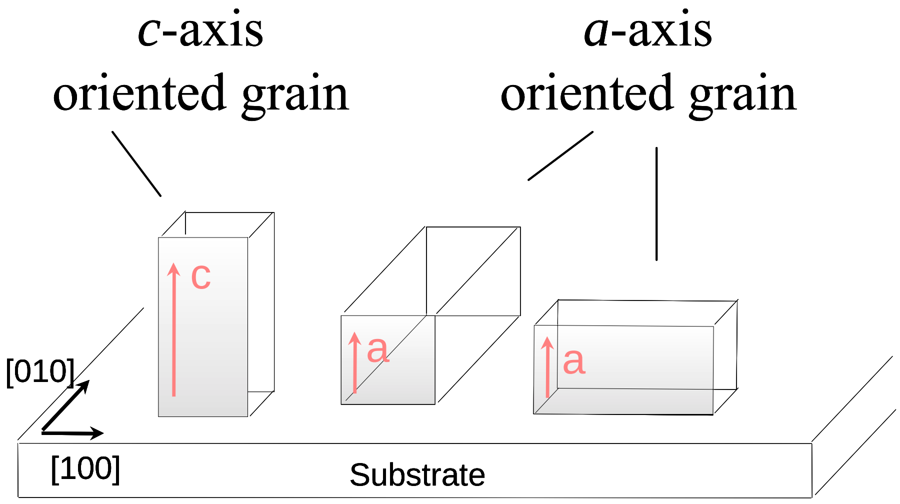

Figure 3.3. Scheme of *c*-axis and *a*-axis oriented YBCO crystals on (*001*) substrate.

For instance, figure 3.4 shows typical Raman spectra of two different YBCO IBAD CC with *polarized* and *depolarized* scattering geometries. In this experiment, the electric field **e**$_i$ of the laser beam is polarized along the [*100*] direction of the substrate. The polarization direction of the scattered field is either parallel (*polarized*) or perpendicular (*depolarized*) to **e**$_i$. Figure 3.4a shows the typical Raman spectra of a sample with a large fraction of *c*-axis oriented grains. The Raman spectra of these samples is characterized by a strong O(2,3)-B_{1g} mode and a weak O(4)-A_g phonon mode. On the contrary, the strong intensity of the O(4)-A_g phonon compared to the O(2,3) mode of figure 3.4b is an indication of a film with a large fraction of *a*-axis oriented grains. Therefore, the ratio between $I_{B_{1g}}$ and I_{A_g} intensities is strongly related to the fraction of *c*-axis oriented grain.

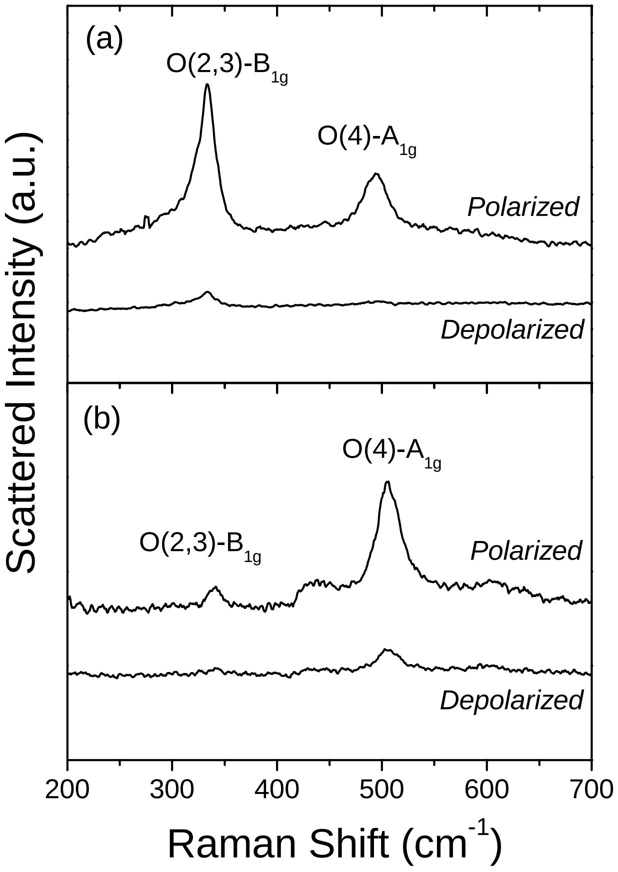

Figure 3.4. *Polarized* and *depolarized* Raman spectra for two YBCO IBAD CC with different fraction of *c*-axis oriented grains. (a) *c*-axis oriented film, (b) *a*-axis oriented film. Incident polarization parallel to the sample substrate.

3.1.1. The Delta Parameter

In order to quantify the *c*-axis and *a*-axis oriented grains fraction in a YBCO film, the intensity of the Raman signal is the sum of the intensity I_c of the *c*-axis oriented part and I_a of the *a*-axis oriented part of the film[3.6],

$$I_R = \delta . I_c + (1-\delta) I_a \tag{3.1}$$

We defined the parameter, δ, as the *c*-axis oriented grain fraction or uniaxial texture of the YBCO film. According to equation (3.1), the values of δ parameter are between 1 and 0, *i.e.*, δ is close to unity for *c*-axis oriented films and close to zero for *a*-axis oriented films.

The uniaxial texture, δ, can be then calculated from the Raman intensity ratio between O(2,3)-B_{1g} and O(4)-A_g modes, *i.e.*,

$$r = \frac{I_{B_{1g}}}{I_{A_g}} . \tag{3.2}$$

In equation (3.2), the total intensity, for each mode, is the sum of the integrated intensities (section 3.1.2) in the *polarized* and *depolarized* spectra, *i.e.*,

$$r = \frac{I_{B_{1g}}}{I_{A_g}} = \frac{I_{B_{1g}}^{pol} + I_{B_{1g}}^{despol}}{I_{A_g}^{pol} + I_{A_g}^{despol}} \tag{3.3a}$$

Considering the contribution of *c*-and *a*-axis oriented grains to the *polarized* and *depolarized* Raman signal, we have

$$r = \frac{\delta . I_{c_{B_{1g}}}^{pol} + (1-\delta) I_{a_{B_{1g}}}^{pol} + \delta . I_{c_{B_{1g}}}^{despol} + (1-\delta) I_{a_{B_{1g}}}^{despol}}{\delta . I_{c_{A_g}}^{pol} + (1-\delta) I_{a_{A_g}}^{pol} + \delta . I_{c_{A_g}}^{despol} + (1-\delta) I_{a_{A_g}}^{despol}} \tag{3.3b}$$

Applying the contraction of their respective Raman tensors (table 1.7):

$$r = \frac{\delta.(x_{B_{1g}}^2 + y_{B_{1g}}^2) + (1-\delta).(x_{B_{1g}}^2 + z_{B_{1g}}^2)}{\delta.(x_{A_g}^2 + y_{A_g}^2) + (1-\delta).(x_{A_g}^2 + z_{A_g}^2)} \qquad (3.3c)$$

From table 1.7, the Raman tensor elements $x_{A_g}^2 = y_{A_g}^2$, $z_{B_{1g}}^2 \approx 0$ and $x_{B_{1g}}^2 = y_{B_{1g}}^2$, and therefore equation (3.3c) may be re-writing,

$$r = \frac{\delta.x_{B_{1g}}^2 + (1-\delta)\frac{1}{2}(x_{B_{1g}}^2)}{\delta.x_{A_g}^2 + (1-\delta)\frac{1}{2}(x_{A_g}^2 + z_{A_g}^2)} \qquad (3.4)$$

Considering the Raman tensor component values displayed in table 3.1, we can calculate the relationship existeng between r and δ. Figure 3.5 shows the behavior of the *r* parameter for that model of *c*- and *a*-axis oriented grains. The *r* values are in the range of 0.083 and 4.25, for a perfectly *a*-axis oriented and a perfectly *c*-axis oriented film respectively, *i.e.*, the intensity of O(2,3)-B_{1g} mode for a large fraction of *c*-axis grains is 4.25 times the intensity of O(4)-A_g mode. On the other hand, for a large fraction of *a*-axis grain, the intensity of O(4)-A_g mode is 12 times the intensity of O(2,3)-B_{1g} mode. This fact can be clearly observed in figure 3.4, where an *c*-axis oriented film clearly displays a larger O(2,3)-B_{1g} Raman signal while in an *a*-axis oriented film we observe a larger O(4)-A_g Raman signal.

From a simple transformation of equation (3.4), the uniaxial texture can be expressed by the following equation:

$$\delta = \frac{r.(z_{A_g}^2 + x_{A_g}^2) - x_{B_{1g}}^2}{r.(z_{A_g}^2 - x_{A_g}^2) + x_{B_{1g}}^2} \qquad (3.5a)$$

$$\delta = \frac{r.(102) - 8.5}{r.(98) + 8.5} \qquad (3.5b)$$

From the very simple equation (3.5b), micro-Raman spectroscopy enables an easy method to determine the uniaxial texture of YBCO films by only determining the ratio of the intensities of O(2,3)-B_{1g} and O(4)-A_g modes. For instance, the δ values extracted from the Raman measurements for the two samples displayed in figures 3.4a and 3.4b are $\delta = 0.92 \pm 0.05$ and $\delta = 0.03 \pm 0.05$, respectively.

Although this simple model does not include any distribution of grain tilting with respect to perfect *on-axis* orientation identified in XRD as the FWHM of the ω-scan (Δω).We have estimated an error value in the *c*-axis oriented YBCO grains (δ-parameter) determination below 3% for neglecting the grain tilt for samples with $\Delta\omega < 5°$.

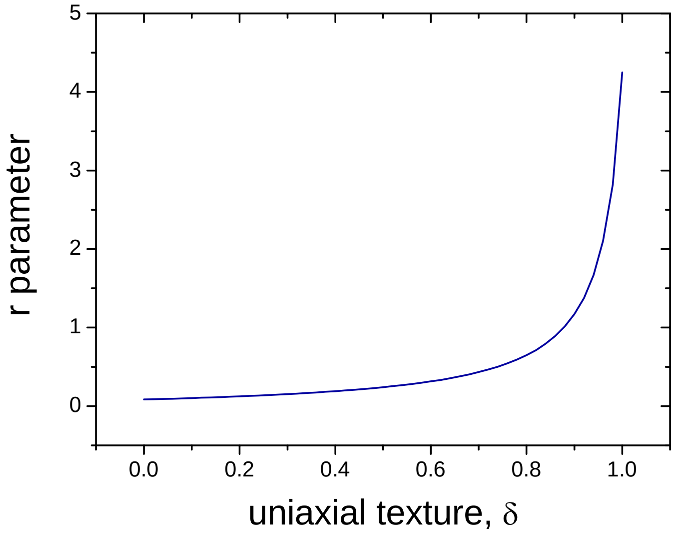

Figure 3.5. Ratio between the intensity of O(2,3) and O(4) mode for different values of uniaxial texture.

3.1.1.1. Fitting of micro-Raman Spectra

In order to determine the intensity ratio (equation 3.2), it is very important to take adequate profiles to integrate the area of the phonon lineshape. We determine the integrated intensities by fitting the YBCO phonon spectrum with two kind of profiles:

1.- ***Fano* lineshape** (asymmetric lineshape): Fano profile[3.8] was used for O(2,3)-B_{1g} phonon mode for *polarized* and *depolarized* spectra. Figure 3.6 shows that the line shape of O(2,3)-B_{1g} phonon mode is not a symmetric Lorentzian profile, due to its coupling with the electronic background, created by the charge transfer to the CuO_2 superconducting planes. This electron-phonon coupling results in a typical Fano profile:

$$I_{B_{1g}} = I_o \frac{\left[\frac{(\omega - \omega_o)^2}{\gamma} + q \right]}{\left[1 + \frac{(\omega - \omega_o)^2}{\gamma^2} \right]} + Const \tag{3.6}$$

where ω_o is the phonon frequency of O(2,3)-B_{1g} mode, γ is the FWHM of the bare phonon, q is an adimensional parameter ($1/q$ is called the Fano parameter) affecting the lineshape plus a constant background term.

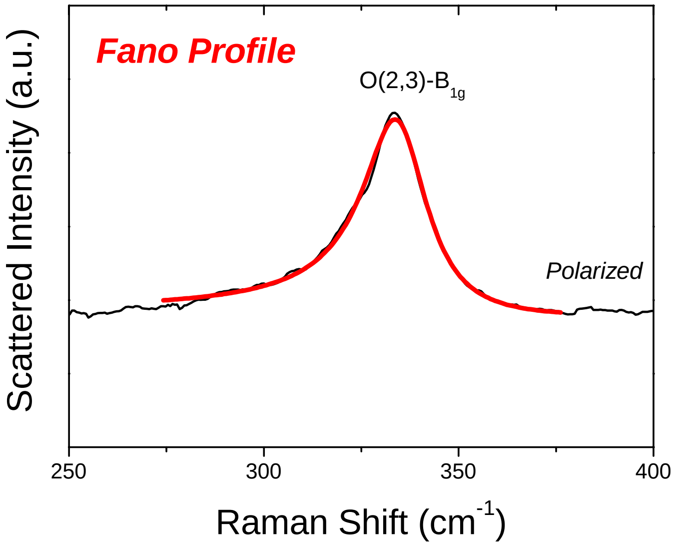

Figure 3.6. Fano profile fitting of O(2,3)-B_{1g} mode.

The Fano lineshape is related to the interference effects of two kind of the scattering sources in the material, *i.e.*, if two scattering sources, let's say a phonon (discrete), and electrons (continuous), do interfere coherently, destructive and constructive interference will influence the lineshape of the Raman spectra[3.5]. The overall result is that depending on the sign of the parameter q, the light scattering rate is enhanced on the low-energy side of the phonon peak and depressed in the high-energy side (for sign $q = -1$; for sign $q = +1$ the reverse is true). This produces an asymmetry of the phonon lineshape, which is referred as a Fano effect. In all the samples analysed, we observed that the Fano parameter was always negative.

2.- ***Lorentz* profile** (symmetric lineshape): The linear function response of the excitation amplitude (molecular vibration) of the medium responsible for the inelastic scattering due to the incident electric field $\mathbf{E}_i$ is a Lorentzian lineshape. Then, the line shape of +O(2,3)-A_g and O(4)-A_g modes are symmetric Lorentzian profiles. They were fitted by Lorentz profile equation (figure 3.7)

$$I_{A_g} = \frac{2A}{\pi} \frac{\gamma}{4(\omega - \omega_o)^2 + \gamma^2} + Const \tag{3.7}$$

where A is the area of the curve, ω_o is the phonon frequency, γ is the FWHM of the profile plus a constant background term.

Once obtained the integrated intensities of O(2,3) and O(4) phonon modes, those values are replaced in equations (3.2) and (3.5b) to obtain the uniaxial texture quality, δ, of the YBCO film.

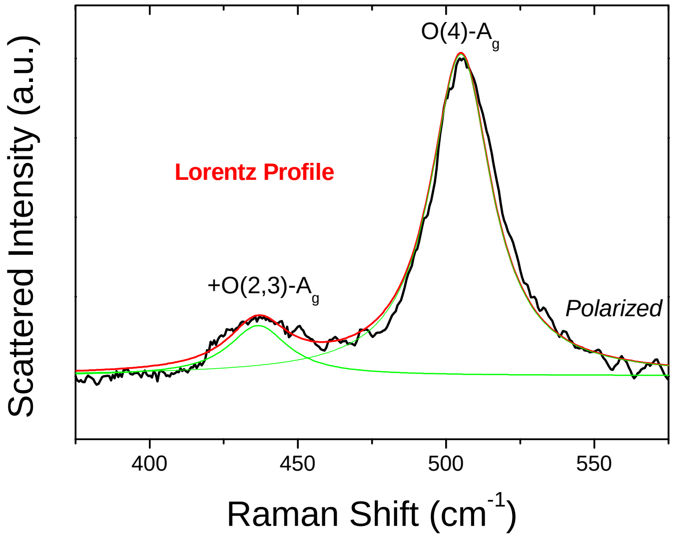

Figure 3.7. Lorentzian profiles fitting of +O(2,3)-A_g (green line) and O(4)-A_g (blue line) modes.

3.1.1.2. Study of uniaxial texture in YBCO films

We performed uniaxial texture studies of seven YBCO samples grown by different methods and with different *in-plane* texture characterized by different FWHM XRD ϕ-scan values from the (*102*) YBCO reflection expanding from 1.4 up to 17 degree (Table

3.5). The Δϕ final values of the YBCO are determined by the buffer layer texture above which YBCO grains grow. Five of them are YBCO CC, two YBCO samples grown onto IBAD substrates by PLD (figure 3.8b-c) and three YBCO samples grown onto RABiTS substrates by BaF_2 process(figure 3.8d). The last sample for comparison purposes, SS18 (figure 3.8a), is a YBCO thin film of 250 nm grown onto LAO single crystal by the TFA-MOD method[1.29] with a FWHM ϕ-scan of 1.4 degree.

A first PLD-IBAD sample, G3 (figure 3.8b), was prepared by depositing a YBCO film by standard PLD on a 20 nm CeO_2 buffered biaxially textured YSZ layer of 900 nm in thickness and deposited by IBAD on a polycrystalline YSZ substrate. It was 230 nm thick and had a ϕ-scan FWHM using the (102) reflection of 7.5 degree. The other two PLD-IBAD CC (figure 3.8c) were prepared by depositing a 1.6 μm thick YBCO film by a high rate PLD, on a non-magnetic Ni-Cr stainless steel ribbon of 100 μm buffered with a biaxially textured YSZ layer of 900 nm in thickness and deposited by IBAD[3.9]. NSS59-1 had a ϕ-scan FWHM value of 17.2 degree and NSS59-2 had a ϕ-scan FWHM value of 12.7 degree.

Table 3.5

YBCO samples for studies of the uniaxial and biaxial texture

	Δϕ (degree)	**Thickness (μm)**
MOD-TFA		
SS 18	1.4	0.30
BaF_2 Process		
F257	5.2	1.0
F260	6.6	2.40
F261	5.3	0.32
PLD		
G3	7.5	0.23
NSS59-1	17.2	1.60
NSS59-2	12.7	1.60

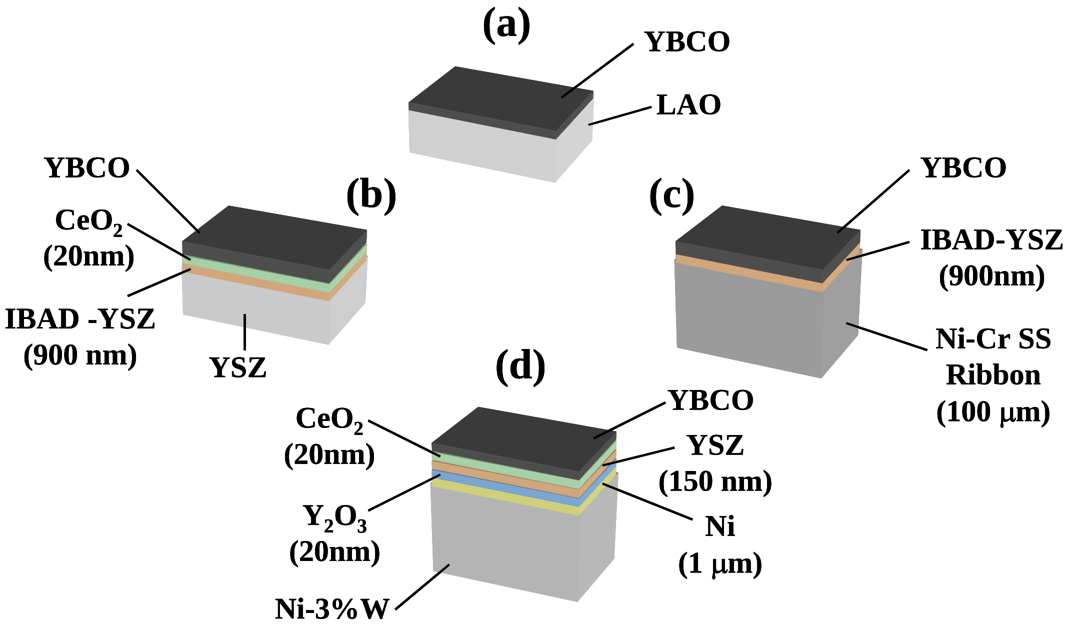

Figure 3.8. Scheme of the films structure analysed (a) TFA-MOD, (b),(c) PLD and (d) BaF_2 process .

The three BaF_2 process-RABiTS CC (figure 3.8d) were prepared by growing a YBCO film by a BaF_2 *ex-situ* process using evaporated precursors on a cube textured Ni tape microalloyed with 3% Wolfram with buffers of Ni (1μm), Y_2O_3 (20nm), YSZ (150nm) and CeO_2 (20nm)[3.10]. F261 was 0.32 μm thick, F257 was 1μm thick and F260 was 2.4 μm thick. Their FWHM ϕ-scan were 5.3, 5.2 and 6.6 degree, respectively.

A first sample characterization was performed by XRD technique. As the YBCO films are expected to be textured coatings, the YBCO grains are aligned in a preferred orientation along (00*l*) lattice planes. With a simple θ/2θ-scan the *c*-axis orientation fraction may be determined perpendicular to the substrate surface, as we will show later. Figure 3.9 shows the θ/2θ XRD patterns of a TFA-MOD, a PLD and a BaF_2 process samples as representative data, a large *c*-axis crystallinity and no signal of impurity or secondary phases was observed in all samples. For the TFA-MOD sample, called SS18 (figure 3.9a), a large *c*-axis crystallinity can be observed by strong (00*l*) peaks, corresponding to a *c*-axis oriented grain growth perpendicular to the LAO single crystal surface. Other phases and *a*-axis signal (like (*200*) profile) are not observed in the spectra.

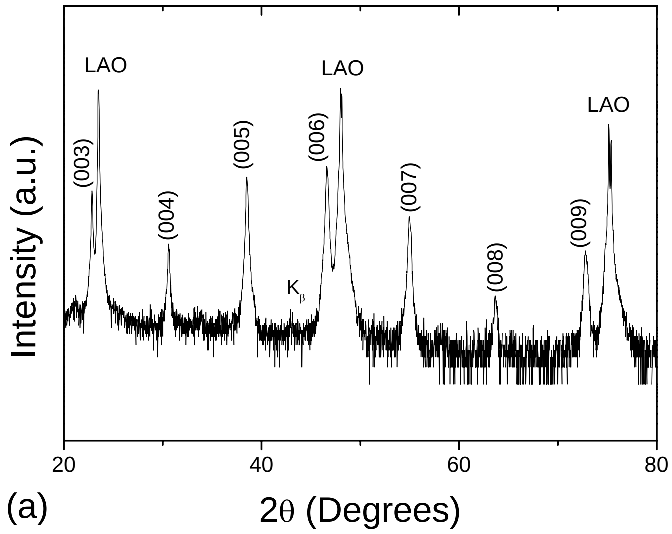

Figure 3.9. (a)

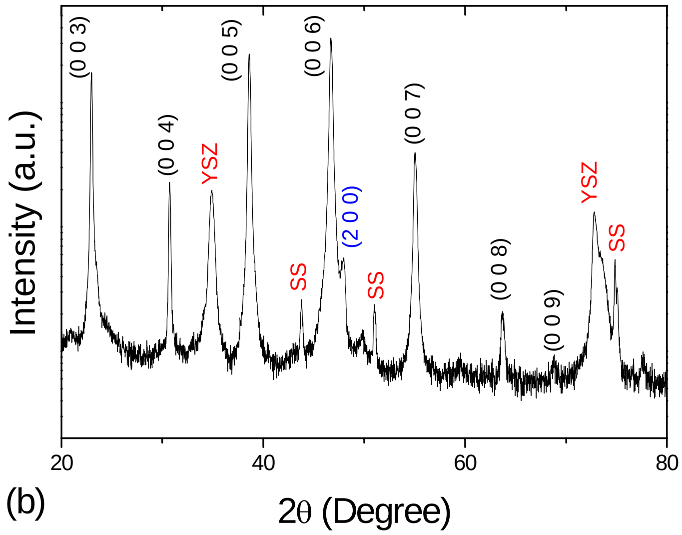

Figure 3.9. (b)

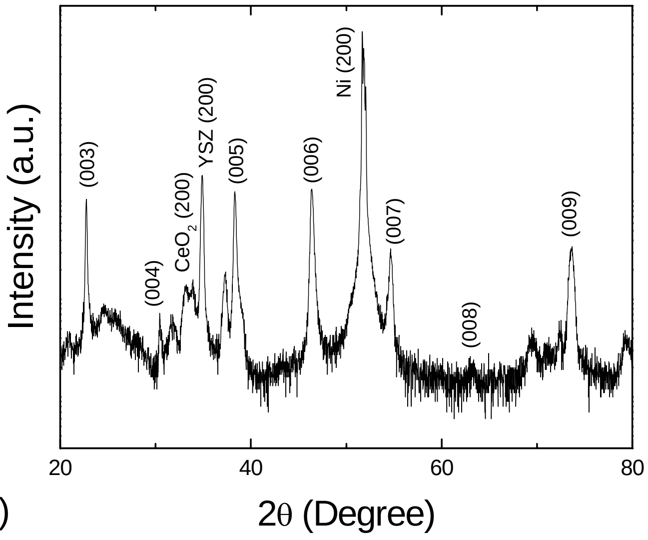

Figure 3.9. XRD patterns in logarithmic scale of (a) TFA-MOD (SS18) , (b) PLD (NSS59-2) and (c) BaF_2 process (F260) samples.

On the other hand, for PLD sample, called NSS59-2 (figure 3.9b), the (00*l*) peaks of YBCO observed are strong and indicating that the grains of the tape are *c*-axis oriented with regard to the substrate surface. Although it can also be observed a (*200*) peak corresponding to a small *a*-axis grains fraction grown perpendicular to the substrate (*a*-axis oriented grains percentage of ~ 3%, it has been stimated from XRD data as it will be explained later in this section). Peaks corresponding to the stainless steel substrate and YSZ buffer layer are also observed. No evidence of other phases is present as an indication that the YBCO is single phase.

Finally, for BaF_2 process sample (figure 3.9c), the (*00l*) reflections of YBCO can be observed, indicating that the tape has the *c*-axis perpendicular to the substrate. The (*200*) peak corresponding to the Ni textured substrate and the peaks corresponding to the CeO_2 (*200*) and YSZ (*200*) buffer layers, grown *cube on cube* onto the nickel substrate, are also observed.

The *out-of-plane* texture was characterized by measurements of the rocking curve and determining the FWHM of the (*005*) YBCO profiles, as shown in figure 3.10. For PLD samples we obtained FWHM ~ 4°, and for BaF_2 process FWHM ~ 5°. These values are clearly higher compared with YBCO films growth onto single crystals ($\Delta\omega$~ 0.4° – 0.7°).

As it is expected, in the case of YBCO tapes, the buffer layers have an *out-of-plane* misorientation higher than the single crystal. In fact, in some cases, the texture of the YBCO layer is improved in comparison to the texture of the buffer layer. For example, in the BaF_2 process sample, the nickel substrate has a FWHM ~ 17.5° and the buffer layers of YSZ and CeO_2 have a FWHM of 11.5° and 10.7° respectively. As we said before, the *in-plane* texture was characterized by measurements of ϕ-scan and determining the FWHM of (*102*) YBCO profiles, as shown in figure 3.11 and table 3.5.

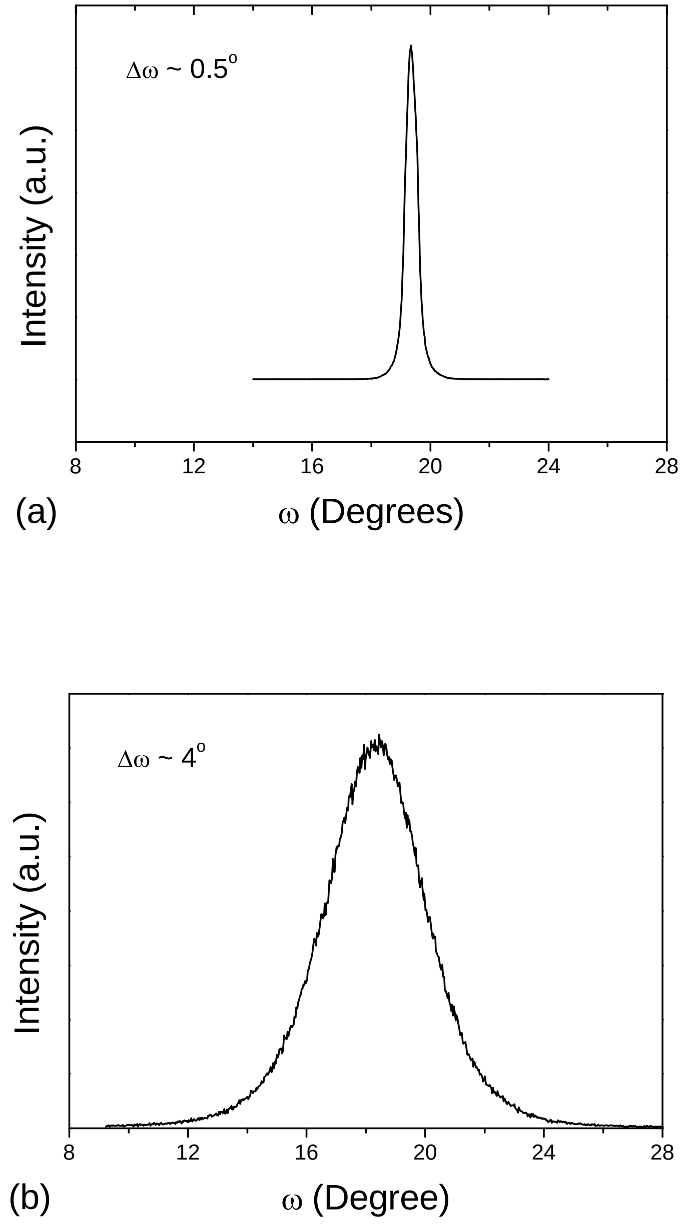

Figure 3.10. Rocking curve of the (*005*) YBCO reflection of (a) TFA-MOD sample SS18, and (b) PLD-IBAD sample NSS59-2.

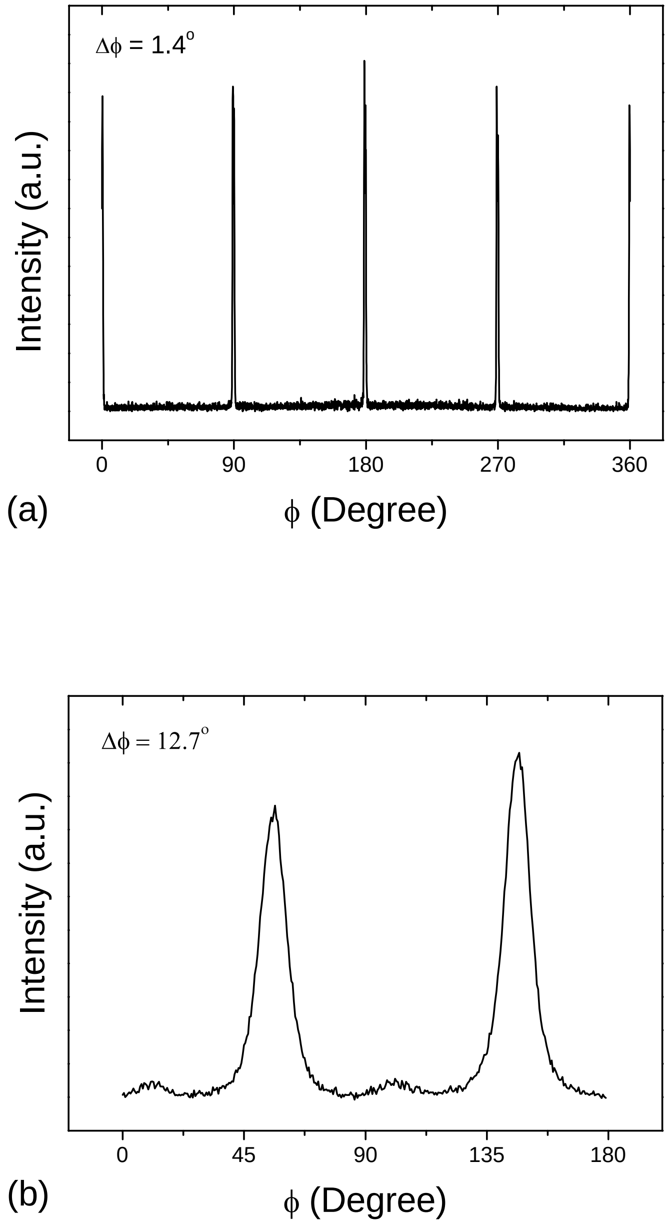

Figure 3.11. XRD ϕ-scan using the (*102*) YBCO reflection of (a) TFA-MOD sample SS18, and (b) PLD-IBAD sample NSS59-2.

The substrate of the PLD samples is polycrystalline, therefore it does not determine the texture of the YBCO film, rather the YSZ-IBAD textured buffer layer mainly gives the texture to the YBCO film (figure 3.12), while for BaF_2 process samples, the textured substrate transmits its texture to the buffer layers and YBCO film (figure 3.12). Therefore, the buffer layer texture determines the properties of the YBCO film.

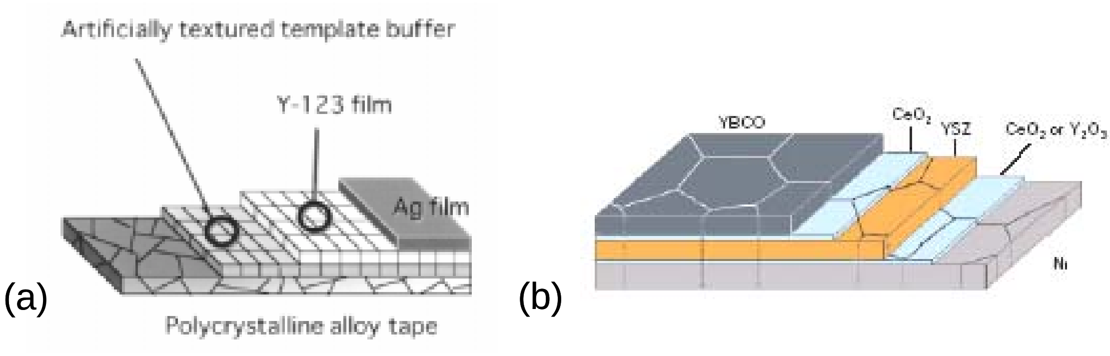

Figure 3.12. (a) A schematic description of biaxially aligned YBCO superconductor film using an artificially textured template or buffer layer growth by IBAD. (b) Schematic description of YBCO superconducting tape grown onto textured nickel substrate by RABiTS process. Notice the grain boundary of the metallic substrate is transferred through the different layers.

In order to summarize the quality of the YBCO samples analyzed in this section, we present in figure 3.13 the critical current density, J_c, at 77 K for the seven samples as a function of their FWHM XRD Δϕ using the (*102*) YBCO reflection. The critical current densities have been determined inductively as has been reported in reference [3.11] by using a SQUID. Notice that J_c follows the exponential decay with the misorientation angle in agreement with the literature[1.11] and as we saw in section 1.2.5, which further evidences that the degree of biaxial texture is the main factor determining the critical currents in these new granular materials.

Figure 3.14 shows the typical *polarized* Raman spectra observed for TFA, PLD and BaF_2 process films, where the strong intensity of the O(2,3)-B_{1g} mode and a weak O(4)-A_g phonon mode denote a large fraction of *c*-axis oriented perpendicular to substrate surface (buffer layer).

Following, we have determined the uniaxial texture, δ, of the films performing micro-Raman measurements. Figure 3.15 shows the δ-value extracted from Raman measurements as a function of the FWHM XRD Δϕ using the (*102*) YBCO reflection for all the samples investigated. Notice that all seven samples analyzed have δ values above 0.9 indicating that less than a 10% of the sample had *a*-axis grain growth. We have observed that there should not exist any correlation between the degree of *c*-axis grain fraction and the distribution of *in-plane* grain orientations.

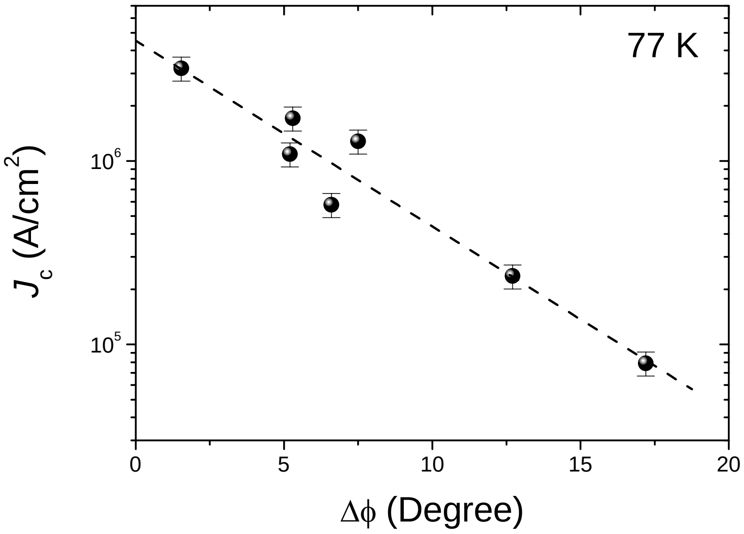

Figure 3.13. Critical current densities, J_c; at 77 K for all the different CC analyzed as a function of their ϕ-scan FWHM for the XRD (*102*) reflection

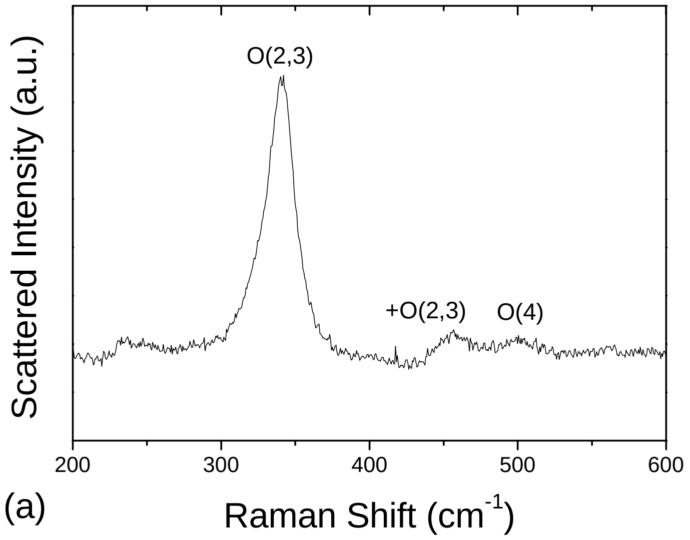

Figure 3.14. (a)

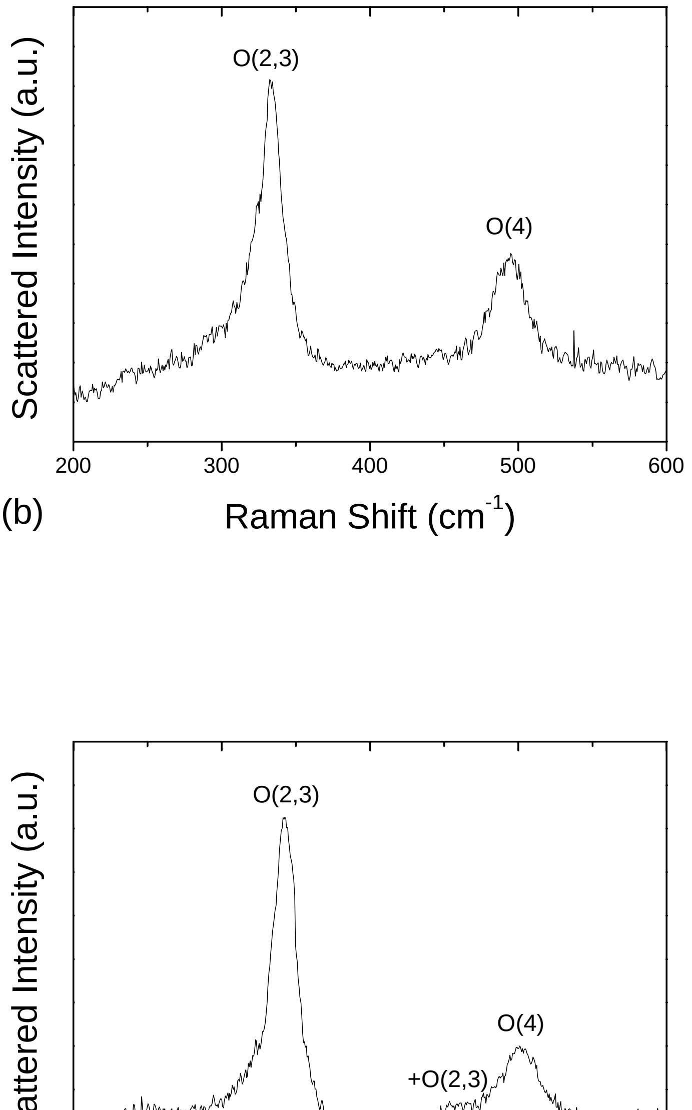

Figure 3.14. Typical *polarized* Raman spectra of (a) TFA-MOD sample SS18, (b) PLD-IBAD sample NSS59-2, and (c) BaF_2 process-RABiTS sample F260. Notice the strong intensity of O(2,3)-B_{1g} mode and a weak O(4)-A_g phonon mode denoting a large fraction of *c*-axis oriented grains.

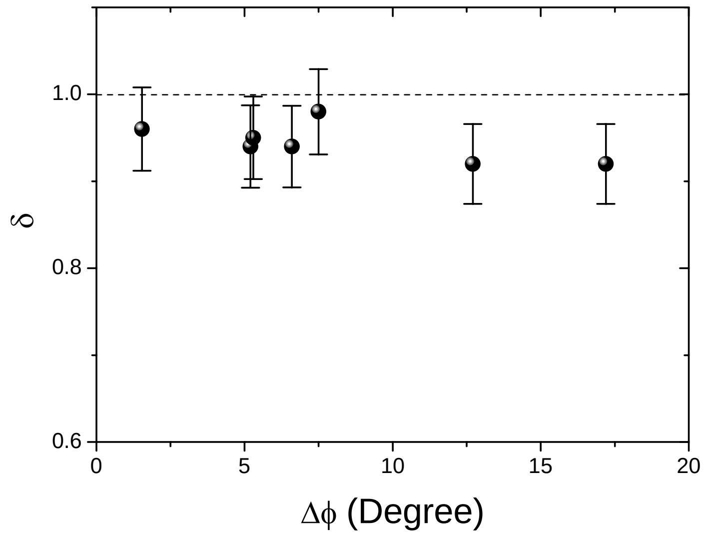

Figure 3.15. Uniaxial texture, δ, extracted from the Raman measurements as a function of the FWHM ϕ-scan XRD data (*102*) reflection.

The δ results shown in figure 3.15 indicate clearly a large *c*-axis grain fraction values near to 1, obtained by averaging 5 different 10μm laser spot (measuring time: 10 min/spot).

As we mentioned before, the *c*-axis grain fraction may be also stimated from XRD θ/2θ-scans, taking into account the structure factor of the Bragg reflections[3.12]. For a *c*-axis oriented film, only (*00l*) reflections are posible on the contrary perfectly *a*-axis oriented films will display only (*h00*) reflections. The *c*-axis grain fraction, f_c, measured by XRD θ/2θ-scan can be stimated from the following expression[3.4]:

$$\frac{I^{005}}{I^{200}} = \frac{f_c . I^{005}_{s\tan d}}{(1-f_c) . I^{200}_{s\tan d}} \qquad (3.8)$$

where I^{005} is the measured intensity of the (*005*)-peak, $I^{005}_{s\tan d}$ is the theoretical intensity of the (*005*)-peak, I^{200} is the measured intensity of (*200*)-peak, and $I^{200}_{s\tan d}$ is the theoretical intensity of (*200*)-peak. The theoretical intensities are $I^{005}_{s\tan d}$ = 13 and $I^{200}_{s\tan d}$ = 12, in percent of the (*103*) peak intensity, as measured on YBCO powder samples. We have applied this method to obtain the *c*-axis grain fraction. For example, for PLD-IBAD sample NSS59-2 shown in figure 3.9b the f_c value obtained was equal to 97% whereas the δ value obtained by micro-Raman was 92%. At the light of these results, a fairly good agreement within a ~ 5% was obtained between the two methods, XRD and micro-Raman. This demonstrates that micro-Raman spectroscopy is very suitable, non-destructive and quick technique to determine the *c*-axis grain fraction (*out-of-plane* texture) of CC samples. In the following section we will apply this methodology to perform local δ line scans on the studied films.

3.1.2. Local evaluation of uniaxial texture

Micro-Raman scattering offers the unique possibility to perform Raman-microprobe scans and to test the structure, homogeneity, crystalline texture and quantitative estimation of grain size and orientation of the films at a microscopic level. The advantages of this technique are that it is non destructive, no sample preparation is required, acquisition times are ~ 10 min/spot and spatial lateral resolution of ~ 1 μm can be obtained. As we mentioned in section 2.1.2, the penetration depth of the 514.5 nm visible light in YBCO is only ~80nm[2.2,2.3], thus enabling this technique for depth homogeneity studies of the YBCO films. We have tested this capability in YBCO TFA-MOD and CC samples.

3.1.2.1. δ line scans

For the production of high quality YBCO tapes, it is very important to have a precise control of the processing parameters to reach a good homogeneity of the films. The lack of homogeneity arises, among others causes from different orientation of the grains. In particular, grains with *c*-axis perpendicular or parallel (*a*-axis) to the substrate surface. Micro-Raman spectroscopy enables us to determine the profiles of *c*-axis grain fraction of the CC top layer surface. The samples were mounted in X-Y stage of the microscope table (figure 2.3a) and all measurements were made at room temperature.

Figures 3.16a-c show the δ lineal scans performed to the samples SS18, NSS59-2 and F260, with lineal steps of Δx ~ 2μm, ~ 1μm and ~ 2μm, respectively. These measurements have enabled to determine the degree of *c*-axis fraction in each measured position following the model described in section 3.1.1.2 and, therefore, we have evaluated if the YBCO layers have long range crystal orientation over distances much larger than the diameter of the focused laser beam. For this reason the laser spot used was ~1 μm. We observed that the SS18 sample has dominant *c*-oriented grain colonies of ~ 12 μm in size and small *a*-axis grain colonies of ~ 2.5 μm in size as represented in figure 3.16a, whereas sample NSS59-2 is a dominant *c*-oriented grain sample with the appearance of some *a*-oriented grains of ~ 2 μm size, randomly distributed as illustrated in figure 3.16b and finally, the sample F260 is a perfect *c*-crystal film within the experimental error as clearly observed in figure 3.16c, due to the δ values were closed to 1.

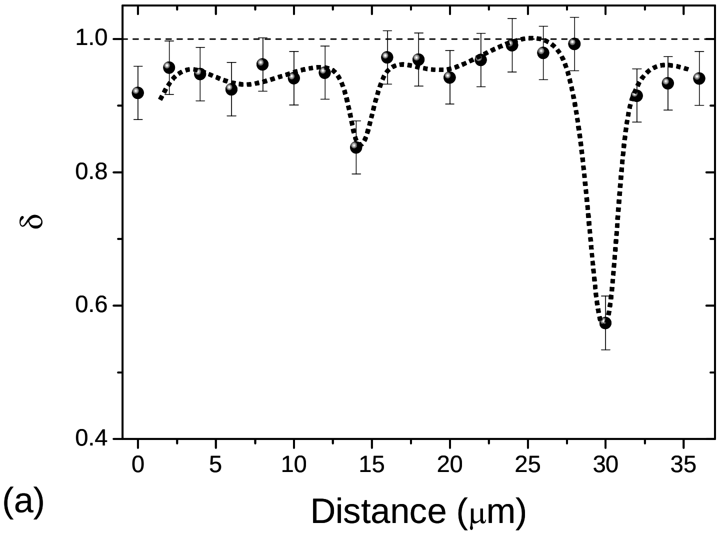

Figure 3.16. (a)

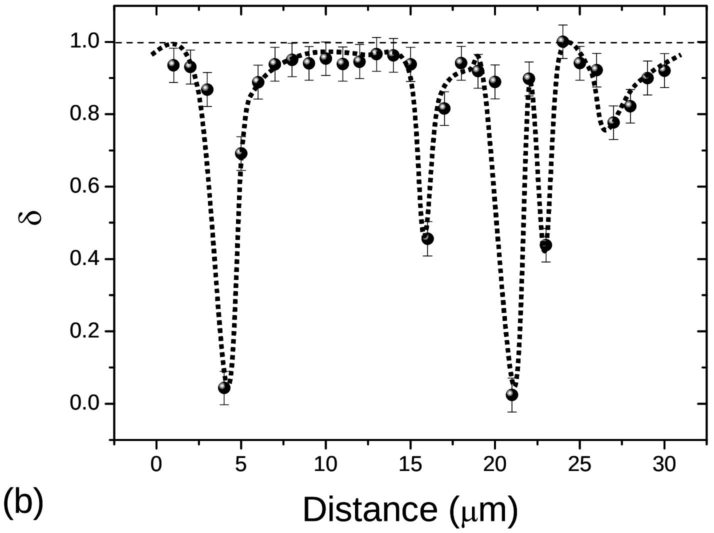

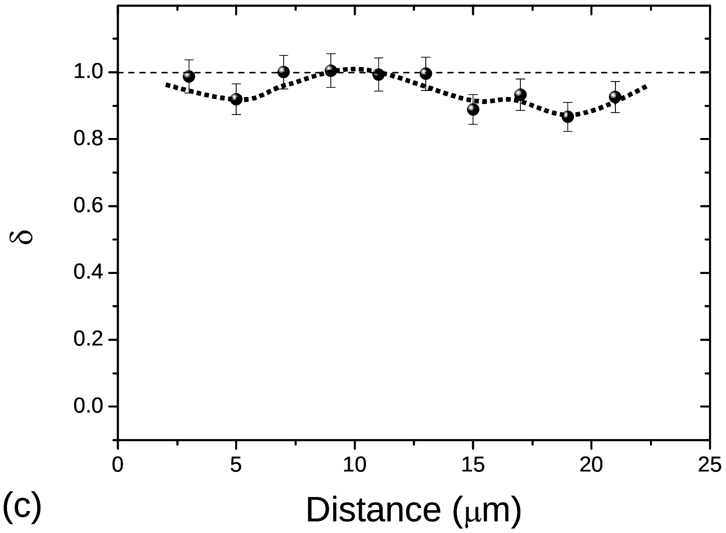

Figure 3.16. Lineal δ scans of samples: (a) TFA-MOD SS18 with Δx ~ 2 μm, (b) PLD-IBAD NSS59-2 with Δx ~ 1 μm, and (c) BaF_2–process-RABiTS F260 with Δx ~ 2 μm.

We conclude that micro-Raman spectroscopy is a very suitable technique to determine the uniformity of the uniaxial texture of YBCO films, to identify the appearance of *a*-crystals even in large *c*-crystal fraction samples and to estimate their size and distribution. In the following section we will investigate the *in-plane* texture of these samples by micro-Raman.

3.2. Determination of Biaxial Texture in YBCO films

As we saw in section 1.4.3, the intensity of the Raman signal in crystalline YBCO strongly depends on the scattering geometry and the relative orientation between the sample and the polarization direction of the incident and scattered light. This makes it possible to find the directions of the crystallographic axes of the film crystals in relation to the substrate axes, *i.e.* the degree of *in-plane* orientation. By rotating the angle φ, between the crystallographic axes of the film crystals and the polarization direction of the incident laser, the scattered intensity for O(2,3)-B_{1g} and O(4)-A_g modes in *polarized* and *depolarized* geometries oscillates generating an angular modulated function. To demonstrate this behaviour, we present below the analysis of O(2,3)-B_{1g} phonon mode Raman intensity for backscattering in the *c*-face of an YBCO crystal.

We consider a fixed space Cartesian system x, y, z with an orthorhombic YBCO crystal oriented such that the *c* axis coincides with the z axis while *a* axis is rotated an arbitrary angle (φ) from the x axis (figure 3.17). The Raman scattering tensor of the crystal B_{1g} mode can be expressed in the x, y, z, system as:

$$\vec{R}^{xyz}_{B_{1g}} = \Phi_{xyz}\vec{R}_{B_{1g}}\tilde{\Phi}_{xyz} \tag{3.9}$$

where Φ is the transformation matrix that is orthogonal, with elements that are direction cosines expressed in terms of Euler's angles. For the geometry shown in figure 3.17, the Φ matriz can be expressed as

$$\Phi_{xyz} = \begin{pmatrix} \cos\varphi & \sin\varphi & 0 \\ -\sin\varphi & \cos\varphi & 0 \\ 0 & 0 & 1 \end{pmatrix} \tag{3.10}$$

For the incident and scattered laser traveling along the crystal c axis (coincides with the z axis) while both incident and scattered polarized light in the x-axis direction (Porto notation $z(x,x)\bar{z}$), the incident and scattered electric vectors can be expressed in x, y, z notation as

$$\mathbf{e}_i = \begin{pmatrix} 1 & 0 & 0 \end{pmatrix}, \mathbf{e}_s = \begin{pmatrix} 1 \\ 0 \\ 0 \end{pmatrix} \tag{3.11}$$

Using the table 3.1 and the equations (3.9), (3.10) and (3.11), the Raman intensity for B_{1g} mode can be expressed as

$$I_{B_{1g}}^{Polarized} = x_{B_{1g}}^2 (\sin^2\varphi - \cos^2\varphi)^2 \tag{3.12}$$

$$I_{B_{1g}}^{Depolarized} = 4.x_{B_{1g}}^2 \sin^2\varphi \cos^2\varphi \tag{3.13}$$

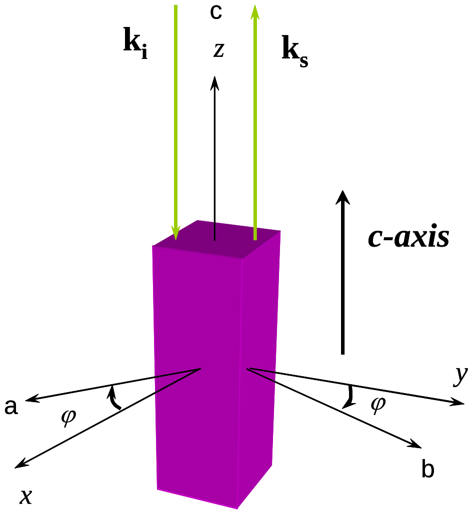

Figure 3.17. Schematic arrangement showing crystal and laboratory axes considered in the analysis.

The Raman intensity of equations (3.12) and (3.13) oscillate between 0 and 8.5 by an angular modulated function such as $(\sin^2\varphi - \cos^2\varphi)^2$ and $(\sin^2\varphi\cos^2\varphi)$ respectively, as clearly represented in figure 3.18.

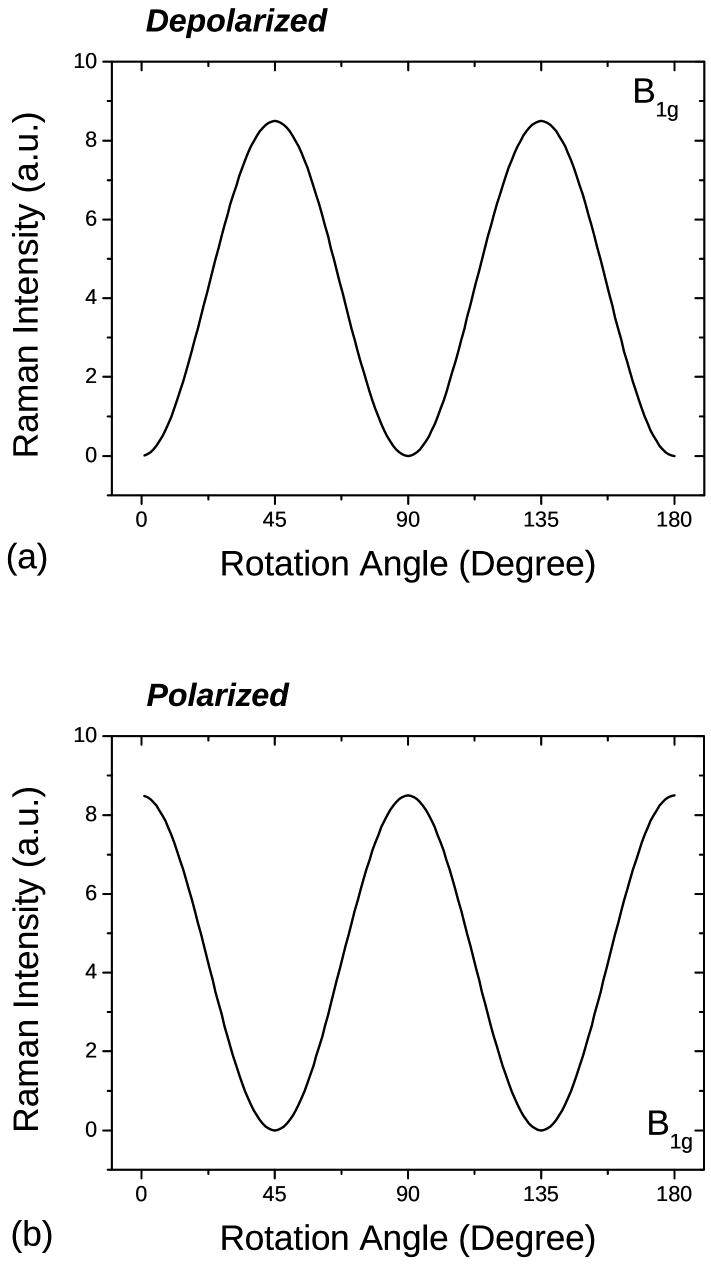

Figure 3.18. Intensity modulation of the O(2,3) mode as a function of the angle between crystallographic axes of the crystal and the electric vector of the incident laser, with a modulation period of 90 degree. (a) Depolarized and (b) polarized scattering.

In the literature, we have found preliminary studies that showed the capabilities of micro-Raman scattering to analyze the *in-plane* texture of YBCO films [3.7, 3.13, 3.14]. Thomsen *et al*[3.14] investigated the degree of *in-plane* orientation of YBCO films consisting only of *c*-axis oriented crystals. Dieckmann *et al*[3.7] extended the evaluation of the degree of epitaxy to the case where the superconductor films include *a*-axis and *c*-axis oriented crystallites. In these previous works, the samples were considered as a mixture of completely *in-plane* oriented and completely *in-plane* random oriented crystals. We have developed a simple and truthful method for easier and practical characterization of *in-plane* texture of YBCO CC by Raman spectroscopy, which in addition takes into account the distribution of misoriented grains, as we will show in the following section.

3.2.1. *In-plane* orientation

As it was mentioned in section 3.1.1.2, we are dealing with textured coatings characterized by a grain misorientation distribution, directly related to the $\Delta\phi$ ($1.4^o < \Delta\phi < 17^o$). As we have seen in section 3.1 and figure 3.15, the samples investigated have high values of $\delta \sim 0.95$, *i.e.* the uniaxial texture values are close to fully *c*-axis oriented films ($\delta = 1$). Therefore, we will neglect the contribution of *a*-axis oriented grains in the following theoretical model proposed. Thus, to extract information on the *in-plane* orientation of these highly *c*-axis oriented films under study, we are going to consider the simplified equations with $\delta \sim 1$ as a good approximation.

Theoretical Model:

The theoretical model proposed considering the angular dependence of the Raman intensity $I(\varphi)$ scattered from a CC sample is dependent on the grain misorientation distribution present in the particular sample. The rotation angle φ, is defined as the angle between the sample edge and the polarization direction of the incident laser light denoted by unit vector $\mathbf{e}_i$, as clearly illustrated in figure 3.19. For the angular dependence of the Raman intensity of a particular phonon mode, we can write the equation:

$$I_R(\varphi) = \sum_{i=0}^{n} P_i(\theta_i) I(\varphi + \theta_i) \tag{3.14}$$

where $P_i(\theta_i)$ is defined as the fraction of crystals with a misorientation angle θ_i according to some angle distribution function (figure 3.20), and $I(\varphi + \theta_i)$ is its Raman intensity angular φ dependence.

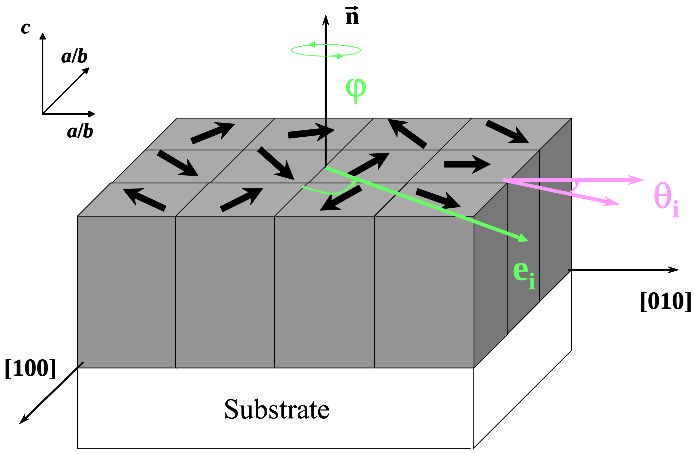

Figure 3.19. Scheme of rotation angle φ and misorientation angle θ_i between grains for a fully *c*-axis oriented YBCO film (δ ≈ 1).

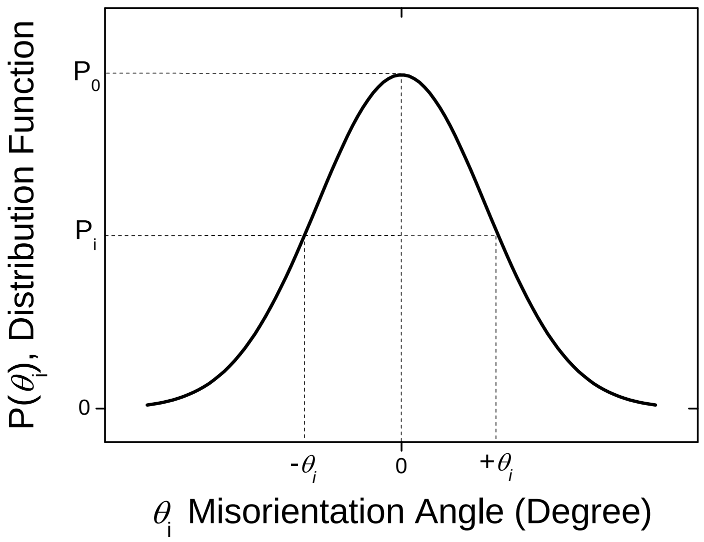

Figure 3.20. Orientation distribution function, P(θ_i), of the YBCO crystals with *in-plane* misorientation angle θ_i.

From equation (3.14) the expressions for the angular Raman intensity dependence of the O(2,3)-B_{1g} and O(4)-A_g modes in *polarized* and *depolarized* scattering geometries is determined by contracting their respective Raman tensors. Thus, due to the fact that the films have large *c*-axis grain fraction, the equation (3.1) for δ ~ 1 is reduced to:

$$I_R(\varphi) \approx \delta . I_c(\varphi) \quad (3.15)$$

Then, the expression for the intensity dependence on the rotation angle φ, of the *depolarized* spectra for the O(2,3)-B_{1g} mode, is expressed by replacing the equations (3.13) and (3.14) into equation (3.15):

$$I_{B_{1g}}^{depolarized}(\varphi) = \delta.\sum_{i=0}^{n} P_i(\theta_i)\left[4x_{B_{1g}}^2 \sin^2(\varphi+\theta_i).\cos^2(\varphi+\theta_i)\right]$$

(3.16)

expanding the equation (3.16) and reagruping common terms we get:

$$I_{B_{1g}}^{depolarized}(\varphi) = 4\delta.x_{B_{1g}}^2\left[\sum_{i=0}^{n} P_i(\theta_i) - 8\sum_{i=0}^{n} P_i(\theta_i)\sin^2\theta_i\cos^2\theta_i\right]\sin^2\varphi.\cos^2\varphi + \\ + 4\delta.x_{B_{1g}}^2\sum_{i=1}^{n} P_i(\theta_i)\sin^2\theta_i\cos^2\theta_i$$

(3.17)

Taking a continuous distribution of possible angles, *i.e.*, changing the summatory to an integral and being A the total grain population (the area under the distribution function of figure 3.20) verifing:

$$A = \int_{-\pi}^{+\pi} P(\theta).d\theta$$

(3.18)

The intensity dependence on the rotation angle of the depolarized spectra for the O(2,3) mode can be written as:

$$I_{B_{1g}}^{depolarized}(\varphi) = 4\delta.x_{B_{1g}}^2\left[A - 8\int_{-\pi}^{+\pi} P(\theta)\sin^2\theta\cos^2\theta d\theta\right]\sin^2\varphi\cos^2\varphi \\ + 4\delta.x_{B_{1g}}^2\int_{-\pi}^{+\pi} P(\theta)\sin^2\theta\cos^2\theta d\theta$$

(3.19)

According to equation (3.19), we can write the scattered intensity as a term k_1 oscillating in φ like $\sin^2\varphi\cos^2\varphi$, plus a φ- independent k_2 term , each term defined as:

$$k_1 = 4\delta . x_{B_{1g}}^2 \left[A - 8\int_{-\pi}^{+\pi} P(\theta)\sin^2\theta\cos^2\theta d\theta \right] \tag{3.20}$$

$$k_2 = 4\delta . x_{B_{1g}}^2 \int_{-\pi}^{+\pi} P(\theta)\sin^2\theta\cos^2\theta d\theta \tag{3.21}$$

therefore, we can re-write equation (3.19) as:

$$I_{B_{1g}}^{depolarized}(\varphi) = k_1 \sin^2\varphi\cos^2\varphi + k_2 . \tag{3.22}$$

The magnitude of the term oscillating in φ is a direct measure of the degree of *in-plane* texture in a given sample. Then, we can define a texture parameter Q_c as the coefficient of the term oscillating in φ in a given sample normalized to the same coefficient for a perfectly epitaxial oriented film ($k_1 = 4A\delta . x_{B_{1g}}^2$),

$$Q_c = \frac{k_1}{4A\delta . x_{B_{1g}}^2} = \frac{k_1}{k_1 + 8k_2} = \frac{\dfrac{k_1}{k_2}}{\dfrac{k_1}{k_2} + 8} \tag{3.23}$$

A highly textured sample will be characterized by values of the Q_c parameter close to unity. On the contrary, poorly textured samples will have Q_c values close to zero, as schematically represented in figure 3.21.

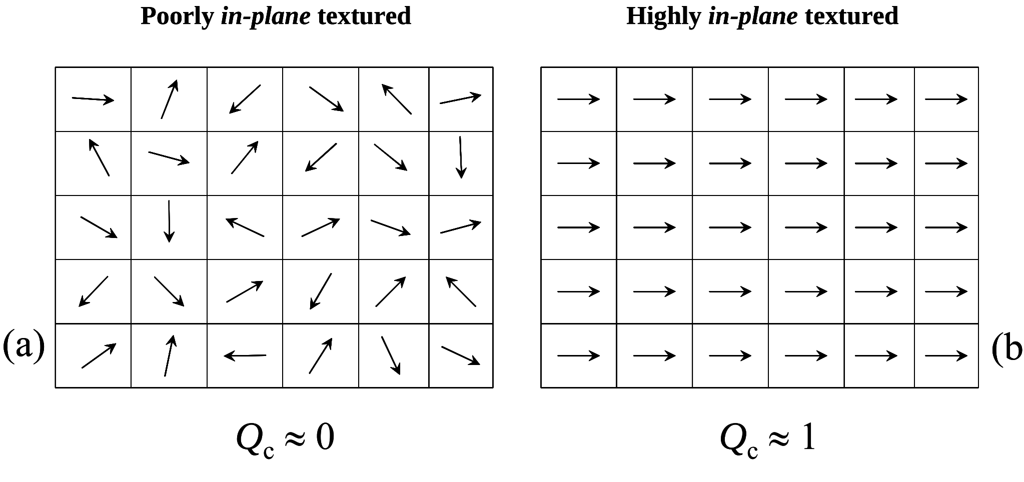

Figure 3.21. Scheme of films with Q_c values close (a) to zero and (b) to unity. The arrows represent the *a*-axis of the YBCO crystals.

The same treatment can be applied to analyze the angular dependence of the Raman intensity of the O(2,3) mode measured in *polarized* scattering configuration by replacing the equations (3.12) and (3.14) into (3.15). The equation that describes the Raman intensity modulation in this case is:

$$I_{B_{1g}}^{polarized}(\varphi) = \delta.x_{B_{1g}}^{2}\left[A - 8\int_{-\pi}^{+\pi} P(\theta)\sin^{2}\theta\cos^{2}\theta d\theta\right](\sin^{2}\varphi - \cos^{2}\varphi)^{2} + 4\delta.x_{B_{1g}}^{2}\int_{-\pi}^{+\pi} P(\theta)\sin^{2}\theta\cos^{2}\theta d\theta \qquad (3.24)$$

Or rewriting it like a function of oscillating and no oscillating terms by using the equations (3.20) and (3.21):

$$I_{B_{1g}}^{polarized}(\varphi) = \frac{1}{4}k_{1}(\sin^{2}\varphi - \cos^{2}\varphi)^{2} + k_{2} \qquad (3.25)$$

This formulation is completely general and enables us to assume different distribution functions, *P(θ)*, in order to further analyze the material and thus provide information on the grain orientation distribution function present in a particular sample. A given distribution function reflects the abundance of different grain orientations in the film plane. We have calculated the theoretical dependence of the texture parameter, Q_c, as a function of the FWHM of three grain orientation distribution functions: (a) Epitaxy and Random, (b) Gaussian and (c) Lorentzian model, which are illustrated in figure 3.22.

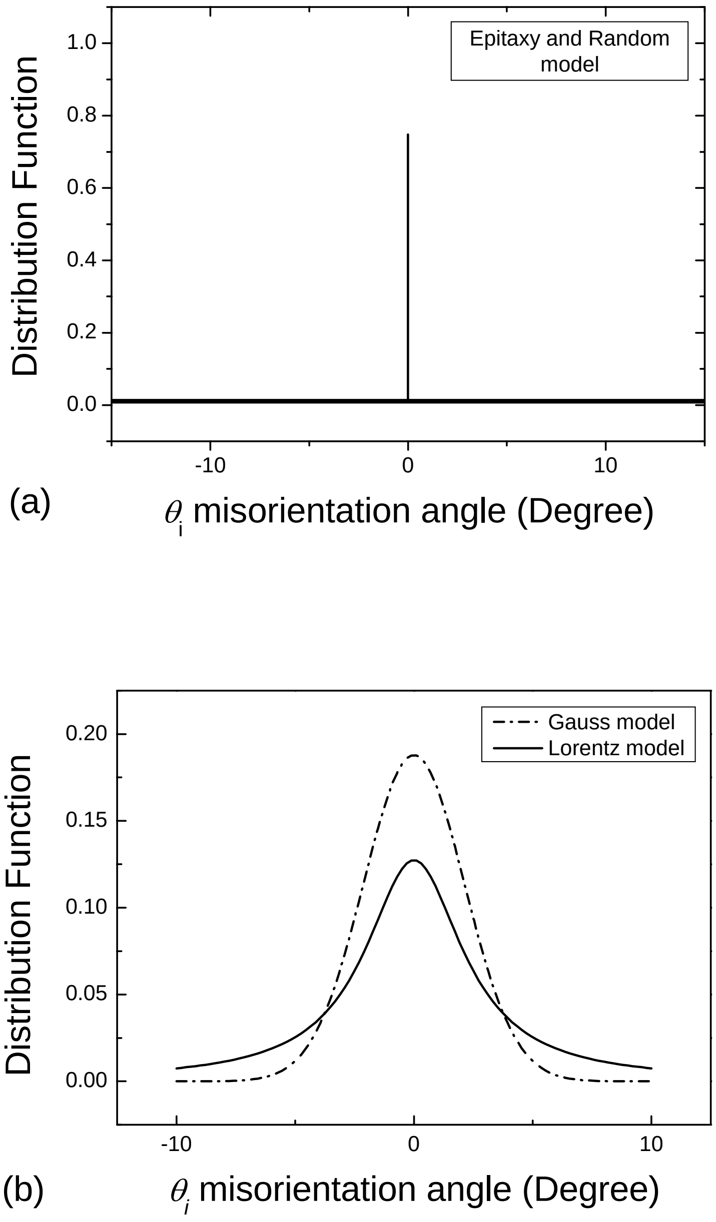

Figure 3.22. Graphs of the three distribution functions: (a) Epitaxy and Random, (b) Gaussian and Lorentzian with FWHM $\Delta\theta \sim 5^{\circ}$. The distribution functions are normalized and the area under the curve is equal to 1.

In the most simple approximation, we considered that the films consist of a perfectly *in-plane* oriented and a randomly *in-plane* oriented parts (a simple 1 or 0 model, as represented in figure 3.22a). The intensity of the signal scattered from the perfectly *in-*

plane oriented fraction is dependent of the rotation angle φ, and the intensity scattered from the randomly *in-plane* oriented fraction is φ independent:

$$I_R(\varphi) = \delta.I_c^{epitaxy}(\varphi) + \delta.I_c^{random}\,. \tag{3.26}$$

To perform a comparison among the theoretical curves of the different orientation distribution function, we have taken the value of the maximum of a normalized Gaussian function as the magnitude of the perfectly *in-plane* oriented part. As it can be seen in figure 3.23, the Q_c parameter value decays very fast to values close to zero ($Q_c \propto 1/\Delta\phi$). A similar model was previously assumed in Raman studies[3.7,3.14] analyzing the biaxial texture of YBCO films.

In order to formulate a more realistic view of the CC samples, a Gaussian and a Lorentzian distribution of the grain orientation have now been considered with the appropriate normalizations of equation (3.19). The Q_c values for Lorentzian and Gaussian dustributions were obtained by resolving numerically the integral,

$$\int_{-\pi}^{+\pi} P(\theta)\sin^2\theta.\cos^2\theta.d\theta\,, \tag{3.27}$$

for each angle θ. Then, we replaced its value into the equations (3.20) and (3.21) to get the k_1 and k_2 parameters. Finally we put these values into equation (3.23) to obtain the Q_c dependence on the distribution FWHM as represented in figure 3.23.

Figure 3.23 shows that the decay of the texture parameter Q_c with increasing FWHM of the distribution is moderate for the Lorentzian grain distribution and it goes to zero at a slower rate for a Gaussian grain distribution. It is clear from this theoretical study that the underlying physics of the material will be determined by the particular distribution of the misoriented grains, and therefore these results validate the importance of modelling the Raman scattered intensities by using distribution functions.

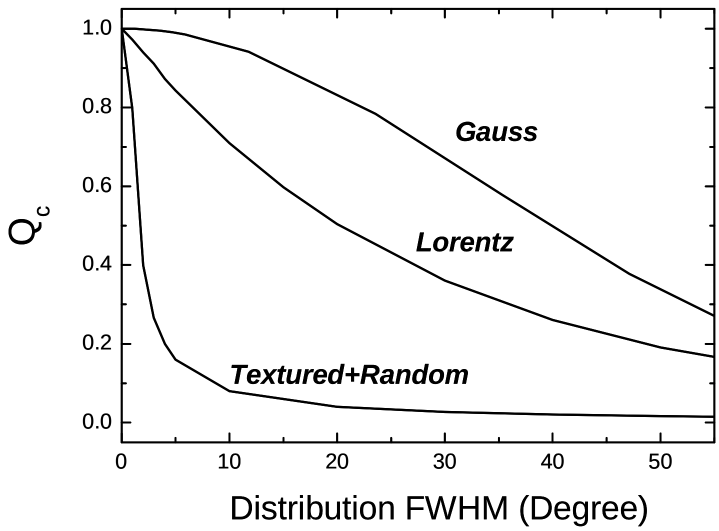

Figure 3.23. Theoretical dependence of the texture parameter Q_c as a function of the FWHM of the three different grain orientation distribution functions.

Experimental Results:

From the experimental point of view, the Raman intensity modulation were verified by rotating the sample from $\varphi = 0^{o}$ to $\varphi = 120^{o}$ degrees and measuring the corresponding *polarized* and *depolarized* Raman spectra every 6^{o}. The samples were mounted on a rotational microscope table (figure 2.3b) whose perpendicular axis was carefully aligned with the optical axis of the microscope, so that always the same spot of the film remained in the focus during rotation and all measurements were made at room temperature.

The experimental values of the angular dependence of the integrated Raman intensity of the O(2,3)-B_{1g} mode in the *depolarized* geometry for NSS59-2 sample are displayed in figure 3.24a. Also shown is the corresponding best fit function according to equation (3.22). The values of k_1 and k_2 are determined from the numerical fit to the experimental Raman data. Q_c can be directly calculated using equation (3.23) from the value of k_1/k_2 evaluated from the fit to the experimental data. Expressing Q_c as a function of the k_1/k_2 ratio has the advantage to eliminate contributions of the particular detection system efficiency, the actual values of the Raman tensor elements, integration time, etc. The value of Q_c obtained for this particular case when applying equation (3.23) is Q_c = 0.68±0.05. For samples with δ >0.9, that is the case for all the samples analyzed in this work, the Q_c values estimated from equation (3.23) differ in less than a 3% from those determined considering the *c*- and *a*-axis crystal population.

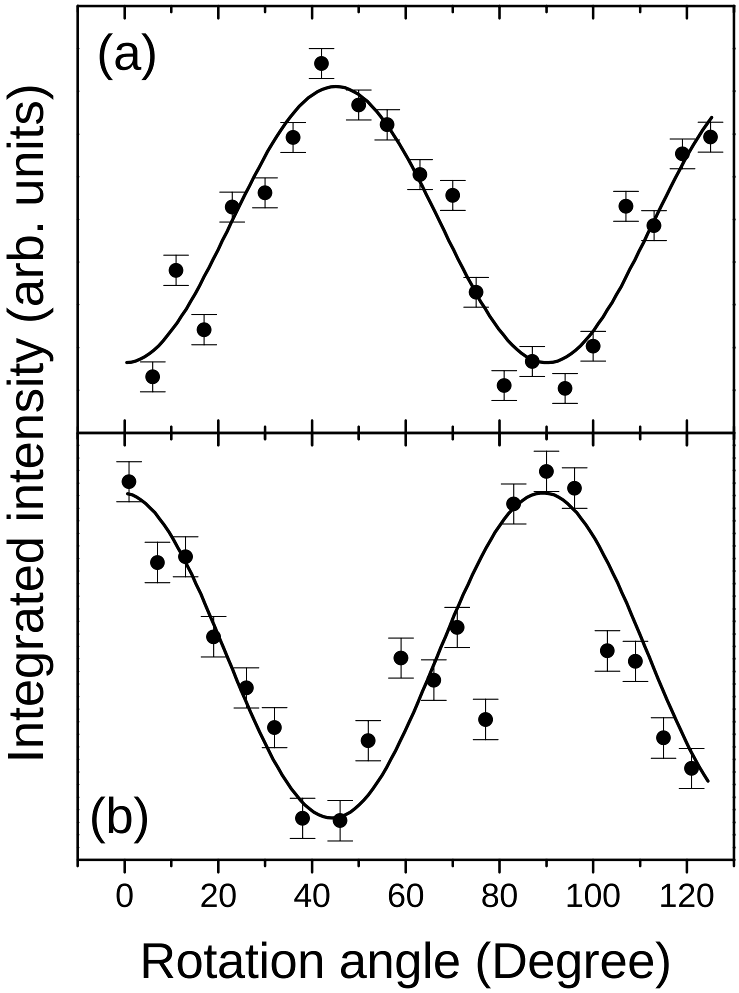

Figure 3.24. Angular dependence of the integrated Raman intensities of the O(2,3)-B_{1g} mode: (a) *depolarized*, and (b) *polarized* scattering geometry, in NSS59-2 sample. The lines are the best fit values with δ= 0.92 and Q_c = 0.68 ± 0.05.

We have confirmed that the value of Q_c obtained from the fit to the *depolarized* configuration, also fits the angular dependence of the Raman intensity of the O(2,3) mode when measured in the *polarized* scattering configuration. We show in Figure 3.24b, the experimental angular Raman intensity oscillations of the O(2,3) phonon mode measured in *polarized* scattering geometry for the NSS59-2 sample together with the calculated intensity oscillation using equation (3.25) and the parameter values encountered in figure 3.24a, $\delta = 0.92$ and $Q_c = 0.68 \pm 0.05$. Notice that a good agreement is obtained between theory and experiment. Similar agreement is also obtained for the other samples. Therefore, we can conclude that in order to determine the Q_c parameter only the *depolarized* Raman spectra of the O(2,3)-B_{1g} mode is required to be analyzed.

Figure 3.25 displays the Q_c experimental values determined by using equation (3.23) as a function of the FWHM ϕ-scan (*102*) reflection for the *c*-crystal domain for all the samples analyzed. A relationship is obtained between the Q_c parameter determined by micro-Raman and the XRD ϕ-scan data, indicating that indeed both parameters are quantitatively related to the degree of biaxial texture of YBCO CC. Furthermore, it can be seen that an extremely good agreement with the experimental Raman results is obtained when using the Lorentz distribution function in our model. We conclude then, that micro-Raman is an interesting technique to investigate, non destructively, the grain orientation distribution function of YBCO tapes.

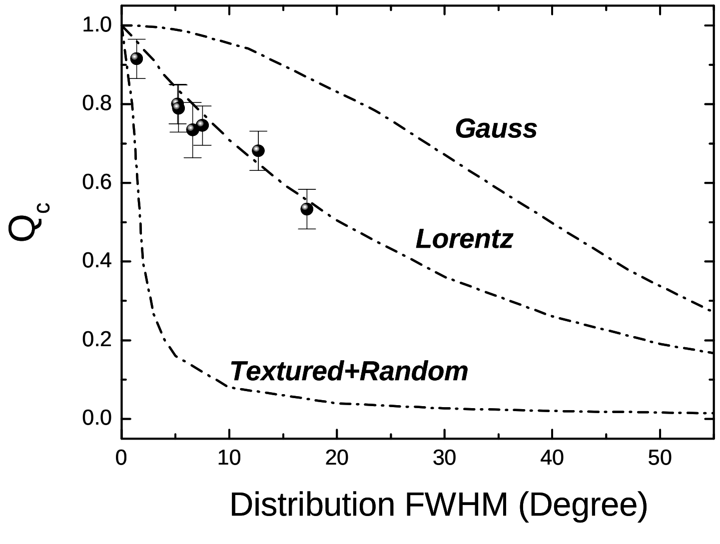

Figure 3.25. Theoretical dependence of the texture parameter Q_c as a function of the FWHM of three different grain orientation distribution functions. Dots are the experimental Q_c values determined from micro-Raman measurements using Eq. (3.23) for all the samples analyzed as a function of the FWHM ϕ-scan (*102*) XRD reflection.

Moreover, the exponential decay of J_c with *in-plane* texture presented in figure 3.13 can now be described by the Q_c texture parameter, as shown in figure 3.26. This figure shows the direct relationship existing between the Q_c parameter value calculated from the micro-Raman measurements in different kind of CC and the critical current densities J_c at 77K. Micro-Raman scattering appears then as a technique to also investigate the superconducting properties of CC. Notice that in order to be at $J_c > 1\text{MA/cm}^2$ (required for applications of CC), the $Q_c > 0.80$ which corresponds in the Lorentzian distribution to $\Delta\phi \sim 5^o - 7^o$ degree.

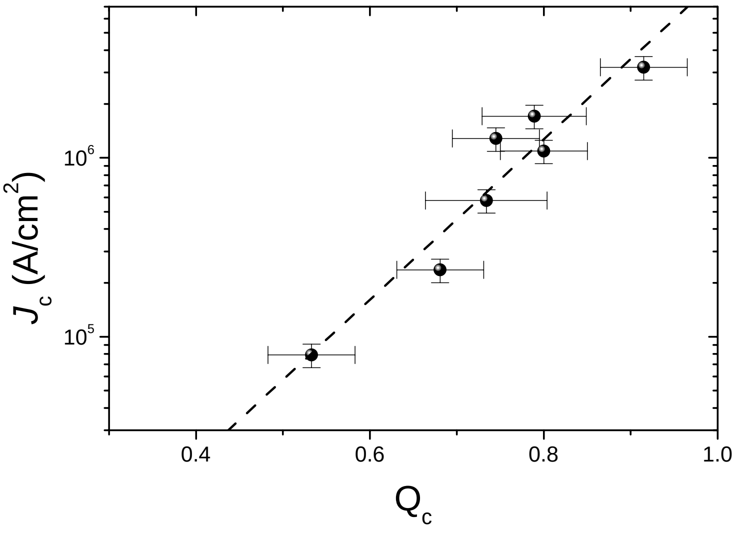

Figure 3.26. Critical current densities, J_c; at 77 K as a function of the texture parameter Q_c, determined from micro-Raman measurements using equation (4.17) for all the different coated conductors investigated in this work

3.2.2. Local evaluation of biaxial texture

We have next evaluated the feasibility of micro-Raman to determine the uniformity of the *in-plane* texture of CC. We have used the model described in the previous section to estimate Q_c at different points of samples with a large fraction of *c*-axis grain growth (δ>0.90). We further simplified the experimental procedure to end up with a practical method to evaluate the local biaxial texture of YBCO CC. We determined the intensity oscillations only by measuring the *depolarized* scattering configuration of the O(2,3)-B_{1g} Raman mode at angle steps of 45 degrees between 0° and 135° in order to minimize the measuring and evaluation times. This experimental simplification will enable us to determine the structure parameter Q_c in several sample positions in a reasonable time scale (10 min/spot).

Figure 3.27 shows the experimental values of the angular intensity dependence of the depolarized O(2,3)-B_{1g} Raman mode and the corresponding best fit function according to equation (3.22) for the G3 IBAD sample. The Q_c value estimated for this particular sample and position according to equation (3.23) is $Q_c = 0.77 \pm 0.05$, which is within the error bar of the value extracted from the full oscillation analysis shown in figure 3.24 ($Q_c = 0.75 \pm 0.05$). This justifies the reduction of the experimental measurements down to four φ values for the determination of Q_c.

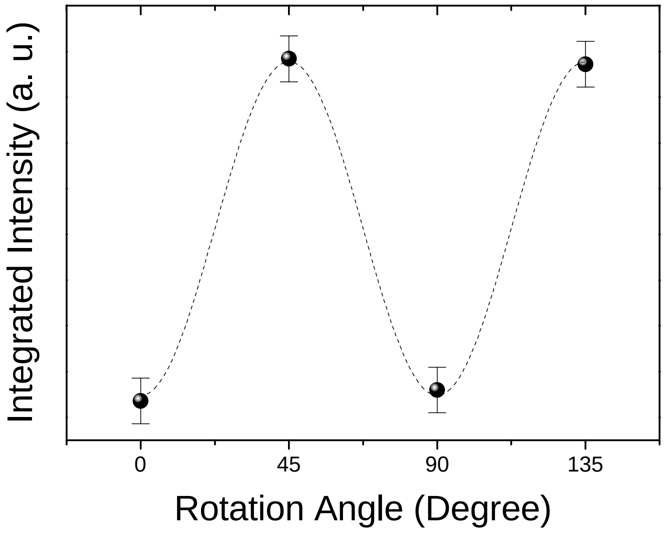

Figure 3.27. Experimental values of the angular intensity dependence of the *depolarized* O(2,3)-B_{1g} mode and the corresponding best fit function (dotted line), according to equation (3.25)

The first attempts to evaluate the uniformity of the degree of in-plane texture using the simplified model just described are presented in figure 3.28 for the PLD-IBAD sample named G3. These results confirm that the in-plane texture of this particular sample is uniform, within our experimental accuracy, over large regions of the YBCO conductor.

In view of these results, we conclude that micro-Raman scattering is a powerful technique to evaluate the uniformity of the *c*-axis grain fraction and *in-plane* texture of

CC, and hence of the uniformity of the critical current which we have demonstrated to be directly related to the degree of *in-plane* texture. Moreover, we have shown that a simplified modification of the model and the experimental procedure presented in this section enables to tackle the local evaluation of the uniaxial texture and film uniformity with a reasonable time investment.

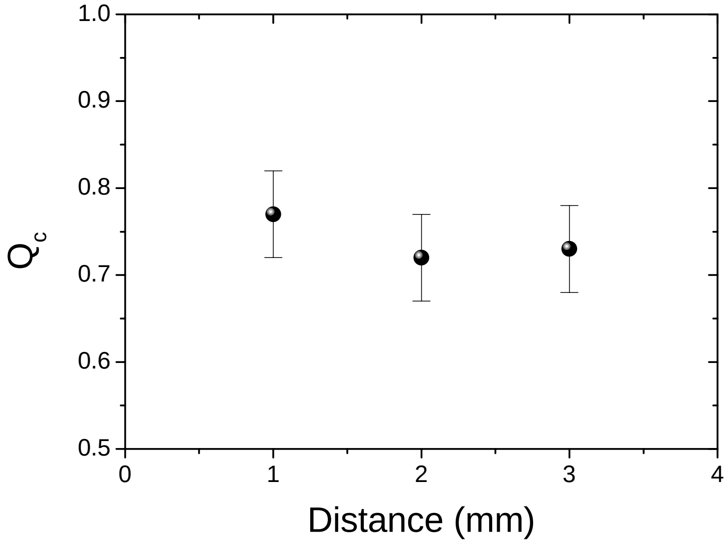

Figure 3.28. *In-plane* texture parameter, Q_c, of PLD-IBAD sample G3 evaluated in three different points with a 10 μm laser spot.

Conclusions

We have demonstrated the high potentiality of micro-Raman spectroscopy for non-destructive biaxial texture analysis of YBCO films and CC. A new and simple methodology has been developed adapted to CC based on the specific Raman selection rules for YBCO and polarized Raman scattering experiments. Detailed information on the epitaxial quality of the superconducting films is obtained from two parameters: *c*-axis oriented grains fraction, δ, and the degree of the *in-plane* orientation of the *c*-crystals, Q_c. Micro-Raman spectroscopy is a very suitable technique to determine the surface uniformity and homogeneity of the uniaxial texture of films, to identify the appearance of *a*-crystals even in large *c*-crystal fraction samples and to estimate their size and distribution. We have theoretically modeled the Raman scattering intensities using different grain misorientation distribution functions and defining the Q_c parameter accordingly. The analysis of several samples with different *in-plane* orientation has proved that YBCO CC are governed by a Lorentz grain orientation distribution function. We have confirmed, therefore, that Q_c is a true parameter to extract the degree of in-plane texture and grain misorientation distribution of YBCO CC. The feasibility and uniqueness possibility of micro-Raman to study the biaxial texture sample uniformity has been demonstrated for CC and a simplification of the model developed has been presented in this case.

Chapter 4

Characterization of YBCO TFA-MOD Films by micro-Raman

This chapter is divided in two parts, in the former we will describe the YBCO TFA-MOD process in more detail than as we saw in section 1.3.3.3, because in the forthcoming chapters of this thesis we will focus on the study, analysis and characterization of TFA grown films; whilst in the latter, we will show, with specific results obtained in this thesis, the high potential of micro-Raman spectroscopy for the characterization of YBCO TFA-MOD films. Emphasis on the application of the Raman scattering analysis of TFA films in aspects like orientation, uniformity, secondary phases, impurities, oxygen content and defects will be done.

A. YBCO TFA-MOD Process

Nowadays, a variety of solution-based processes have been developed for the preparation of YBCO films. Most of the techniques are based on the deposition of metal precursors prepared from alkoxides, acetates, naphthenates, carbonates, hydroxides, and so on[4.1-4.9]. All of the techniques have a common step that requires pyrolysis of the organic components prior to formation of YBCO from metal oxide phases. In general, the copper and yttrium compounds are easily converted to the respective oxides; however barium compounds tend to form stable carbonates, necessitating extreme high temperature processing conditions for the formation of YBCO and generally resulting in significant degradation of the superconducting properties of the final YBCO film[1.31].

In order to avoid the formation of $BaCO_3$, an alternative solution process based on metal trifluoroacetates was developed by Gupta *et al*[4.10]. In this approach, the more thermodynamically stable BaF_2 phase is formed during the pyrolysis process:

$$Ba(O_2CCF_3)_2 \rightarrow BaF_2 + (2CO_2 + C_2F_4) \tag{4.1}$$

The BaF_2 phase is subsequently converted to the barium oxide by reaction with H_2O at higher temperatures, as shown in the following equation:

$$BaF_2 + H_20 \rightarrow BaO + 2HF \tag{4.2}$$

In presence of Y_2O_3 and CuO oxides, the BaO reacts to form the YBCO superconducting phase.

4.1. The Trifluoroacetate Process

As we saw in chapter 1 (section 1.3.3.3.), the basic TFA process consists of four distinct steps: (1) precursor synthesis, (2) precursor coating, (3) pyrolysis of organic matter, and (4) YBCO nucleation and growth. Although these are separate processes, each step is dependent on the preceding steps in order to successfully fabricate a high-J_c YBCO film. Thus, due to that we have analyzed YBCO TFA-MOD films growth by micro-Raman spectroscopy to optimize the growth process, especifically in steps 3 and 4. We will describe the four steps more in detail below.

Step 1: Precursor Synthesis

The original TFA process used a precursor prepared by reacting a mixture of acetates of yttrium, barium, and copper in a 1:2:3 cation ratio in a 25% aqueous solution of trifluoroacetic acid at room temperature, following the chemical reaction as described in equation (4.3)[4.11]:

$$(Metal)^{n+}(acetate)_n + n(TFA\,acid) \rightarrow (Metal)^{n+} + (TFA)_n + n(acetate\,acid) \tag{4.3}$$

The mixture is continuously submitted to a reflux at 75 °C for 4 hours to improve the homogenization of the solution. The resulting solution is dried in air producing a blue glassy residue, which is redissolved in methanol[4.12,4.13] to make a solution of low viscosity and hence suitable for deposition on single crystal or metallic substrates (see figure 4.1). At ICMAB Inductively Coupled Plasma (ICP) analysis of these solutions has been used to determine the metal concentration. The use of solution precursors allows accurate control of composition and intimate mixing of the constituents.

An alternative route to the synthetic procedure based on acetate precursors has been also followed at ICMAB, which has as an advantage a higher simplicity and an improved control of the metallic stoichiometry[4.11]. In this case, ceramic YBCO oxide powder is directly used as starting precursor which is dissolved in trifluoroacetic acid and later evaporated and dried following a similar process to that described with acetate precursors (see figure 4.2). The reaction generated is described by:

$$\begin{aligned} & YBa_2Cu_3O_7 + 13\,(TFA\ acid) \rightarrow \\ & \rightarrow Y(TFA)_3 + 2Ba(TFA)_2 + 3Cu(TFA)_2 + \frac{13}{2}H_2O + \frac{1}{2}O_2 \end{aligned} \tag{4.4}$$

These two procedures have been widely used in the superconductivity group at ICMAB to grow YBCO films onto LAO single crystals and the microstructure and superconducting properties have been found to be indistinguishable. Actually, members of the superconductivity group are working on improvements of the synthesis focused on reducing the free acid and water content in the precursor solution.

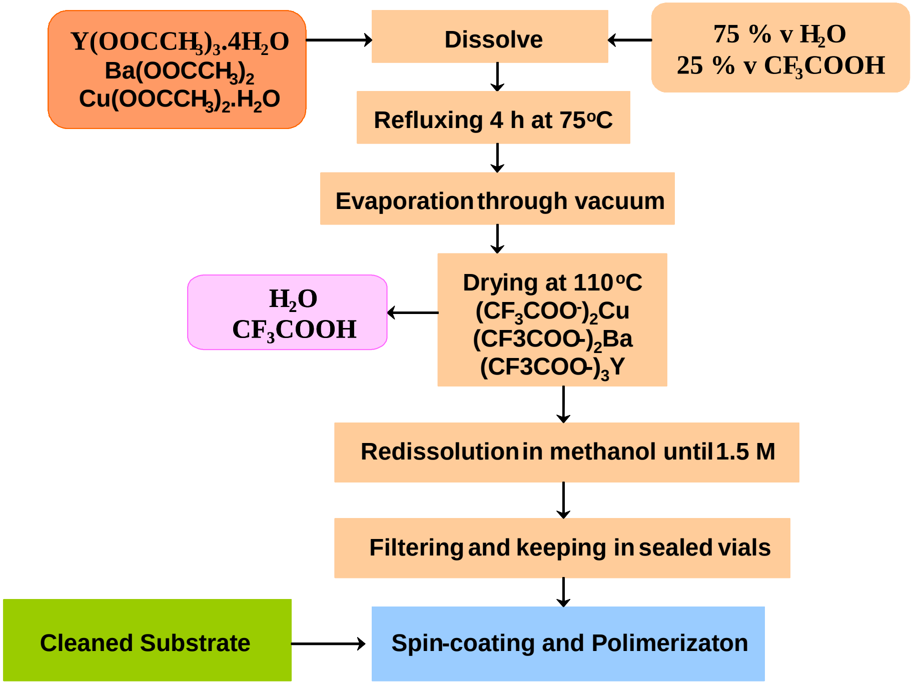

Figure 4.1.Schematic flow diagram of the procedure followed to prepare precursor using acetates as precursors. Metal trifluoroacetates are synthetized with metal acetates and trifluoroacetic acid in water.

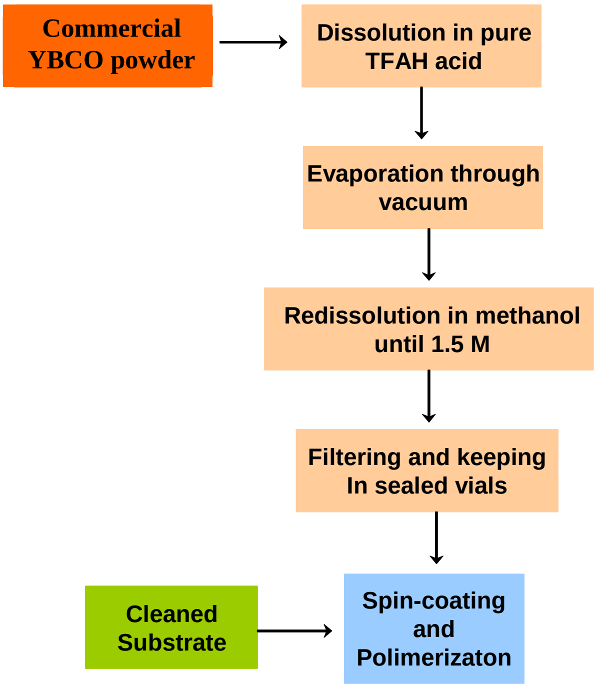

Figure 4.2. Schematic flow diagram of the procedure followed to prepare trifluoroacetate precursor solution using YBCO oxide powder as precursor.

Step 2: Precursor Coating

Deposition of the TFA precursor onto single crystal (or flexible) substrates can be carried out by a variety of coating techniques commonly used for industrial film-coating processes. Processes currently under development include dip and slot die coating[4.14]. In our case, the TFA solution precursor is deposited onto square (typically 5mm x 5mm area), (001) oriented $LaAlO_3$ (LAO) single crystal substrates by spin coating technique. This is a very convenient technique for the laboratory scale production of YBCO TFA-MOD films, because a very small volume of solution is used and an accurate control of the film thickness can be achieved by controlling the precursor viscosity, spinning rate and spinning acceleration. The solution was spinned at room temperature at angular speeds up to 6000 rpm and constant acceleration 2500 rpm-s^{-1}. The final film thicknesses were modified by adjusting the concentration of the mixed-metal precursor solution and were in the range of 300–400 nm for 1.5 M concentration solution, as determined by transverse SEM observations, profilometer and optical interferometric methods.

For coating long length conductors or large area films at industrial scale, dip coating technique is very suitable to minimize the use of solution and where even both faces can be coated simultaneously. Thus dip coating appears very convenient for large scale production of coated conductors.

Step 3: Pyrolysis of Organic Material

Precursor pyrolysis involves the thermal decomposition of the metalorganic salts and removal of the organic constituents of the precursor, leaving behind a mixture of nominally copper oxide, yttrium oxide, and barium fluoride. Even though the detailed decomposition reaction is still not well established, a tentative picture is[4.9,4.15]:

$$\begin{aligned} &Y(O_2CCF_3)_3 + 2Ba(O_2CCF_3)_2 + 3Cu(O_2CCF_3)_2 \rightarrow \\ &\rightarrow 0.5Y_2O_3 + 2BaF_2 + 3CuO + (nCO_2 + mC_xO_yF_z)\uparrow \end{aligned} \tag{4.5}$$

The process is carried out in a humid, oxidizing atmosphere at temperatures below 400 ^{o}C. Water vapour is added to the process atmosphere to suppress sublimation of the $Cu(O_2CCF_3)_2$ from the film, water molecules seem to stabilize $Cu(TFA)_2$ although this phenomenon has not been clearly described up to now. At ICMAB, to avoid any Cu loss during the pyrolysis, oxygen with a dew point of room temperature is injected into the furnace once the furnace temperature reaches 110 ^{o}C. The flow of humid oxygen was maintained until the temperature reaches 400 ^{o}C, at which point the furnace power and the flow of gas into the furnace are shut off. The furnace is then allowed to cool with the sample in stagnant humid oxygen. The water humidified gas is obtained by passing oxygen through de-ionized water contained in two flasks in series, prior to entering the furnace[4.11,4.13]. Oxygen is injected into the flasks at $P(O_2) = 1$ bar[4.11] and water pressure of $P(H_2O) = 24$ mbar[4.11].

The thermal decomposition of TFA precursor films results in a reduction in film thickness of the order of 50% and is accompanied by an increase of stress within the film. The standard TFA-based precursor is very susceptible to crack at decomposition temperatures corresponding to the increase in the stress versus temperature as shown in figure 4.3a. In order to mitigate cracking in the precursor film (figure 4.3b), it is necessary that the heating ramp after 200 ^{o}C is very slow ~ 3 ^{o}C/h, the original temperature–time profile developed for the decomposition required nearly 20 hours[4.11,4.13], as illustrated in figure 4.4.

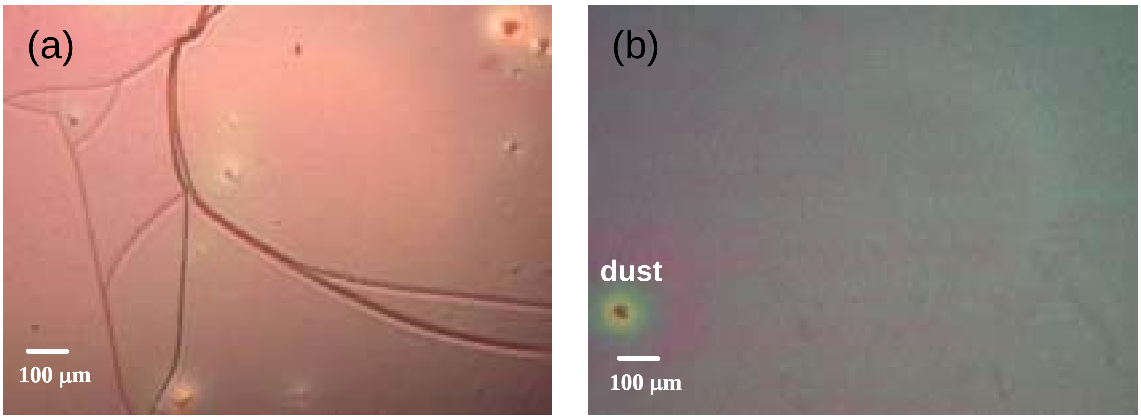

Figure 4.3. Optical micrographs of decomposed trifluoroacetates precursor films showing (a) the formation of cracks resulting from excessive stress during the thermal decomposition and (b) a defect-free film.

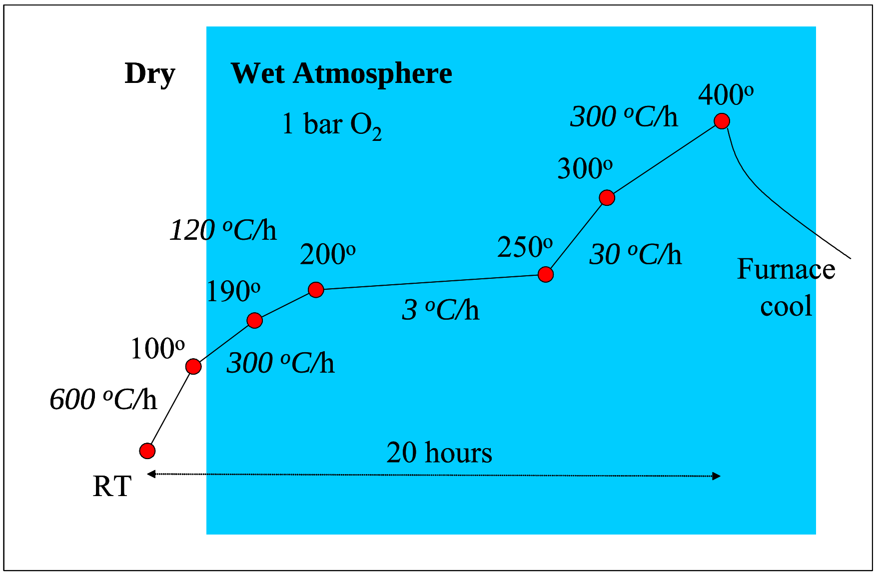

Figure 4.4. Typical pyrolysis profile for TFA-MOD method[4.13]. Humidified gas is introduced at 110 °C. All metal trifluoroacetates are decomposed at 200–300 °C to become CuO, BaF_2 and Y_2O_3 nanocrystallites in a homogeneous mixture with minimal segregation or coarsening of individual phases.

Approaches to shorten the decomposition time have generally focused on reducing the stress by modifying the chemistry of the starting precursors. Dawley[4.16] has shown that the addition of amines such as diethanolamine to the precursor allows a significant reduction in the decomposition time. ISTEC (Japan) has modified the full content of fluor by replacing $Cu(O_2CCF_3)_2$ by a Cu-free precursor and have succeeded in reducing the pyrolysis process down to two hours. At ICMAB lately, we have been able to shorten the pyrolysis process down to 2.5 hours by proper determination of the temperature region where stress is released and optimising the heating rate conditions.

Step 4: YBCO Nucleation and Growth

The CuO, BaF_2 and Y_2O_3 nanocrystallites that result from decomposition of the metal trifluoroacetates, are clearly evidenced in the XRD pattern displayed in figure 4.5. The nanocrystalline phases, have to subsequently be converted to the $YBa_2Cu_3O_{7-\delta}$ phase by annealing in humid nitrogen/oxygen gas mixtures at temperatures greater than 700 °C. The reaction process occurs according to the following nominal equation[4.17]:

$$0.5Y_2O_3 + 2BaF_2 + CuO + 2H_2O \xrightarrow{O_2} YBa_2Cu_3O_{7-\delta} + 4HF(g) \qquad (4.6)$$

Other authors, Smith *et al*[1.28] have proposed the presence of intermediate phases with the reaction represented by:

$$2BaF_2 + 2CuO + 0.5Y_2Cu_2O_5 + 2H_2O \xrightarrow{O_2} YBa_2Cu_3O_{6.5} + 4HF(g) \qquad (4.7)$$

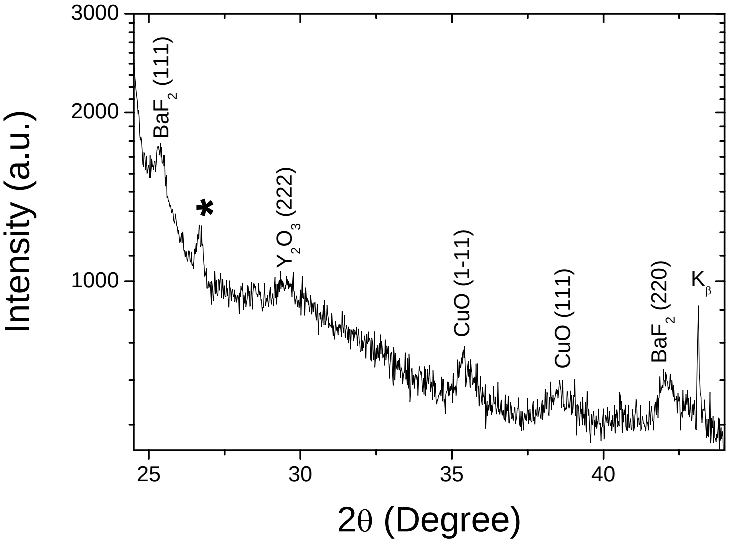

Figure 4.5. Logarithmic XRD pattern, measured during 12 hours, of a TFA film after the pyrolysis step. The CuO, BaF_2 and Y_2O_3 nanocrystalline phases resulted from the decomposition of the metal trifluoroacetates The curved background is due to the presence of the (*100*) LAO profile tail at ~ 23° degree. The reflection profile at ~ 26° degree (asterisk) will be explained later in chapter 6.

The heat treatment[4.11,4.13], as shown in figure 4.6, consist of heating to the annealing temperature at a ramp rate of 1500 °C/h, from room temperature up to 750 – 800 °C; then the precursor film is kept at the same high temperature for about 180 minutes to obtain the $YBa_2Cu_3O_{6.5}$ tetragonal phase and then cooled down at 150 °C/h to 450 °C for film oxygenation, thus we transform the tetragonal to YBCO orthorhombic superconducting phase, and subsequent slow cooling to room temperature is done at 300 °C/h. The humid gas flow is initiated at the furnace temperature of 110 °C to avoid water condensation on the film, and water vapour is introduced into the furnace by bubbling the incoming gas through an attached reservoir of de-ionized water like in the pyrolysis process (figure 4.7).

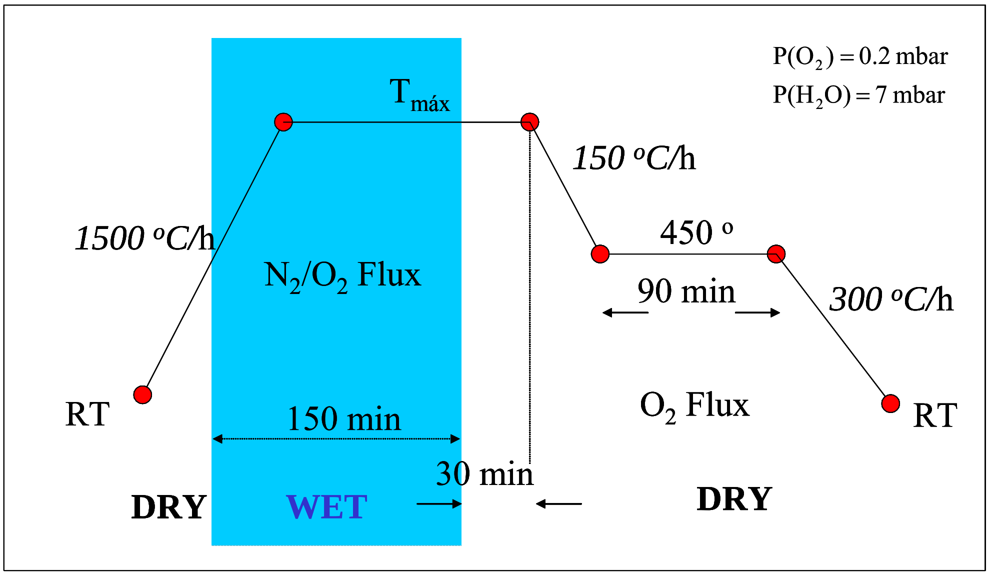

Figure 4.6. Typical firing profile[4.11] for the TFA-MOD process used at the ICMAB superconductivity group. Humidified gas is introduced at 110 °C to avoid water condensation on the film. The maximum temperature was between 750 – 800 °C.

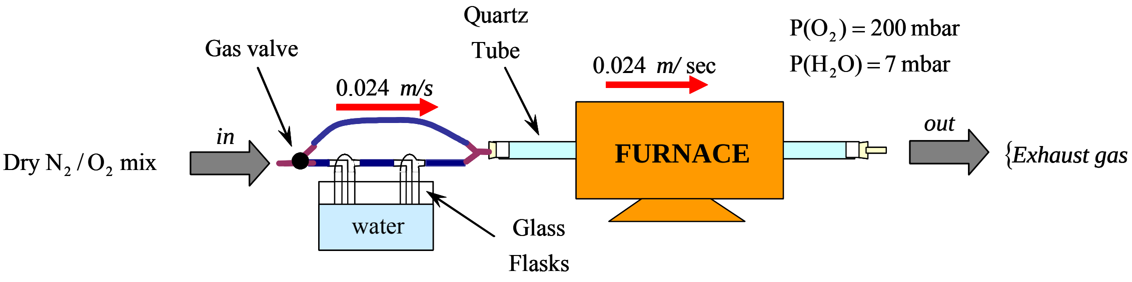

Figure 4.7. Scheme of experimental set-up[4.11] for the YBCO superconducting film preparation by the TFA-MOD process.

Low $P(O_2)$ = 0.2 mbar furnace atmospheres for the high temperature treatments were prepared using mass flow controllers to mix nitrogen/oxygen gas. The total flow rate of gas through the furnace was kept at 0.024 m/s. The oxygen partial pressure in the furnace was altered by changing the relatives flow rates of nitrogen[4.11].

The conversion of the precursor phases to the YBCO results in a further reduction in film thickness of 50% approximately, as schematically shown in figure 4.8. The initial step is the reaction of BaF_2 in the precursor film with H_2O, which requires the transport of H_2O vapour into the film and removal of the resulting HF product. As the BaF_2 reacts, the YBCO phase nucleates at the substrate interface and continues to grow through the film thickness, as schematically illustrated in figure 4.8. Precise control of the reaction rate is required to promote the epitaxial nucleation of YBCO on the substrate surface and subsequent growth of the highly textured YBCO through the thickness of the film.

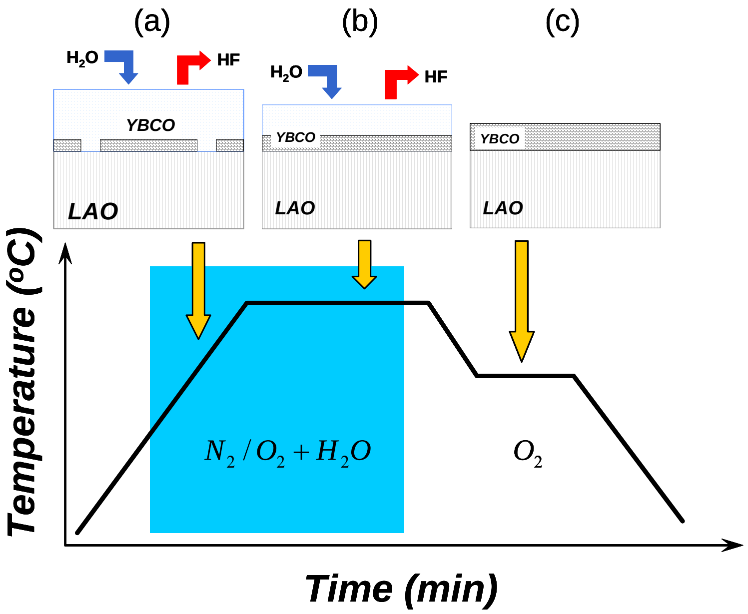

Figure 4.8. Illustration and corresponding drawing of the nucleation and growth of the YBCO phase from a trifluoroacetates precursor film as a function of processing temperature and atmosphere.

The pre-existent knowledge of this conversion process is summarized below. In chapter 6, we will present our latest results which will extend this pre-existent knowledge. As it is observed in the XRD pattern of precursor film after the pyrolysis step (figure 4.5), the starting decomposed precursor consists of BaF_2, CuO, and Y_2O_3 nanocrystalline phases; it is a homogeneous mixture with minimal segregation or coarsening of individual phases. However, precursor films decomposed at low temperatures can have high fluoride contents, suggesting the formation of yttrium fluoride species[4.18]. As the temperature increases, $Y_2Cu_2O_5$ begins to form, although with minimal segregation or coarsening of individual phases. As the film approaches the hold temperature (~750–800°C), the YBCO begins to nucleate at the substrate/precursor interface (as we shall see in chapter 6 when we will show our results on quenched films). Depending on the experimental conditions such as total pressure, $P(H_2O)$, $P(O_2)$, flux flow rate (V_g) and temperature, the growth rate, R, can be varied in a very extend range:

0.04nm/s<*R*<6nm/s. The YBCO continues to grow through the thickness of the precursor as the film is held at the growth temperature.

A theoretical analysis of YBCO growth proposed by Honjo *et al*[4.19] to estimate the growth rate of the YBCO phase in order to optimize the annealing time under various conditions was used to study the relation between the gas flow vector of water pressure and the HF gas, as we will show in chapter 5. Figure 4.9 shows the fundamental image of their model. They consider a one-dimensional analysis for the mass transfer of H_2O and HF gases. It can be imagined that the precursor film is surrounded by a stagnant gas boundary layer through which H_2O diffuses and arrives at the precursor surface (H_2O mass transfer through porous layer). They assume that the conversion reaction (equation 4.6) only occurs at the YBCO growing interface (interface kinetics) and the produced HF (equation 4.2) diffuses back out through the precursor film and gas boundary layer to the main gas stream (HF mass transfer through a gas).

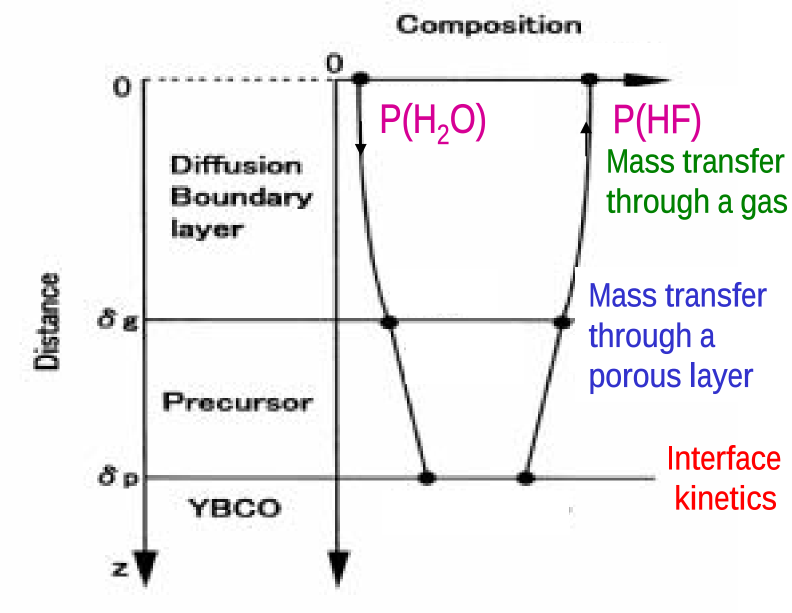

Figure 4.9. Fundamental image of Honjo *et al* YBCO growth model[4.19], where δ_p is the effective precursor film thickness, δ_g is the gas boundary layer thickness. H_2O gas diffuses and arrives at the precursor surface, conversion reaction of BaF_2, CuO and Y_2O_3 nanocrystallites only occurs at the YBCO growing interface (interface kinetics) and the produced HF diffuses back out through the precursor film and gas boundary layer to the main gas stream.

They have got an expression for the local rate of conversion from H_2O to HF, given by:

$$R = K \frac{\sqrt{V_g}\sqrt{P(H_2O)}}{P_{Total}^{1/6}} \exp\left[-(a/T)\right] \tag{4.8}$$

where K is a constant, T is the temperature, V_g is the gas flow rate, P_{Total} is the total pressure and $P(H_2O)$ is the water pressure. We have observed that the more important part in this process is the diffusion boundary layer in agreement with this model, as we will show in chapter 5 varying the $P(H_2O)$.

B. Raman Scattering Analysis of YBCO TFA-MOD films

Raman spectroscopy has become a very useful and powerful tool to characterize YBCO films, as we saw in chapter 3. This non-destructive technique can be also applied to the analysis of YBCO TFA-MOD films. As we mentioned in section 1.6.3, the phonons of YBCO are five, but in our work frequency range (200 – 600 cm^{-1}) we may observe only three peaks: the O(2,3), +O(2,3) and O(4) modes, as shown in figure 4.10. In practise we are interested only in two phonon peaks, the O(2,3)-B_{1g} (red line) and O(4)-A_g (blue line), for the characterization of YBCO TFA-MOD films grown onto single crystal substrates in order to optimized the YBCO growth process. In this chapter we emphasize aspects related to orientation, uniformity, secondary phases, grain size, impurities, defects and oxygen content in YBCO TFA-MOD films. All these items shall be considered separately in the next sections.

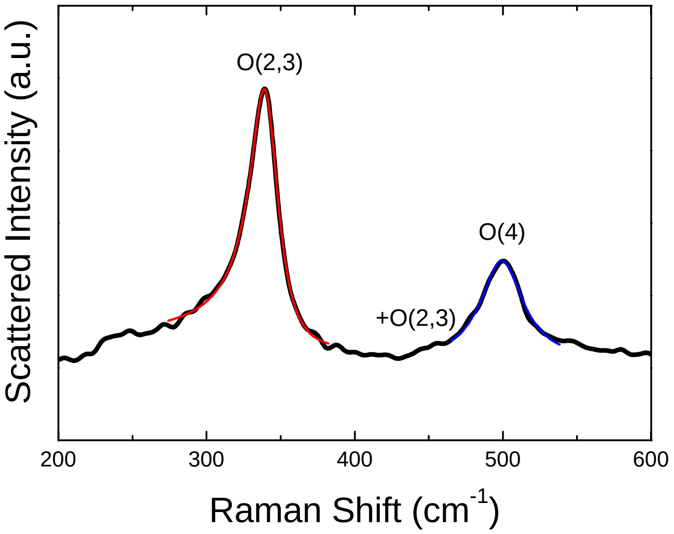

Figure 4.10. Two phonon peaks in the Raman spectrum have been used in the characterization of YBCO TFA-MOD films. The peak at 340 cm^{-1} (B_{1g}-like) associated with the *out-of-phase* vibration of the O(2,3) oxygen atoms in the CuO_2 planes (red line), and the peak at 500 cm^{-1}, an A_g mode involving the apical oxygen atoms O(4) vibrations (blue line).

4.2. *C*rystal Orientation

Due to the anisotropy of YBCO (section 1.2.4), the superconducting properties of YBCO films, such as the critical current density is also strongly anisotropic, $J_c^{ab} >> J_c^{c}$ and therefore an epitaxial film with the c-axis perpendicular to the substrate has to be grown to reach critical currents densities higher than 1MA/cm^2 at 77K. Raman scattering provides information on the crystal orientation of the YBCO grains with regard to the substrate surface. It can easily be gained from polarization-dependent measurements, because phonon symmetries involved are known and Raman intensity described in equation (1.12) is sensitive to the polarization of the incident light with regard to crystallographic axis of YBCO grains, as we showed in chapter 3.

In particular, in figure 4.11 we show two Raman spectra of two TFA samples with different uniaxial orientation. In the first sample (figure 4.11a), we show the results for an almost *c*-axis oriented film, with the scattering configuration $\mathbf{e}_i // \mathbf{e}_s // c - axis$ (*polarized*). We can observe that the phonon mode at 340 cm^{-1} is much stronger than the mode at 500 cm^{-1}. According to equation (3.5) we can calculate the value of the *c*-axis grain fraction, $\delta = 0.90$. In the second sample (figure 4.11b), an almost *a*-axis oriented film is analyzed, with the scattering configuration $\mathbf{e}_i // \mathbf{e}_s // a, b - axis$ (*polarized*). In this latter case, we can observe that the mode at 340 cm^{-1} has become much weaker than the strong mode at 500 cm^{-1} ($\delta = 0.20$). Thus, from the relationship between these two Raman modes one can determine the uniaxial film orientation and the *c*-axis fraction value by using the equation (3.5).

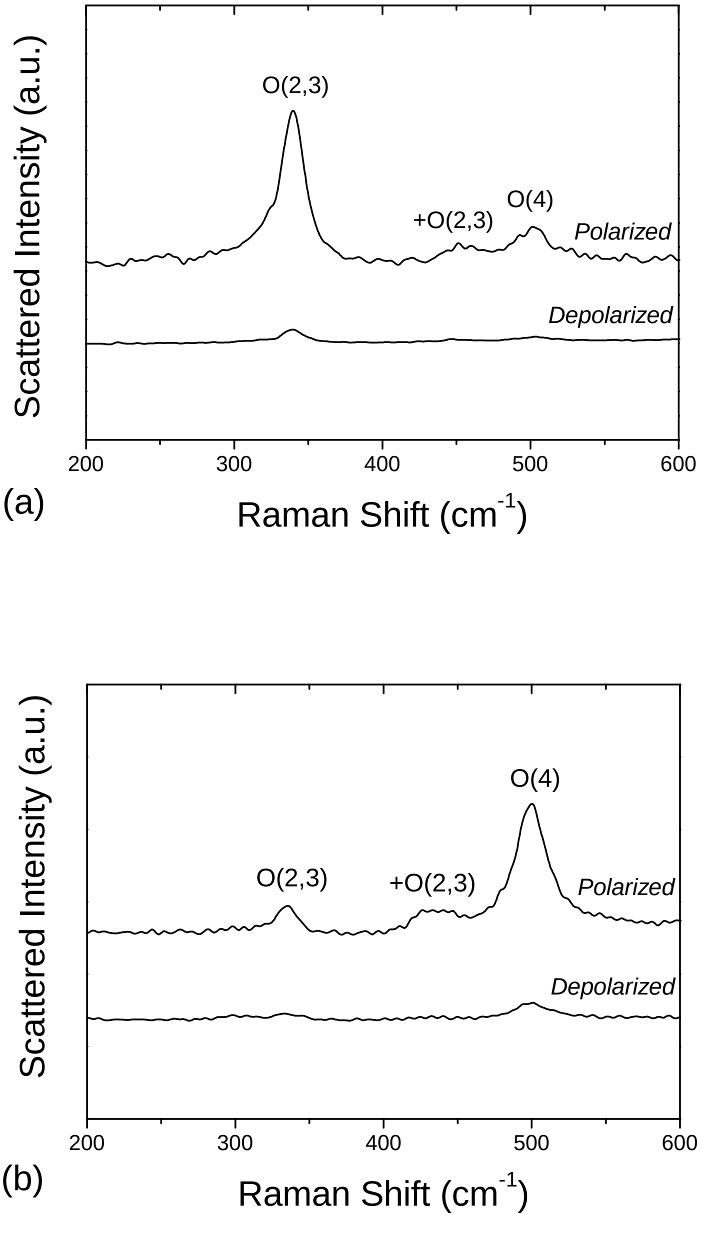

Figure 4.11. Raman spectra of two YBCO TFA-MOD films: (a) an almost *c*-axis oriented film (*c*-axis perpendicular to substrate surface), $\delta \sim 0.90$ and (b) an almost *a*-axis oriented film (*c*-axis parallel to the substrate surface), $\delta \sim 0.20$.

In addition, Raman scattering can supply information on the *in-plane* orientation as shown in section 3.2. According to the model described in chapter 3, changing the angle between the crystallographic axes of the film and the polarization direction of the incident laser light produces intensity modulation of the O(2,3)-B_{1g} and O(4)-A_g modes in *polarized* and *depolarized* geometries, with a modulation period of 90°. In particular, one can determine the matching *in-plane* orientation between the YBCO film and the underneath substrate. It is known that different types of substrate support different *a/b*-orientations of the YBCO grains[4.20] due to different lattice matching between the substrates and YBCO.

Figure 4.12 shows the Raman spectra of a YBCO film grown on an LAO single crystal, recorded in the *polarized* and *depolarized* scattering configurations for two different values of the angle φ namely 0° and 45°. Remember that φ is defined as the angle between the polarization direction of the laser light and the edge of the sample. We see that in figure 4.12(a) φ = 0°, the polarized spectrum is much stronger than the depolarized one. The reverse is true for figure 4.12(b), φ = 45°. From the intensity oscillations displayed in figure 3.23 we can deduce that the spectra of figure 4.12 are for YBCO grains with crystalline *a*-axis lying in the substrate plane and parallel to the (100) direction of the substrate, denoted as $[100]_{YBCO} \| [100]_{LAO}$.

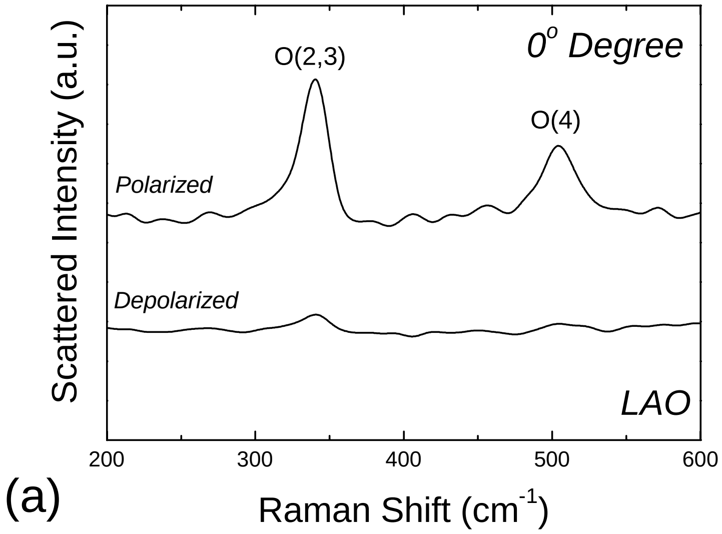

Figure 4.12. (a)

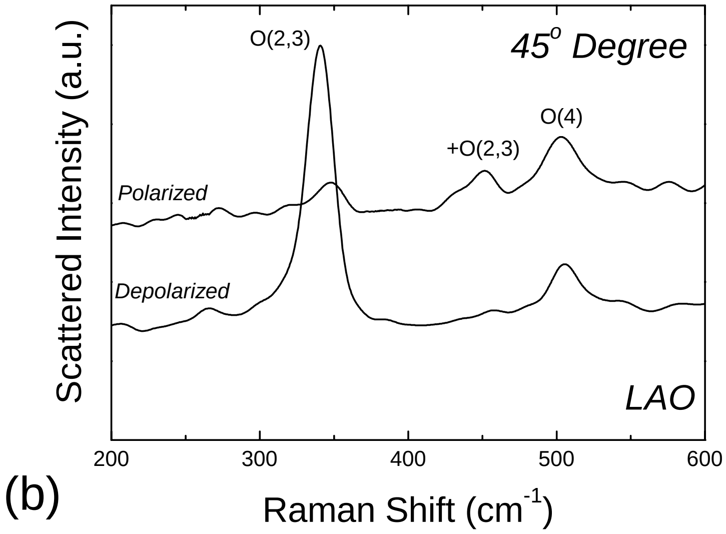

Figure 4.12 Raman spectra for φ = 0° (a) and φ = 45° (b) of a TFA-MOD YBCO film on a LAO single crystal in the *polarized* and *depolarized* scattering geometries. The relative Raman intensities correspond to YBCO grains whose crystalline axes are along the [*100*] direction of substrate, $[100]_{YBCO}\|[100]_{LAO}$.

Figure 4.13 shows the polarized and depolarized Raman spectra of a YBCO film grown on a CeO_2 buffer layer on top of a YSZ single crystal for φ = 0° and φ = 45°. Figure 4.13(a) shows higher intensity for the depolarized configuration, and the spectra of figure 4.13(b), φ = 45° show a higher Raman intensity for the polarized scattering. According to figure 3.23 the spectra of figure 4.13 correspond to YBCO grains with the crystalline *a*-axis in the plane of the substrate and oriented at 45° respect to the substrate edge of YSZ, i.e. the crystalline a-axis of the grains are along the (110) direction of the substrate, and are denoted as $[100]_{YBCO}\|[110]_{YSZ}$.

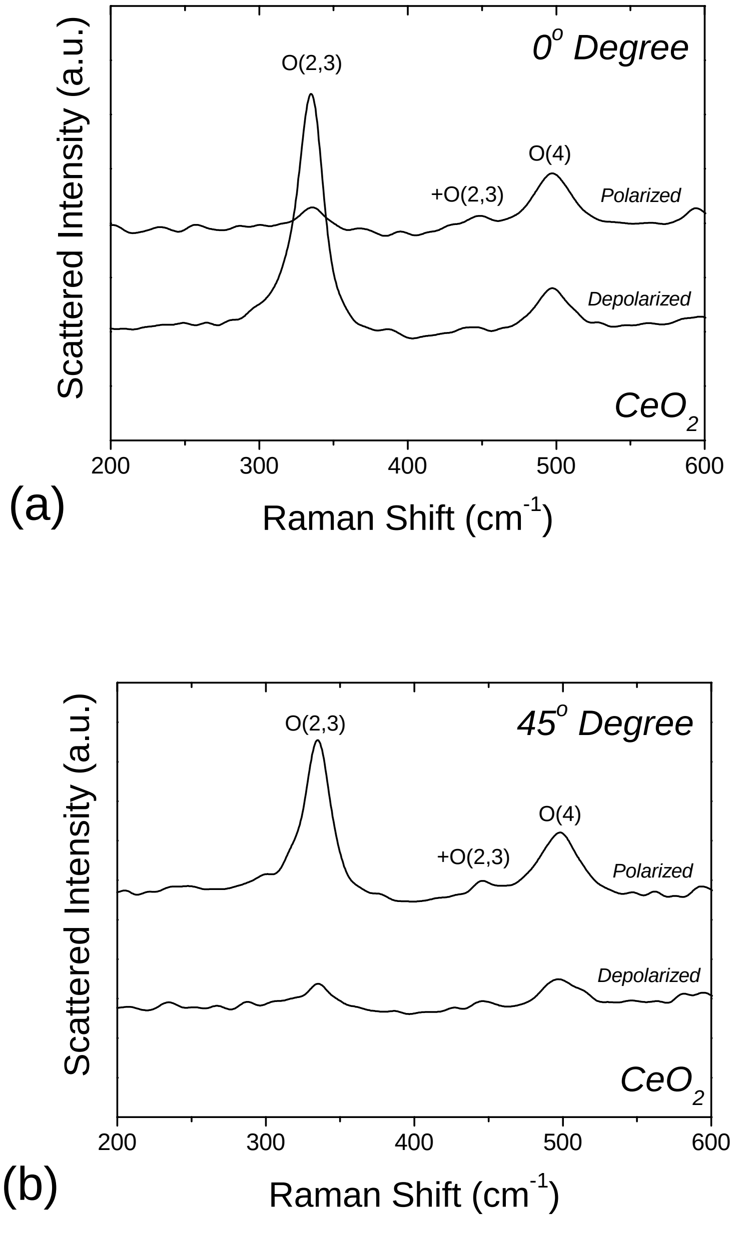

Figure 4.13 Raman spectra for φ = 0° (a) and φ = 45° (b) of a TFA-MOD YBCO film on a CeO_2 buffer layer on top of a YSZ single crystal in the *polarized* and *depolarized* scattering geometries. The relative Raman intensities correspond to YBCO grains whose crystalline axes are along the [*110*] direction of substrate, $[100]_{YBCO} \| [110]_{YSZ}$.

In particular, we present two YBCO films grow onto (a) LAO single crystal and (b) CeO_2 buffer layer grown on a YSZ single crystal. With micro-Raman spectroscopy we have determined the different YBCO *in-plane* matching orientations between YBCO and the underneath layer. Keep in mind that the substrate *a*-axis [*100*] can be aligned with the microscope axis, as we showed in the *in-plane* orientation analysis presented in chapter 3. Hence, from Raman polarization-dependent measurements and rotating the angle between the crystallographic axes of the film crystals and the polarization direction of the incident laser we may account with the actual crystallographic orientation of the YBCO *a*-axis with respect to the substrate. The scattered intensity for O(2,3) and O(4) modes in *polarized* and *depolarized* geometries change from 0° to 45° degree as shown in figures 4.12 and 4.13. We may concluded that YBCO *a*-axis grow parallel to LAO substrate, *i.e.* $[100]_{YBCO} // [100]_{LAO}$, mainly due to low lattice mismatch between the two cell parameters ($a_{YBCO} \approx 3.85$ Å and $a_{LAO} \approx 3.79$ Å), while YBCO *a*-axis grow at 45° degree from the CeO_2 *a*-axis, *i.e.* $[110]_{YBCO} // [100]_{CeO_2}$, due to good mismatch of $a_{YBCO} \approx \sqrt{2}\, a_{CeO_2}$ ($a_{YBCO} \approx 3.85$ Å and $a_{CeO_2} \approx 3.85$ Å), as shown clearly in figure 4.14.

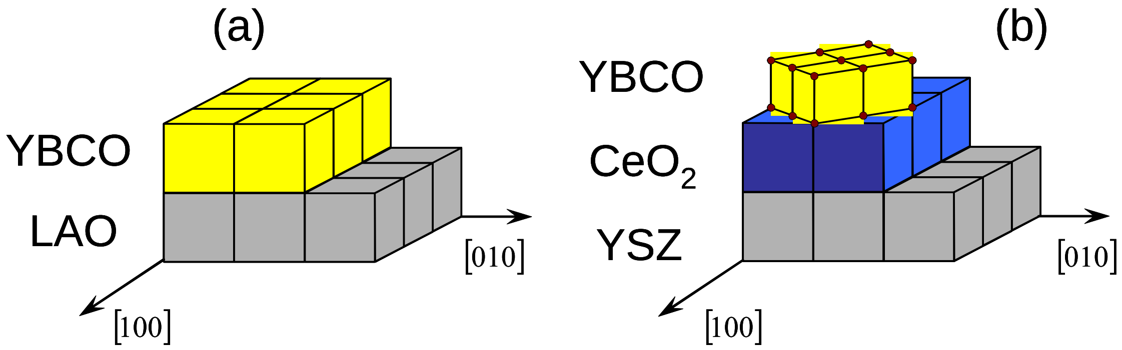

Figure 4.14. An illustration of YBCO growth with different *a*/*b*-orientations with regard to (a) LAO single crystal and, (b) CeO_2 buffer layer on YSZ single crystal.

4.2.1. *c*-axis Fraction. Local Uniformity

The achievement of a high degree of uniaxial texture is a prerequisite for high critical current YBCO films due to the large anisotropy factor[4.16]. The microscopic spatial resolution of our Raman system (~ 1 μm) allows us to analyze the local uniformity and local inhomogenities of YBCO TFA-MOD films. We have performed 1μm line scans to determine the local distribution and size of *c*- and *a*-axis grains, following the procedures of section 3.1.2.1 for BaF_2 process, PLD and CC samples.

We performed line scans in two YBCO samples grown onto LAO substrate at two different grow temperatures (700 and 790 °C) keeping the other growth parameters fixed ($P(H_2O)$, $P(O_2)$, gas flow, etc), the film thickness was 250 nm. Figure 4.15a shows the sample grown at 790 °C where a majority of *c*-axis grains are present. Instead figure 4.15b shows the results of the sample grown at 700 °C where *c*- and *a*-axis grain colonies are randomly distributed with submicron size (smaller than laser beam spot) In addition, some larger *a*-axis grains of 2-3 μm ($\delta \sim 0.2$) are observed as well as the δ values of ~ 0.4 are interpreted as potential *a*-axis colonies of smaller dimension ~ 0.5-1μm which our spatial resolution could neither resolve. This difference in the uniaxial texture determined by micro-Raman will be reflected in the critical current, J_c, values. Thus, the sample of figure 4.15a has a J_c.~ 3MAcm^{-2} while 4.15b a J_c.~ 0.6 KAcm^{-2}. Therefore, micro-Raman line scans help us to correlate the film microstructure with J_c. Hence, high synthesis temperature is favourable for *c*-axis grain growth to obtain high J_c.values, as we shall discuss in chapter 5.

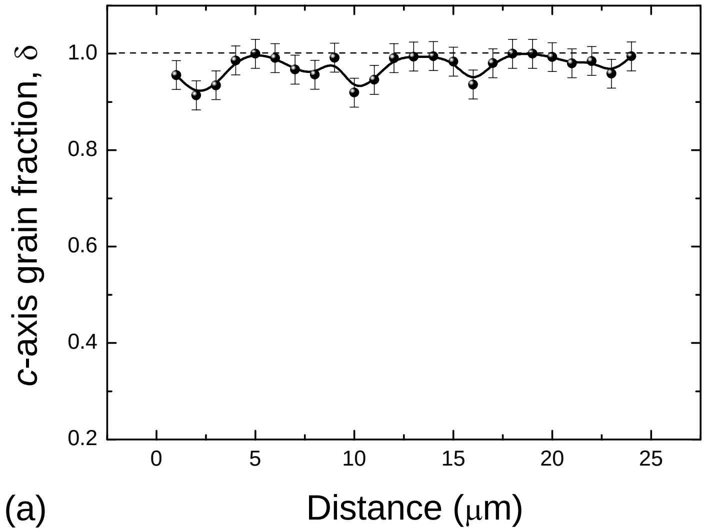

Figure 4.15. (a)

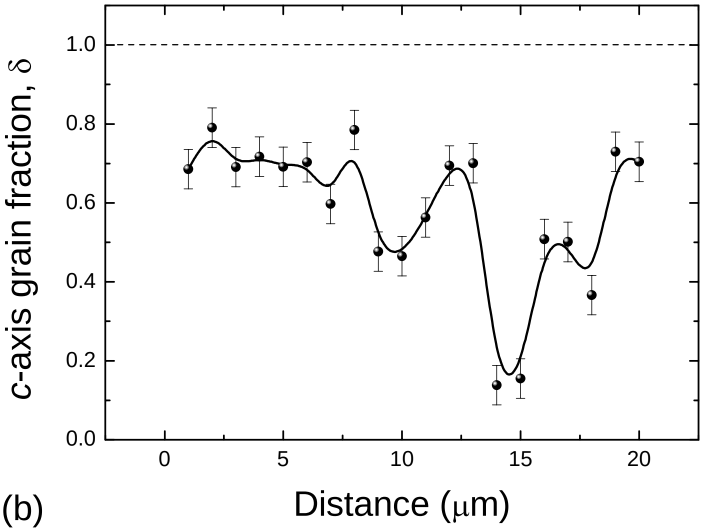

Figure 4.15. Line scans obtained from micro-Raman measurements of two YBCO TFA-MOD films with synthesis temperature at (a) 790 °C with J_c ~ 3.2 MAcm^{-2} and δ ~ 0.9, and (b) 700 °C with J_c ~ 0.6 KAcm^{-2} and δ ~ 0.6.

On the other hand, micro-Raman spectroscopy also allows us to obtain texture maps of YBCO TFA-MOD films by scanning (now laser spot ~10μm) twenty-five points on the film, in the shape of a 5x5 grid that covered most of the film surface (2mm x 2mm area). In particular, we show two TFA samples grown onto LAO and grown at different processing conditions such as growth temperature (575 and 790 °C) and water pressure (7 and 24 mbar). These samples showed different texture maps, as clearly illustrated in figure 4.16. Figure 4.16a shows the texture maps of an almost *c*-axis film as a function of position on the sample. This YBCO film has high *c*-axis oriented grains ($0.80<\delta<0.85$) homogeneously and uniformly distributed. This fact is correlate with SEM micrograph of its surface microstructure shown in figure 4.16b and a high J_c value ~ 3MAcm^{-2}. The second film, figure 4.16c shows the texture maps of an almost *a*-axis film ($0.20<\delta<0.30$) as a function of position on the sample. This YBCO film is an almost *a*-axis oriented film with *a*-grains uniformly distributed. This fact is correlated with SEM micrograph of its surface microstructure shown in figure 4.16d. We can observe a vast majority of needle-shape structure, which is a feature associated with *a*-axis YBCO grains, J_c value ~ 0.3MAcm^{-2}. As one could expect the microstructure of each film is sensitive to the processing conditions, as we shall discuss in chapters 5.

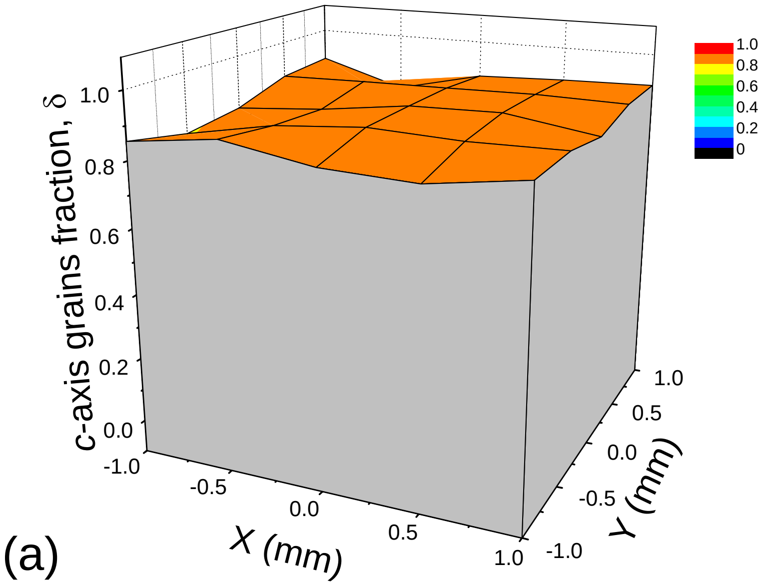

Figure 4.16. (a)

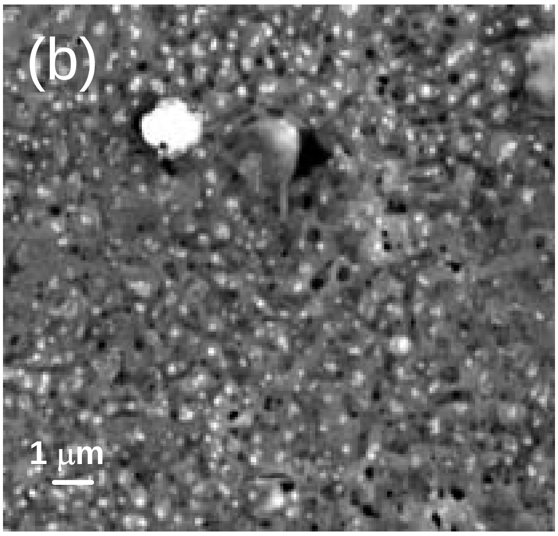

Figure 4.16 (b)

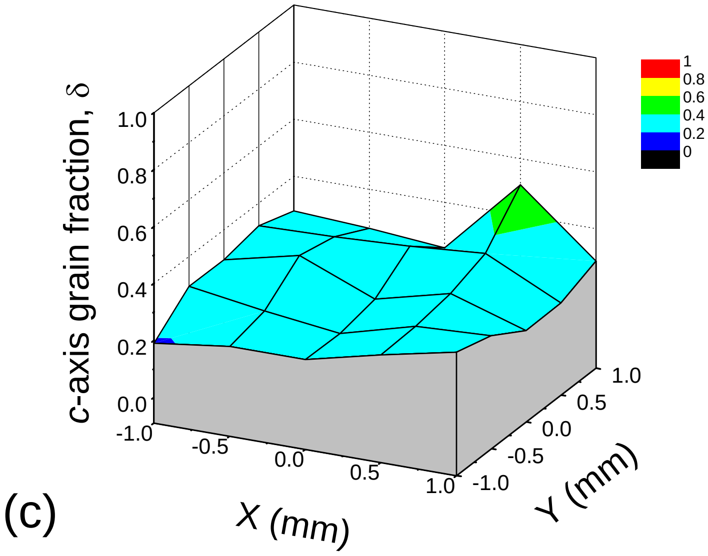

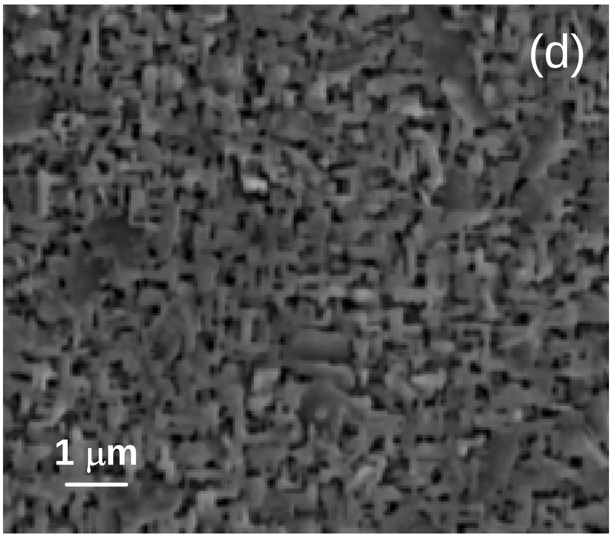

Figure 4.16. Texture maps and SEM micrographs of YBCO TFA-MOD samples with (a)-(b) high fraction of *c*-axis oriented grains, and (c)-(d) low fraction of *c*-axis oriented grains.

4.3. Secondary Phases and Impurities

On the way to grow single phase YBCO TFA-MOD samples, we have observed that small amounts of precursor material that did not react or impurities which were unintentionally grown appears on the films. We call secondary phases to precursor phases coming from non-fully reacted material such as: BaF_2, CuO, Y_2O_3 and $Y_2Cu_2O_5$ (precursor phases). Instead, we call impurities to those phases that unintentionally grow, such as: $BaCuO_2$ and Y_2BaCuO_5.

Raman spectroscopy shows again its enormous potential to identify traces of secondary phases and impurities coexisting with a major YBCO superconducting phase. Results are compared with XRD measurements. We illustrate this singular feature in two particular TFA films grown onto LAO substrate. Figure 4.17a-b show typical film XRD pattern and Raman spectra of a completely reacted YBCO TFA-MOD film. Both, the XRD and Raman scattering measurements have shown that the film is virtually a single phase due to no presence of other profiles than YBCO. In contrast, the Raman spectrum of the other film shows the presence of $BaCuO_2$ phase due to a clear phonon at ~ 630 cm^{-1}, as is indicated in figure 4.17d. Note that $BaCuO_2$ could not be readily detected by the conventional XRD technique[4.21], as shown in figure 4.17c. Thus, such impurity just as others, are often more readily detected by Raman scattering than XRD.

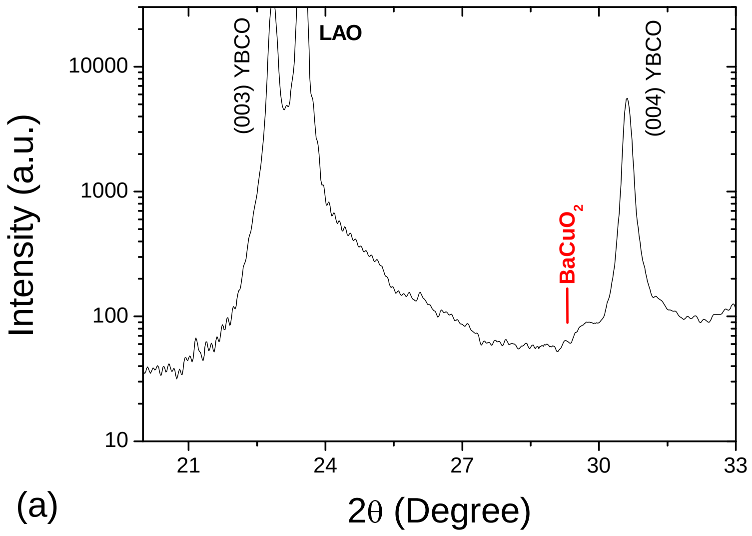

Figure 4.17. (a)

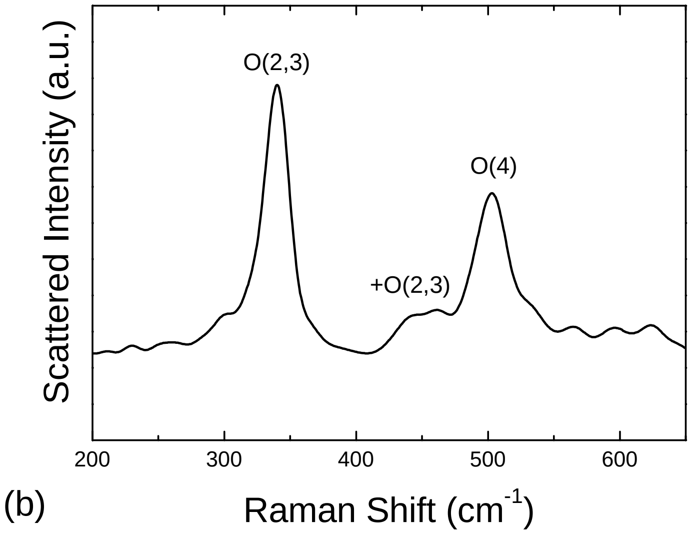

Figure 4.17(b)

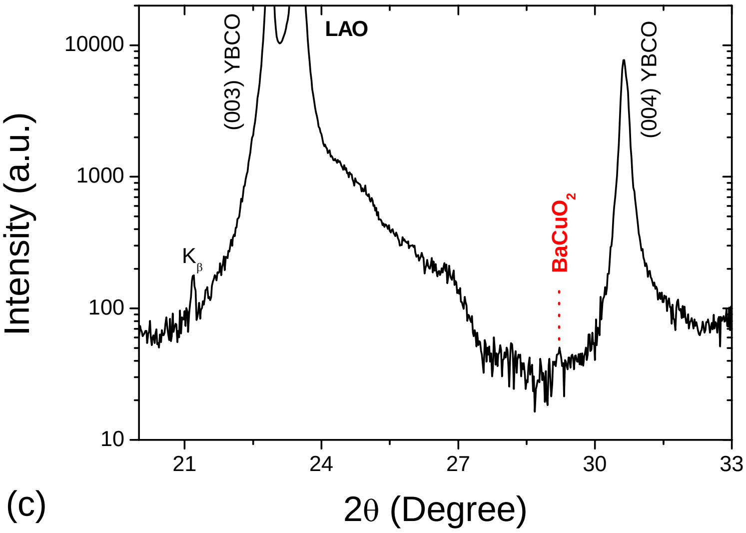

Figure 4.17(c)

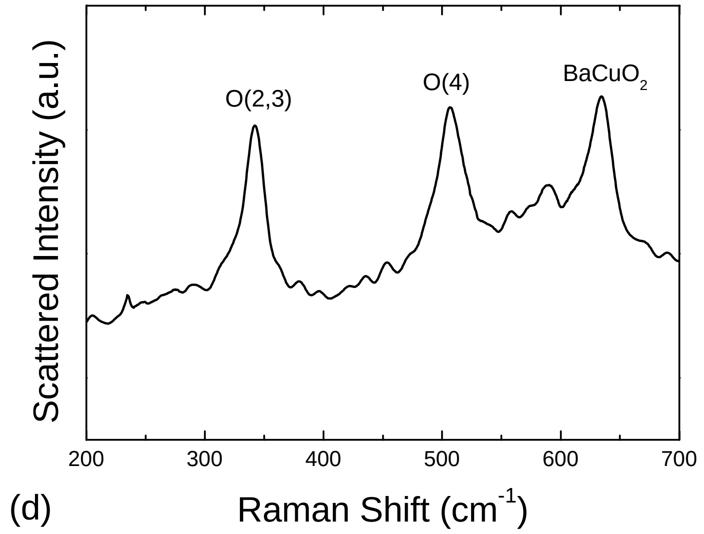

Figure 4.17. XRD and Raman spectra of (a) YBCO single phase film, and (b) YBCO film with presence of $BaCuO_2$ phase.

As the secondary phases and impurities are frequently insulating substances, they have much larger Raman signals within a particular illuminated spot and show up strongly in the spectra (high Raman scattering efficiency). Additionally, since secondary phases and impurities have in general different crystal symmetry, they also have different Raman tensor and phonon frequencies and therefore we can easily distinguish them from well defined YBCO phonons.

In order to show the difference in the Raman scattering efficiency among secondary phases and impurities, we have performed reference measurements in powder samples with constant measuring conditions (laser spot, power on sample, integration time, laser wavelength, etc). The Raman spectra of the most important precursor (intermediate) phases for YBCO TFA-MOD, are shown in figure 4.18. The Y_2O_3 compound has showed to have the stronger Raman scattering efficiency as compared with the other three ones, while the CuO compound has showed the weaker scattering efficiency. The impurity phases are observed in figure 4.19. Notice that the $BaCuO_2$ phase has also a very large Raman scattering efficiency. In Tables 4.1 and 4.2 the phonon frequencies of these compounds in the range of 200 – 700 cm^{-1} are shown. Hence, it is very easy to determine the secondary phases and impurities on YBCO TFA-MOD films by comparison of the Raman spectra of secondary (precursor) phases and impurities with the Raman spectra of real YBCO samples. It is clear, though, that phases or compounds which are not Raman active can not be detected. This is the case of the BaO phase[4.22] which in fact has been evidenced by TEM as a precursor phase, as we will show in chapter 6.

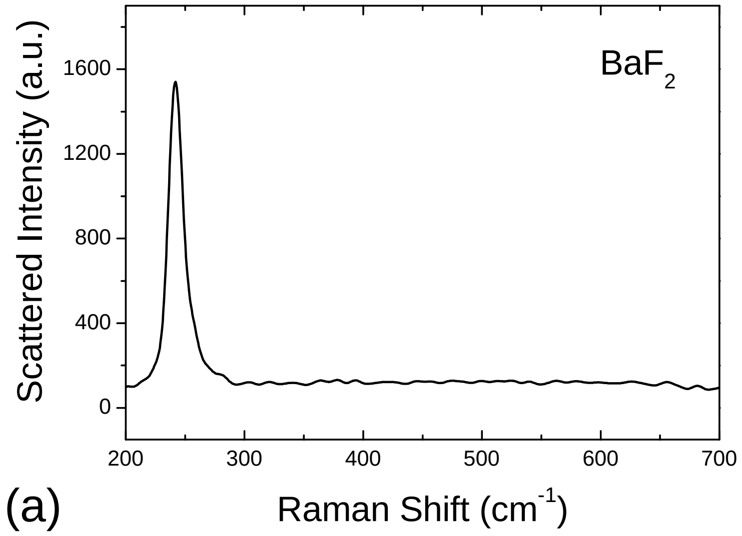

Figure 4.18. (a)

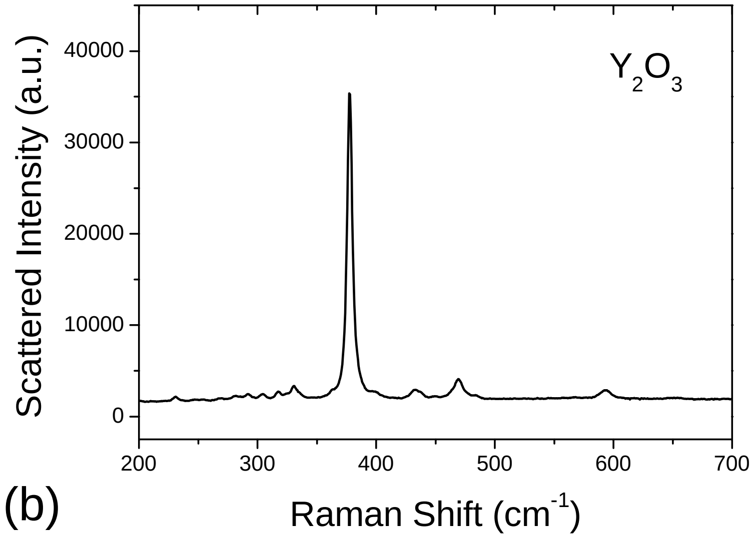
Scattered Intensity (a.u.)
40000
30000
20000
10000
0
200
300
400
500
600
700
Raman Shift (cm^{-1})
Y_2O_3
(b)

Figure 4.18. (b)

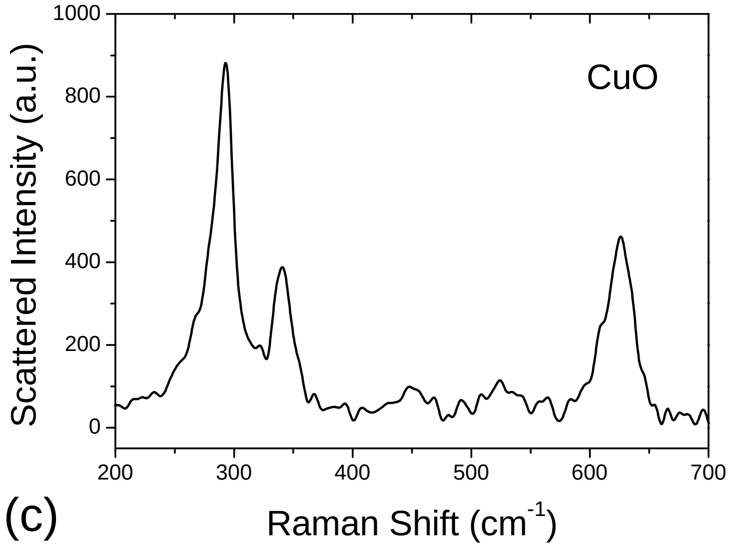
Scattered Intensity (a.u.)
1000
800
600
400
200
0
200
300
400
500
600
700
Raman Shift (cm^{-1})
CuO
(c)

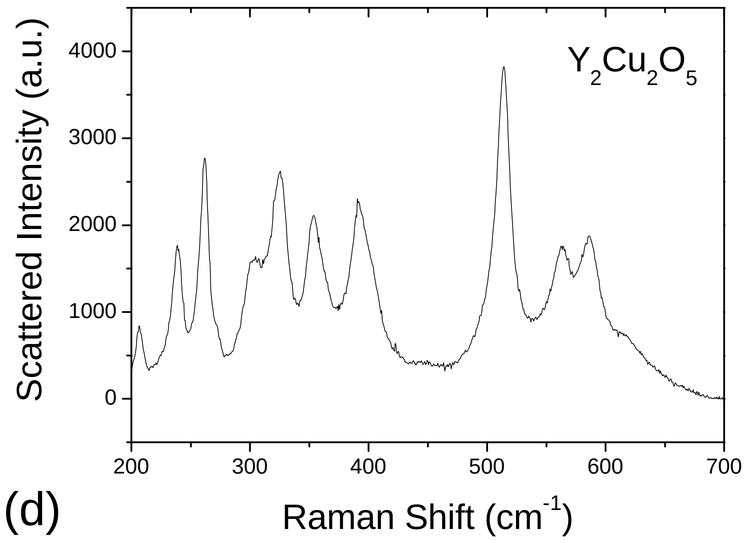

Figure 4.18. Raman spectra of main secondary (intermediate) phases of TFA samples in powder form (a) BaF_2 (b) Y_2O_3 (c) CuO and (d) $Y_2Cu_2O_5$.

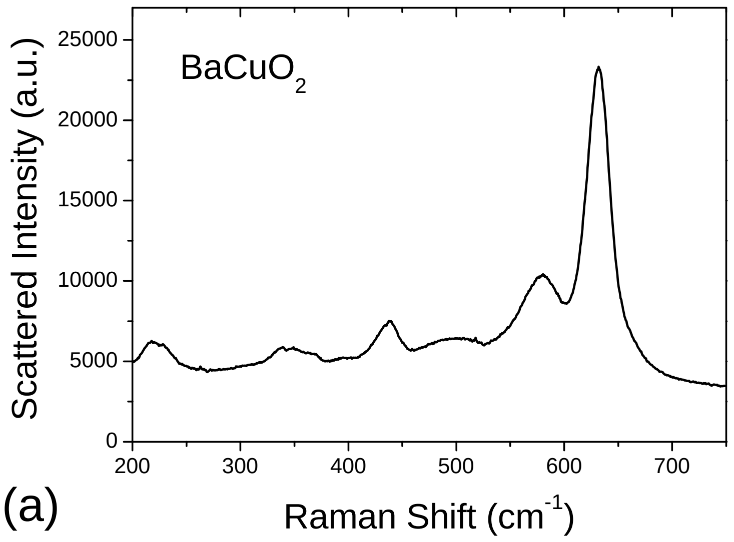

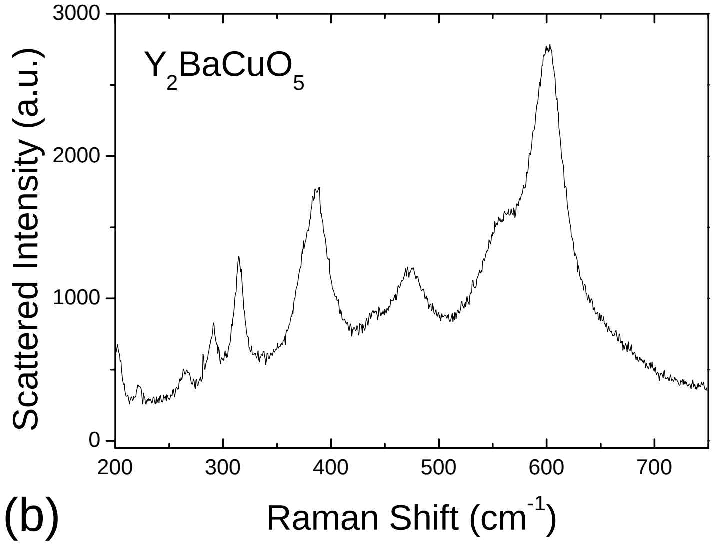

Figure 4.19. Raman spectra of impurity phases. (a) $BaCuO_2$ and (b) Y_2BaCuO_5.

Table 4.1

Phonon frequencies of secondary (precursor) phases in the range of 200 – 700 cm^{-1}

Phase	Raman Phonon Frequency (cm^{-1})
BaF_2 [4.23]	241 (vs)[‡]
Y_2O_3 [4.24,4.25]	330, 377 (vs)[‡], 433, 469 and 593
CuO[4.26,4.27]	294 (s)[‡], 342 and 625
$Y_2Cu_2O_5$[4.24,4.28]	206, 238, 261, 325, 354, 390, 514 (s)[‡], 562 and 586

Table 4.2

Phonon frequencies of impurity compounds in the range of 200 – 700 cm^{-1}

[‡] Where (vs) is *very strong* and (s) is *strong* line.

Phase	Raman Phonon Frequency (cm^{-1})
$BaCuO_2$[4.29,4.30]	217, 437, 580 and 631(vs)‡
Y_2BaCuO_5[4.31,4.32]	202, 223, 265, 291, 314, 387 (s)‡, 474, 560 and 603 (vs)‡

This study by micro-Raman spectroscopy of the secondary phases and impurities in powder form has been applied to identify the precursor phases and impurities related to the solution precursor (section 4.3.1 below) and pyrolysis process (section 4.3.2. below) as well as to determine the precursor phases involved in the YBCO growth, as we will show in chapter 5 and 6.

4.3.1. Aging Effect of the TFA-YBCO Precursor Solution

After the synthesis of the precursor solution to grow YBCO TFA-MOD films, it is necessary a right control, handling and storage of the precursor solution, in order to make uniform and reliable YBCO films with high J_c values. An aging effect of the precursor solution was observed by the appearance of a coarsening effect of precipitates of CuO and $BaCuO_2$ phases on the film, if the precursor solution is not right stored. Four YBCO samples were prepared by using the same solution in the same conditions of pyrolysis and growth parameters (790 °C). Figure 4.20 shows the sequence of SEM results for these four YBCO films grown (a) two, (b) six, (c) thirteen and (d) sixteen days after the preparation of the solution. It is important to note that the solution was keep in *eppendorf* type tube containers. The microstructure clearly indicates the increasing size of the precipitate such as CuO and $BaCuO_2$ phases. On other hand, in the case of the uniaxial texture, a not strong difference was observed between the *c*-axis grain fraction of the film grown with the two and the sixteen days after solution preparation, 90 % and 80 %, respectively.

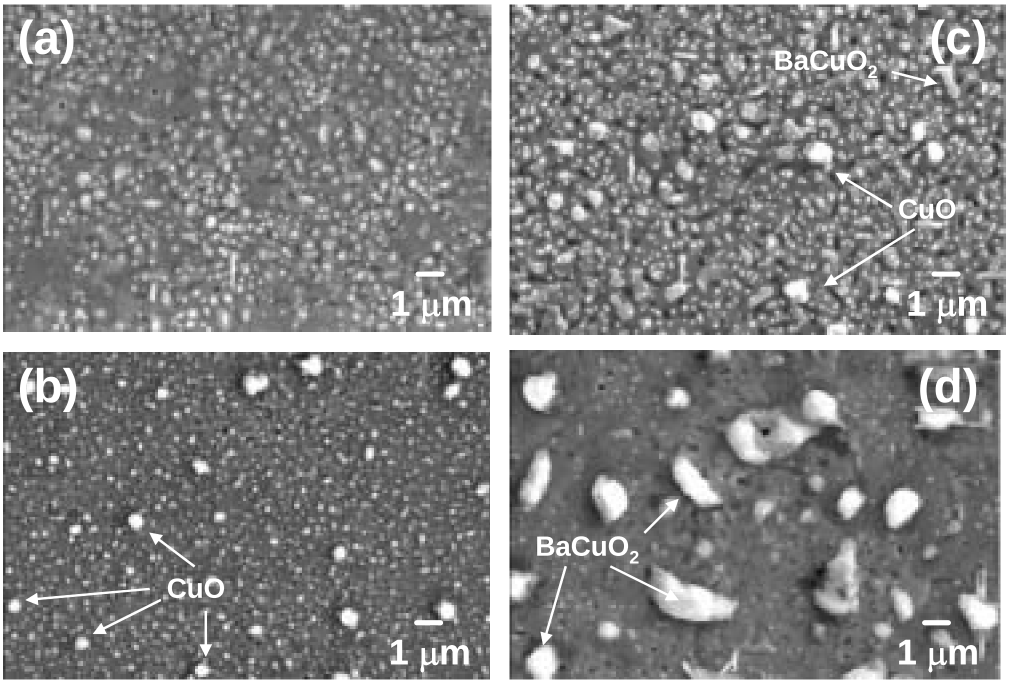

Figure 4.20. SEM images showing the aging effect of YBCO precursor solution in the final sample microstructure: (a) two, (b) six, (c) thirteen and (d) sixteen days after solution preparation. Precipitates observed are CuO and $BaCuO_2$ phases.

However, the superconducting properties such as the critical current density in the former was J_c (77K) ~ 3.2 MA/cm^2, while for the latter, J_c (77K) ~ 1.8 MA/cm^2. In addition, the coarsening of the precipitates was observed by using micro-Raman spectroscopy with a focused laser spot of size ~ 1μm over different parts of the film, detecting mainly the presence of CuO and $BaCuO_2$ phases. The measured Raman spectra of these secondary phases are shown in figure 4.21a, 4.21b and 4.21c, for two and sixteen days after preparation of the solution, respectively, while figure 4.21d shows the YBCO phonons of the YBCO matrix film. The $BaCuO_2$ precipitates have a size of the order of 1 – 5 μm, while the precipitates of CuO are smaller than 1μm. In the YBCO film with sixteen days old precursor solution, we have also observed Raman phonons corresponding to BaF_2 and Cu_2O phases in the matrix.

Therefore, the source of aging effect was the ambient atmosphere due to opening and closing of the *eppendorf* container. This fact, can thus seriously damage the precursor solution and have as a consequence the appearance of precipitates unintentionally grown, such as CuO and $BaCuO_2$ phases. Thus, it is necessary a right storage of the precursor solution in a special sealed container with porous cap (*septum*), to avoid contact of the solution with external atmosphere and then, to use a syringe to extract the required precursor solution to afterwards deposit it onto the substrate.

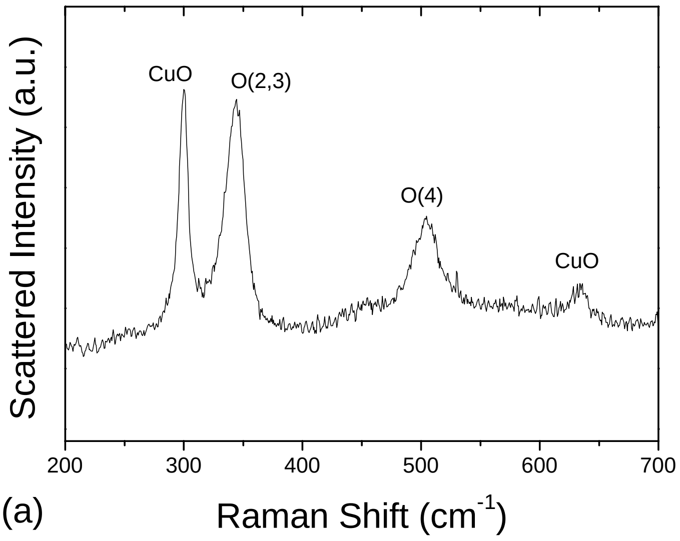

Figure 4.21. (a)

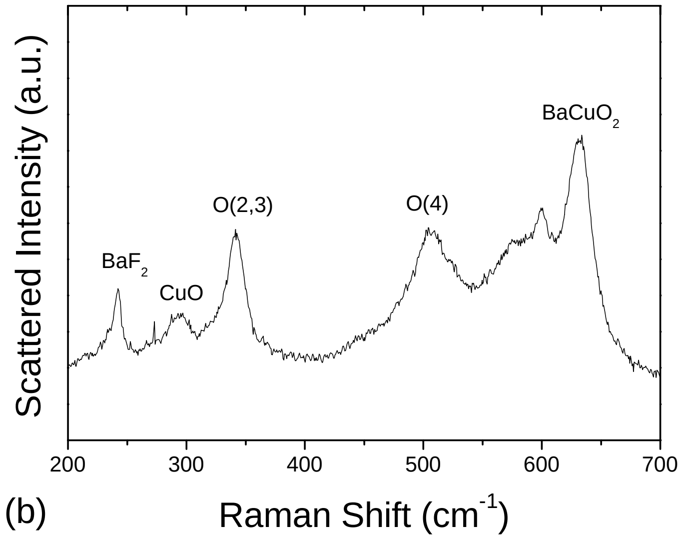

Figure 4.21. (b)

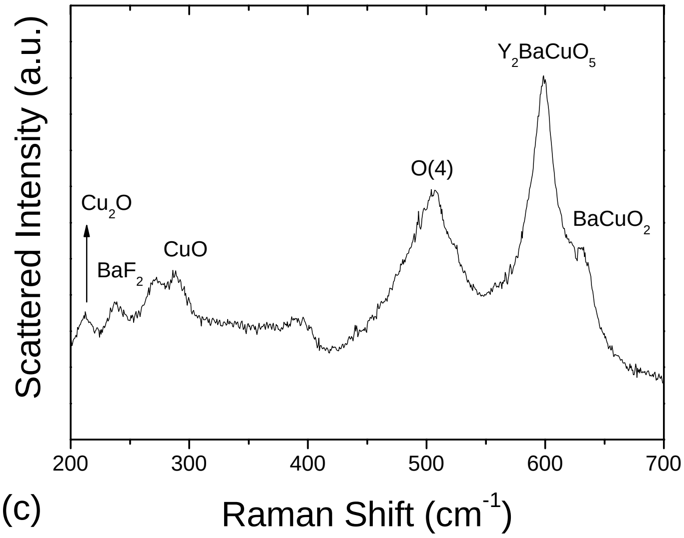

Figure 4.21. (c)

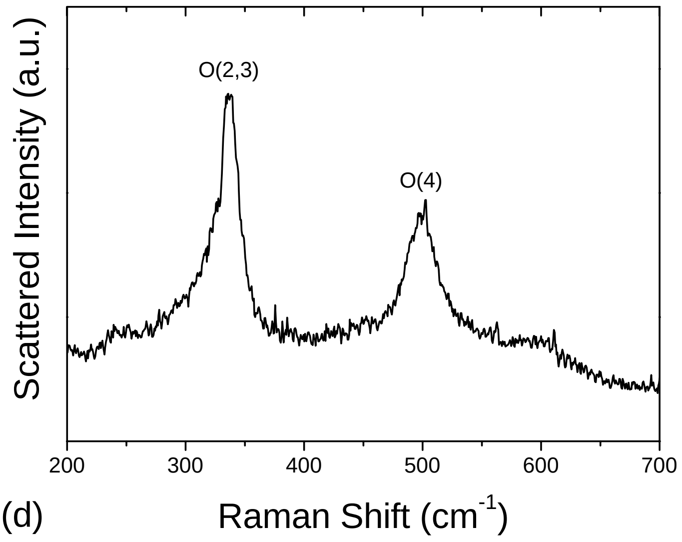

Figure 4.21. Raman spectra of precipitates in YBCO samples grown with precursor solution (a) two days old, (b),(c) sixteen days old, and (d) Raman spectrum of the matrix in the samples grown with a two days old precursor solution.

4.3.2. Control of the YBCO-TFA Pyrolysis Process

The preparation of high quality YBCO films by chemical solution process involves four steps, as we saw in section 4.1, namely solution preparation, precursor coating, pyrolysis and growth. There are multiple processing parameters which require optimization for the preparation of high quality YBCO thin films and probably not a single combination of them exists[1.26,1.28]. In the present section, we shall focus on the pyrolysis parameters control, which is a crucial step for the achievement of high-J_c superconducting films. The pyrolysis of the different metalorganic precursors occurs at rather low temperatures (300 – 400 ^{o}C) and leads to oxide and fluoride nanometric phases. The growth process of the YBCO epitaxial crystalline phase occurs in a second step after a higher thermal treatment, as we will show in chapter 5. Below we present an example where the Raman spectroscopy helped us to optimize the parameters of the pyrolysis process. The analyses of those films were complemented by SEM and optical microscopy observations.

The parameters controlling the formation of a homogeneous precursor solution deposition are mainly the viscosity, which may be controlled through the trifluoroacetate concentration in the solution, the maximum spinning velocity and acceleration rate. In addition to obtain an homogeneous pyrolyzed film one has to control the pyrolysis rate, which should be kept low enough to avoid any phase segregation and stress release in the forms of cracks, and P(O_2), temperature, P(H_2O) and gas flow rate. Optical micrographs of pyrolyzed films should appear featureless after deposition step and also after the pyrolysis. To make uniform and reliable YBCO TFA-MOD films with high-J_c values an exhaustive and systematic control of the precursor solution deposition and pyrolysis parameters is therefore necessary.

Figures 4.22 shows optical microscopy images of two samples submitted to: (a) high heating rate (60 ^{o}C/h for decomposition of organic matter) in 2 % O_2 and (b) slow heating rate (3 ^{o}C/h) in 100 % O_2. In the first image, we can easily view surface inhomogenities; these features can be associated with some kind of phase segregation during the shrinkage process of the film when the polymerized organometallic precursors decompose. We note that after a typical crystallization process the inhomogeneities observed by polarized optical microscopy (figure 4.22a) remain as a source of microstructural inhomogeneity. This is observed in SEM micrograph of the crystallized film shown in figure 4.23 which reproduces the star-like shaped microstructures observed in figure 4.22a. On the other hand, in the figure 4.22b we can observe a smooth, uniform and homogeneous surface indicating a good pyrolysis process.

After a typical sample crystallisation process, local analysis of the inhomogenities has been performed using micro-Raman spectroscopy with a focused laser spot size of 1μm to identify the crystalline phases formed in these phase-segregated features of the film. The measured Raman spectra of figure 4.22a (see figure 4.22c) shows besides the YBCO phonon modes the presence of reagents, secondary and impurity phases such as BaF_2, CuO, $BaCuO_2$ and Y_2BaCuO_5. Focusing the Raman probe over different parts within an inhomogeneous region indicated a different concentration of secondary phases thus suggesting that the inhomogenities generated during the pyrolysis involve some metal content segregation. Additionally to the formation of secondary phases, epitaxial growth of the YBCO phase is also strongly degraded in this segregated region. On the other hand, figure 4.22d shows typical Raman spectra after the crystallisation process of sample 4.22b. We can observe that there are no secondary phases or impurities on the Raman spectra.

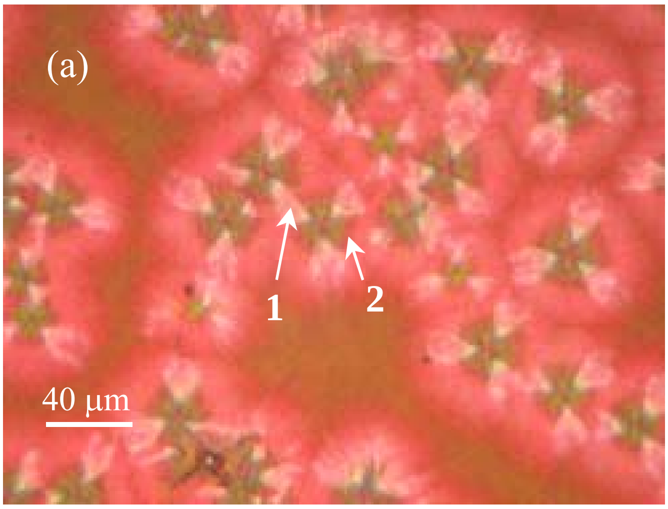

Figure 4.22. (a)

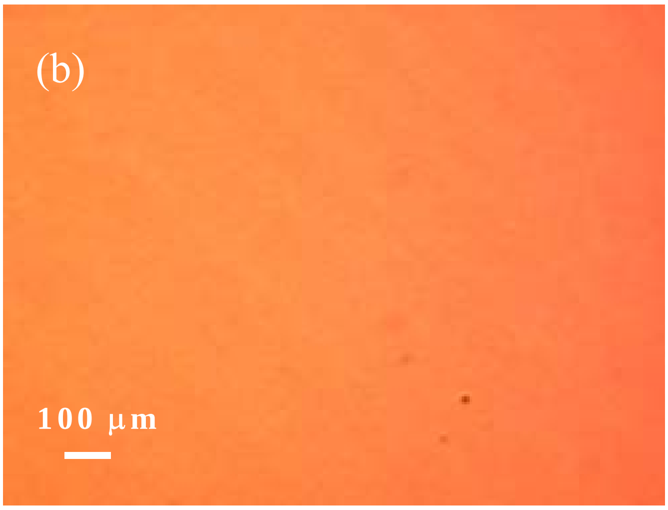

Figure 4.22. (b)

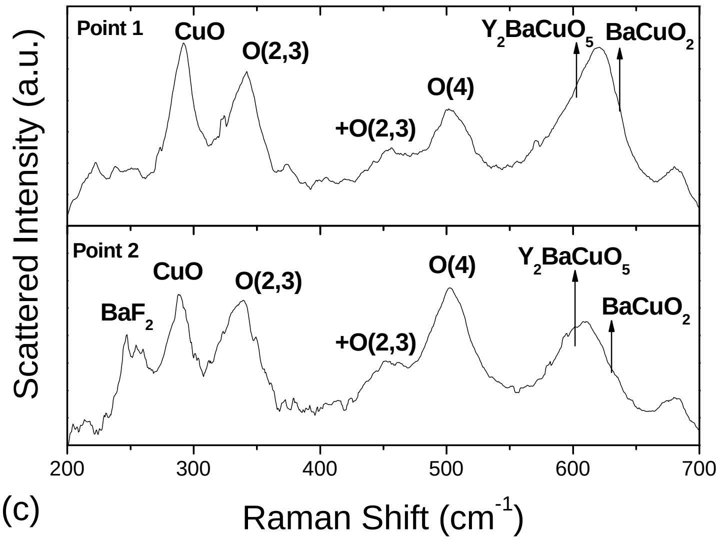

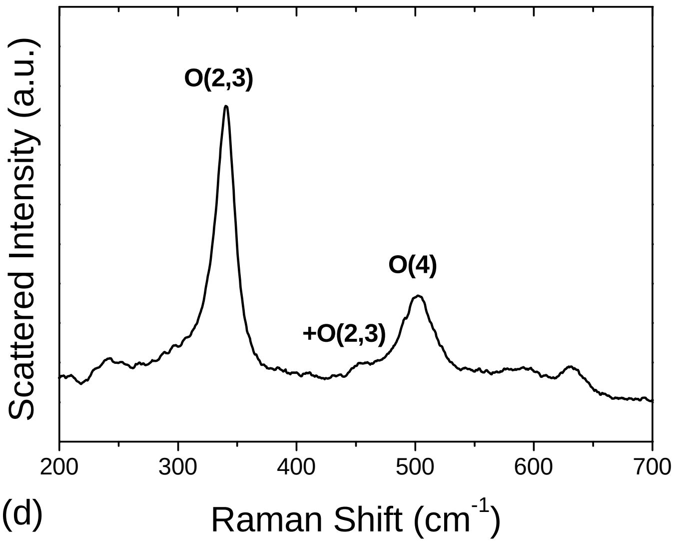

Figure 4.22. Polarized optical microscopy images of two samples with: (a) high heating rate (60 °C/h) in 0.02 mbar of O_2, P(H2O) = 24 mbar, and (b) slow heating rate (3 °C/h) in 1 mbar of O_2, P(H2O) = 7 mbar; (c) μ-Raman Scattering spectra measured at points (1) and (2) of figure (a) and (d) micro-Raman spectra of the sample shown in figure (b).

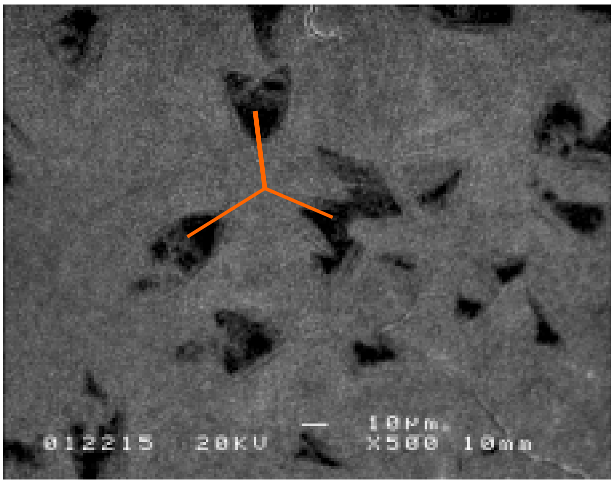

Figure 4.23. SEM micrograph of the sample 4.22a after the high temperature growth process where the same symmetrical geometry arrangements associated to inhomogeneities are observed

Therefore the presence of secondary phases produces a deterioration of the superconducting properties of the film, and the J_c value can even reduce from 3 MA/cm^2 to 2.5 KA/cm^2 at 77K for a sample like figure 4.22a. A detailed observation of the samples after the pyrolysis and growth processes with optical microscopy, SEM and μ-RS appears to be very useful because they allow us to identify local segregation processes which are difficult to detect by XRD.

Another crucial parameter of the pyrolysis process is the water pressure, because without humidified gas the pyrolysis of the gel film promotes the sublimation of the $Cu(O_2CCF_3)_2$ phase and then we obtain a film deficient in copper[4.13]. We present a particular sample pyrolyzed without wet atmosphere and then a typical crystallization process. We can observe in figure 4.24 the Raman phonons of Y_2BaCuO_5 phase and a small presence of YBCO.

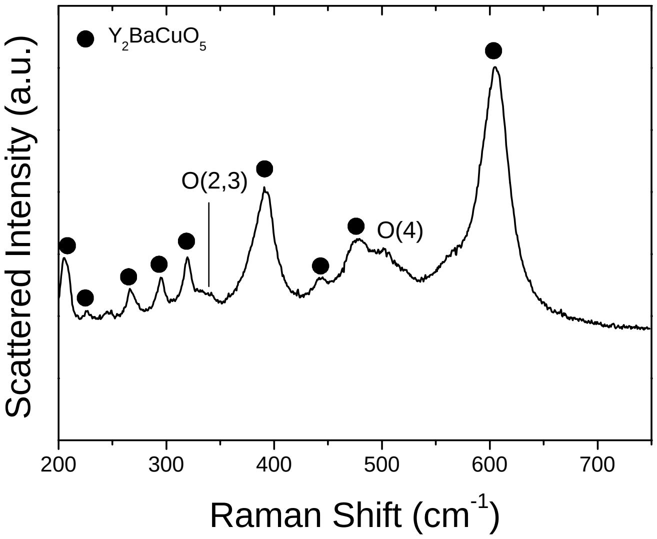

Figure 4.24. Raman spectra of sample after a typical crystallization process with pyrolysis step without wet atmosphere. Notice the strong presence of Y_2BaCuO_5 phase.

4.4. Oxygen Content and Defects

An other important feature of Raman spectra analysis is that we can also obtain information about oxygen content of the $YBa_2Cu_3O_{7-x}$ TFA-MOD films. As we saw in section 1.2.6, it is well known that the oxygen content "7-x" determines the metallicity of the YBCO (see figure 1.10). When the oxygen content diminishes its value from 7 to 6, the YBCO Raman modes are observed to undergo a blue shift (lower frequencies)[3.5]. We show in table 4.3, the Raman frequencies for YBCO orthorhombic and tetragonal phase. The most relevant variation appears for the O(4) phonon mode at 500 cm^{-1}. Consequently, this phonon mode has been chosen for the determination of the oxygen stoichiometry in our TFA films. This variation is to be linked with size variation of the unit cell when O(1) oxygen is depleted (see YBCO structure, figure 1.3). The O(1) oxygen atoms have the lowest thermal activation and are therefore depleted before the other oxygen atoms of the structure, so that the interplane Cu(2)-O(4)-Cu(1) bond is increased[§] and the corresponding frequency is decreased[4.36]. Statistical studies carried out on thin films, sintered ceramics and single crystals show that, the following empirical relationship is established[1.39]:

[§] The *c*-axis value for YBCO orthorhombic phase is ~ 11.68 Å whilst for tetragonal phase is ~ 11.84 Å

$$x = 13.58 - 0.027\omega_{O(4)} \tag{4.12}$$

Therefore, the oxygen concentration, which determines the superconducting properties of YBCO films, is in roughly linear relationship with the frequency of the mode at 500 cm^{-1}. Hence, Raman spectroscopy is a good probe to control optimal oxygenation of the films after the oxygenation process also in the YBCO TFA process (section 4.1). In particular in figure 4.25 we show the Raman spectra of two YBCO TFA-MOD samples one optimally doped ($O_{6.95}$) at 450 °C for 90 minutes and one underdoped ($O_{6.48}$) at 450 °C for 60 minutes.

Table 4.3

Raman shift frequencies of YBCO modes for the two extreme Values of the oxygen constants.

Frequency(cm^{-1})	**$YBa_2Cu_3O_7$**	**$YBa_2Cu_3O_6$**
ω_{Ba}	115	113
$\omega_{Cu(2)}$	150	140
$\omega_{O(2,3)}$	340	342
$\omega_{+O(2,3)}$	440	453
$\omega_{O(4)}$	500	466

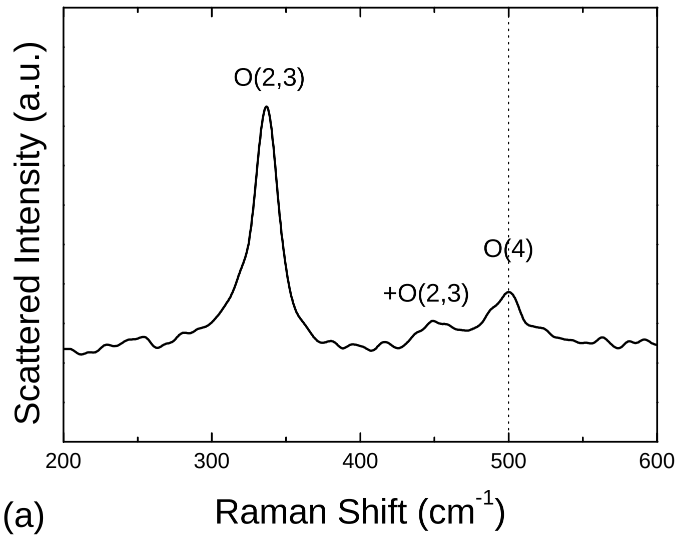

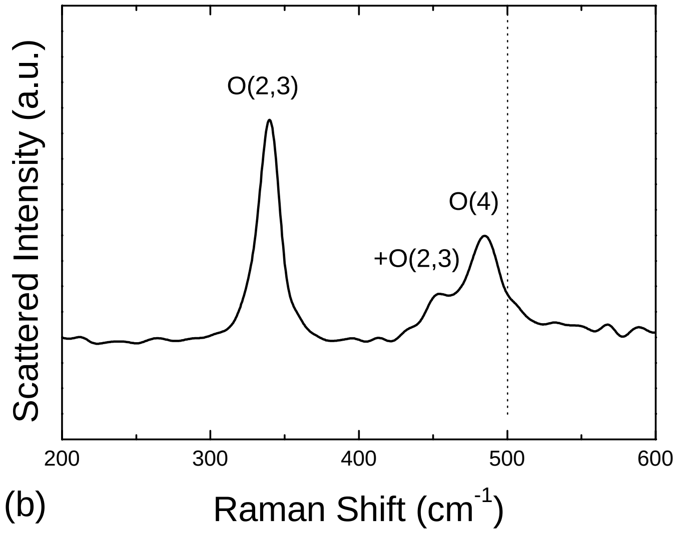

Figure 4.25. Raman spectra of YBCO TFA-MOD film (a) optimally doped $O_{6.95}$ ($\omega_{O(4)}$ = 501 cm^{-1}) and (b) underdoped $O_{6.48}$ ($\omega_{O(4)}$ = 484 cm^{-1}). The dotted line is only to indicate the 500 cm^{-1} position.

In the study, analysis and characterization of YBCO TFA-MOD films by micro-Raman spectroscopy, we observed lines due to Raman-active z-polarized A_g symmetry modes, besides these Raman–allowed bands we have also observed many additional spectral features due to local changes of the atomic environment resulting in activation of otherwise Raman-forbidden modes. These Raman-forbidden modes appearing in the Raman spectra are peaks or bands belonging to defects in the YBCO film. We have mainly observed defects related to: cation disorder and oxygen broken-chains, as shown in figure 4.26. One of the researcher in 90's performing studies on structural defects of YBCO films by micro-Raman and XRD was J. L. MacManus-Driscoll[4.37,4.38]. We name cation disorder to the replacement of barium for yttrium atom in the YBCO structure[4.39], which exhibits a broad Raman mode at 560 –580 cm^{-1}; while we name oxygen broken-chains to finite fragments of the *infinite* long Cu(1)-O(1) metallic chains, which exhibit additional Raman modes at 220 – 250 cm^{-1} [4.40] and 590 –600 cm^{-1} [4.41], for Cu(1) and O(1) atom, respectively.

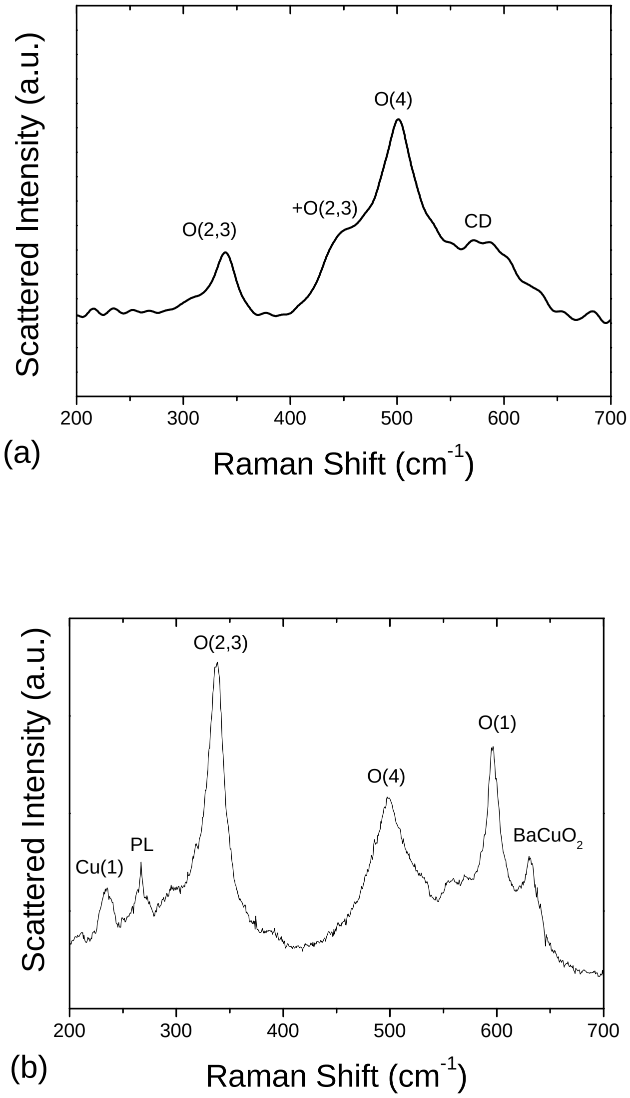

Figure 4.26. Defects in YBCO TFA films related to: (a) cation disorder (CD) at 560 – 580 cm^{-1}, and (b) oxygen broken-chains at 220 – 250 cm^{-1} (Cu(1)) and 590 –600 cm^{-1} (O(1)).

Conclusions

We have shown that the analytical capabilities of micro-Raman spectroscopy to analyse YBCO films are very broad. Raman scattering has developed into a very powerful tool in the field of high-T_c superconductivity, providing information on the fundamental physical properties of superconducting materials. At a first glance the Raman spectra may provide a lot of information and features of the TFA films such as orientation, secondary phases, impurities, oxygen content and defects. The information obtained at the molecular scale by Raman scattering can sometimes help to deduce the mechanism of activity or reactivity of some process. In this chapter we have used this technique to optimize some parameters of the YBCO TFA-MOD process. Precipitates such as CuO and $BaCuO_2$, may be avoided by right storage of precursor solution in special sealed containers which avoid the contact of the solution with the air. We have also demonstrated the assistance of micro-Raman spectroscopy complemented with SEM to characterize the pyrolysis step. We have shown that in order to achieve high quality YBCO TFA-MOD films, during the pyrolysis process the film homogeneity must be preserved and any kind of phase segregation should be avoided, otherwise the final microstructure and superconducting performances are degraded.